



University of  
Massachusetts  
Amherst

## Prediction And Manipulation Of Drop Size Distribution Of Emulsions Using Population Balance Equation Models For High-Pressure Homogenization

Item Type	Dissertation (Open Access)
Authors	Raikar, NB
DOI	<a href="https://doi.org/10.7275/1562249">10.7275/1562249</a>
Download date	2026-06-05 22:56:12
Link to Item	<a href="https://hdl.handle.net/20.500.14394/38653">https://hdl.handle.net/20.500.14394/38653</a>

**PREDICTION AND MANIPULATION OF DROP SIZE  
DISTRIBUTION OF EMULSIONS USING POPULATION  
BALANCE EQUATION MODELS FOR HIGH-PRESSURE  
HOMOGENIZATION**

A Dissertation Presented

by

NEHA B. RAIKAR

Submitted to the Graduate School of the  
University of Massachusetts Amherst in partial fulfillment  
of the requirements for the degree of

DOCTOR OF PHILOSOPHY

May 2010

Chemical Engineering

© Copyright by Neha B. Raikar 2010

All Rights Reserved

**PREDICTION AND MANIPULATION OF DROP SIZE  
DISTRIBUTION OF EMULSIONS USING POPULATION  
BALANCE EQUATION MODELS FOR HIGH-PRESSURE  
HOMOGENIZATION**

A Dissertation Presented

by

NEHA B. RAIKAR

Approved as to style and content by:

---

Michael Henson, Co-chair

---

Surita Bhatia, Co-chair

---

Michael Malone, Member

---

David Schmidt, Member

---

T.J. Mountziaris, Department Chair  
Chemical Engineering

*To my dad.*

## ACKNOWLEDGMENTS

I would like to thank my advisors Michael A. Henson, Surita Bhatia and Michael F. Malone for providing me with the opportunity to work on this project. Their valuable advice and guidance helped me throughout my work. I would also like to thank Professor David Schmidt for serving on my committee. I am grateful to Professor Julian McClements for his help and insights on the problem and also for allowing me to use equipments in his laboratory. I would also like to thank Cristhian Almedia-Rivera and Peter Bongers for their active collaboration on this project.

Family support is most important even though it is from a distance. My mom and my sister have been a tremendous help and so have been my would be in-laws. I owe a special thanks to my fiance Nilanjan who has always been by my side and motivated me throughout. I am also grateful to all my friends without whose company my stay in Amherst would not have been a pleasurable experience. Especially, Swetha, Hari, Raja, Abhisek, Gunjan and Siddhartha have always helped and supported me whenever I needed them. I would also like to thank all my group members, batchmates and other members of the chemical engineering department both past and present for their support and help in times of difficulties. I am also grateful to Neil Irving, Mike Egan and Ujwal Meda who made my internship in Liverpool a fun learning experience.

I dedicate my thesis to my dad. Although he is not with me today, I am here because of him and he will always remain my inspiration.

## **ABSTRACT**

# **PREDICTION AND MANIPULATION OF DROP SIZE DISTRIBUTION OF EMULSIONS USING POPULATION BALANCE EQUATION MODELS FOR HIGH-PRESSURE HOMOGENIZATION**

MAY 2010

NEHA B. RAIKAR

B.Chem Engg, UNIVERSITY INSTITUTE OF CHEMICAL TECHNOLOGY, MUMBAI

Ph.D., UNIVERSITY OF MASSACHUSETTS AMHERST

Directed by: Professor Michael Henson and Professor Surita Bhatia

Emulsions constitute a wide range of natural as well as processed products. Pharmaceutical applications of emulsions include oral administration, parenteral delivery, ophthalmic medicine, topical and transdermal creams, and fluorocarbon-in-water emulsions for blood oxygenation. In the foods area many of the products like mayonnaise, margarine, ice-creams are emulsions by nature and some products can also be used for delivery of active ingredients (e.g. nutraceuticals) with potential health benefits. Emulsions are also encountered at many stages of petroleum recovery, transportation, and processing. Typically, emulsions are manufactured in a two-step process. First a coarse emulsion called a premix is made which is passed through a high-pressure homogenizer. Intense energy supplied in the high pressure homogenizer causes breakage of the coarse emulsion to a fine one with a tighter distribution.

Population balance equation (PBE) models are useful for emulsions since they allow prediction of the evolution of the drop size distribution on specification of the two rate processes i.e., breakage of drops due to the flow field and coalescence of colliding drops. In our work, we developed a PBE model to describe emulsion breakage in a high pressure homogenizer. The focus of the work was breakage and conditions to keep coalescence to minimum were implemented. Two breakage rates representing two mechanisms i.e., turbulent inertial and turbulent viscous breakage were necessary for reproducing the bimodal nature of the distributions. We used mechanistic functions in the PBE model to develop a predictive model which could be extended to changes in formulation variables as well as process variables. Starting with the assumption of binary breakage, the model was refined to include multiple drop breakage. The developed model was found to be extensible to reasonable changes in oil concentration, surfactant concentration, continuous phase viscosity and constant ratio of oil to surfactant. Anomalies in pressure prediction encountered earlier were also corrected for by including some additional features like heating, maximum stable diameter, and number of daughter drops. A preliminary attempt was also made to use the developed model for designing experiments for making target emulsions with pre-specified properties.

# TABLE OF CONTENTS

	<b>Page</b>
<b>ACKNOWLEDGMENTS</b> .....	<b>v</b>
<b>ABSTRACT</b> .....	<b>vi</b>
<b>LIST OF TABLES</b> .....	<b>xi</b>
<b>LIST OF FIGURES</b> .....	<b>xii</b>
 <b>CHAPTER</b>	
<b>1. INTRODUCTION AND LITERATURE SURVEY</b> .....	<b>1</b>
1.1 Pharmaceutical and Biomedical Applications of Emulsions .....	4
1.2 Important Properties of Pharmaceutical Emulsions .....	11
1.3 Population Balance Equation Modeling of Emulsions .....	15
<b>2. INVERSE POPULATION BALANCE EQUATION MODELING:     SENSITIVITY TO MEASUREMENT ERRORS</b> .....	<b>25</b>
2.1 Population Balance Equation Model .....	26
2.2 Inverse Population Balance Equation Modeling .....	28
2.2.1 Breakage Rate Function .....	28
2.2.2 Daughter Drop Distribution Function .....	29
2.3 Simulation Results and Discussion .....	32
2.3.1 “Perfect” Data .....	33
2.3.2 Noisy data .....	34
2.3.3 Skewed Data .....	35
2.3.4 Dust Particles .....	36
2.3.5 Binned Data .....	37
2.4 Conclusions and Future Work .....	39

<b>3. EXPERIMENTAL STUDIES AND POPULATION BALANCE EQUATION MODELS FOR BREAKAGE PREDICTION OF EMULSION DROP SIZE DISTRIBUTIONS</b> .....	<b>51</b>
3.1 Experimental Methods .....	51
3.1.1 Materials .....	51
3.1.2 Emulsion Preparation .....	52
3.1.3 Emulsion Characterization .....	52
3.2 Theory .....	53
3.2.1 Computational Fluid Dynamics .....	53
3.2.2 Population Balance Equation Model .....	54
3.2.3 Parameter Estimation .....	56
3.3 Results and Discussion .....	58
3.3.1 Homogenized Drop Volume Distributions .....	58
3.3.2 Recoalescence Test .....	58
3.3.3 Computational Fluid Dynamics .....	59
3.3.4 Base Case Parameter Estimation .....	60
3.3.5 PBE Model Extensibility .....	62
3.4 Conclusion .....	66
<b>4. PREDICTION OF EMULSION DROP SIZE DISTRIBUTIONS WITH POPULATION BALANCE EQUATION MODELS OF MULTIPLE DROP BREAKAGE</b> .....	<b>80</b>
4.1 Experimental Methods .....	80
4.1.1 Materials .....	80
4.1.2 Emulsion Preparation .....	81
4.1.3 Emulsion Characterization .....	82
4.2 Theory .....	82
4.2.1 Population Balance Equation Model .....	82
4.2.2 Parameter Estimation .....	85
4.3 Results and Discussion .....	87
4.3.1 Reproducibility of Measured Drop Volume Distributions .....	87
4.3.2 Base Case Parameter Estimation .....	87
4.3.3 Model Extensibility to New Emulsification Conditions .....	89

4.4	Conclusions .....	93
<b>5.</b>	<b>PREDICTING THE EFFECT OF HOMOGENIZATION PRESSURE ON THE DROP SIZE DISTRIBUTIONS OF EMULSIONS IN A HIGH PRESSURE HOMOGENIZER .....</b>	<b>108</b>
5.1	Materials and Methods .....	108
5.1.1	Experimental Methods .....	108
5.1.2	Theory .....	109
5.2	Results and Discussion .....	116
5.2.1	Base case model .....	116
5.2.2	Heating effects .....	117
5.2.3	Interfacial tension effect .....	118
5.2.4	Critical diameter limit .....	119
5.2.5	Surfactant limit .....	120
5.2.6	Effect of number of daughter drops .....	120
5.2.7	Overall trends in the objective function .....	121
5.2.8	Design .....	121
5.3	Conclusion .....	123
<b>6.</b>	<b>CONCLUSIONS AND FUTURE WORK .....</b>	<b>137</b>
6.1	Summary .....	137
6.2	Future Work .....	138
 <b>APPENDICES</b>		
<b>A.</b>	<b>DERIVATION OF THE TURBULENT VISCOUS BREAKAGE RATE FUNCTION .....</b>	<b>140</b>
<b>B.</b>	<b>MAXIMUM STABLE DROP SIZES .....</b>	<b>142</b>
<b>C.</b>	<b>DERIVATION OF THE NO APPLIED PRESSURE BREAKAGE RATE FUNCTION .....</b>	<b>144</b>
<b>BIBLIOGRAPHY .....</b>		<b>146</b>

## LIST OF TABLES

<b>Table</b>	<b>Page</b>
3.1 Base case emulsion formulation and homogenization values . . . . .	67
3.2 Range of emulsion formulations and homogenization pressures studied . . . . .	67
4.1 Base case emulsion formulation and homogenization values . . . . .	95
4.2 Variable oil concentrations . . . . .	95
4.3 Variable surfactant concentrations . . . . .	95
4.4 Concentrations used to maintain constant oil to surfactant ratio . . . . .	96
5.1 Oil and surfactant concentrations . . . . .	125
5.2 Objective function values for 5 wt% oil and 1 wt% surfactant . . . . .	125
5.3 Design options . . . . .	125
5.4 Design strategy with experimental and model results . . . . .	126

## LIST OF FIGURES

Figure	Page
1.1 Biodistribution as function of emulsion drop size [75, redrawn from Chpt 5]. . . . .	3
2.1 Inverse population balance modeling results for perfect drop volume distribution data. (a) Transient number drop distributions. (b) Predicted and actual drop breakage rate and daughter drop distribution functions. (c) Predicted and actual transient cumulative drop distributions. (d) Predicted and actual transient number drop distributions. . . . .	40
2.2 Effect of the drop breakage and daughter drop distribution functions on the predicted cumulative distribution ( $t = 5$ min). (a) Estimated breakage function and actual distribution function. (b) Actual breakage function and estimated distribution function. (c) Estimated breakage and distribution functions. . . . .	41
2.3 Inverse population balance modeling results with six noisy drop volume distributions. (a) Noisy and actual transient number drop distributions. (b) Predicted and actual drop breakage rate and daughter drop distribution functions. (c) Predicted and actual transient cumulative drop distributions. (d) Predicted and actual transient number drop distributions. . . . .	42
2.4 Inverse population balance modeling results with twelve noisy drop volume distributions. (a) Noisy and actual transient cumulative drop distributions. (b) Predicted and actual drop breakage rate and daughter drop distribution functions. (c) Predicted and actual transient cumulative drop distributions. (d) Predicted and actual transient number drop distributions. . . . .	43
2.5 Inverse population balance modeling results with transient drop volume distributions skewed towards larger drops. (a) Skewed and actual transient number drop distributions. (b) Predicted and actual drop breakage rate and daughter drop distribution functions. (c) Predicted and actual transient cumulative drop distributions. (d) Predicted and actual transient number drop distributions. . . . .	44

2.6	Inverse population balance modeling results with transient drop volume distributions skewed towards smaller drops. (a) Skewed and actual transient number drop distributions. (b) Predicted and actual drop breakage rate and daughter drop distribution functions. (c) Predicted and actual transient cumulative drop distributions. (d) Predicted and actual transient number drop distributions. . . . .	45
2.7	Inverse population balance modeling results with transient drop volume distributions skewed by dust peak. (a) Skewed transient number drop distributions. (b) Predicted and actual drop breakage rate and daughter drop distribution functions. (c) Predicted and actual transient cumulative drop distributions. (d) Predicted and actual transient number drop distributions. . . . .	46
2.8	Drop size distribution measurements obtained with dynamic light scattering for a mineral oil in water emulsion with Pluronic F-68 as the surfactant. (a) Results for a coarse emulsion obtained with a stator-rotor device. (b) Results for a processed emulsion obtained with a single pass of a high-pressure homogenizer. . . . .	47
2.9	Inverse population balance modeling results with transient drop volume distributions represented by 10 bins. (a) The binned transient number drop distribution at $t = 5$ min. (b) Predicted and actual drop breakage rate and daughter drop distribution functions. (c) Predicted and actual transient cumulative drop distributions. (d) Predicted and actual transient number drop distributions. . . . .	48
2.10	Inverse population balance modeling results with transient drop volume distributions represented by 50 bins. (a) The binned transient number drop distribution at $t = 5$ min. (b) Predicted and actual drop breakage rate and daughter drop distribution functions. (c) Predicted and actual transient cumulative drop distributions. (d) Predicted and actual transient number drop distributions. . . . .	49
2.11	Inverse population balance modeling results with transient drop volume distributions represented by 200 bins. (a) The binned transient number drop distribution at $t = 5$ min. (b) Predicted and actual drop breakage rate and daughter drop distribution functions. (c) Predicted and actual transient cumulative drop distributions. (d) Predicted and actual transient number drop distributions. . . . .	50
3.1	(a) Measured drop volume distributions for the base case conditions. Optical microscopy image at 20x magnification of (b) the pre-emulsion, (c) the homogenized sample after the first pass, and (d) the homogenized sample after the fifth pass. . . . .	68

3.2	Recoalescence test where the base case formulation was homogenized for six passes at 10000 psig (labeled H10K-1 through H10K-6) and then homogenized for five passes at 5000 psig (labeled as H5K-1 through H5K-5). (a) Sauter mean diameters $d_{32}$ . (b) Drop volume distributions. ....	69
3.3	Computational fluid dynamics simulation of the homogenizing valve gap showing contours of turbulence intensity (%) near the valve. The section of the homogenizing valve is shown at the extreme left. The portion of the valve gap used for CFD calculation is shown in the center. Enlarged sections of the gap inlet, the middle part of the gap, and the gap outlet are shown on the right.....	70
3.4	Base case parameter estimation results with the drop-eddy collision breakage function $g_1(v)$ . (a) Breakage rate. (b) Predicted and experimental drop volume distributions for the pre-emulsion (P), the first pass (1), the third pass (3), and the fifth pass (5). $\Psi$ is the objective function value. ....	71
3.5	Base case parameter estimation results with the shear breakage function $g_2(v)$ . (a) Breakage rate. (b) Predicted and experimental drop volume distributions. Base case parameter estimation results with the combined breakage function $g(v) = g_1(v) + g_2(v)$ . (c) Breakage rate. (d) Predicted and experimental drop volume distributions. ....	72
3.6	Effect of dispersed phase volume fraction and interfacial tension on the experimental and predicted mean diameters. a) Experimental mean diameters $d_{43}$ for changes in dispersed phase volume fraction. b) Predicted mean diameters $d_{43}$ using base case values for changes in dispersed phase volume fraction. c) Experimental mean diameters $d_{43}$ for changes in interfacial tension. d) Predicted mean diameters $d_{43}$ using base case values for changes in interfacial tension. ....	73
3.7	Effect of continuous phase viscosity and pressure on the experimental and predicted mean diameters. a) Experimental mean diameters $d_{43}$ for changes in continuous phase viscosity. b) Predicted mean diameters $d_{43}$ using base case values for changes in continuous phase viscosity. c) Experimental mean diameters $d_{43}$ for changes in pressure. d) Predicted mean diameters $d_{43}$ using base case values for changes in pressure. ....	74

3.8	Effect of the dispersed phase volume fraction on predicted drop volume distributions with the combined breakage function $g(v)$ for the pre-emulsion (P), the first pass (1), the third pass (3), and the fifth pass (5). $\Psi$ is the objective function value. The base case values were used for the adjustable breakage parameters $K_1-K_4$ . (a) $\phi = 2.78 \times 10^{-3}$ . (c) $\phi = 0.0112$ . The parameters $K_1-K_4$ were re-estimated using a combined data set containing the dispersed phase volume fraction variations. (b) $\phi = 2.78 \times 10^{-3}$ . (d) $\phi = 0.0112$ . . . . .	75
3.9	Effect of the interfacial tension on predicted drop volume distributions with the combined breakage function $g(v)$ . The base case values were used for the adjustable breakage parameters $K_1-K_4$ . (a) $\sigma = 14.318$ mN/m. (c) $\sigma = 13.056$ mN/m. The parameters $K_1-K_4$ were re-estimated using a combined data set containing the interfacial tension variations. (b) $\sigma = 14.318$ mN/m. (d) $\sigma = 13.056$ . . . . .	76
3.10	Effect of the continuous phase viscosity on predicted drop volume distributions with the combined breakage function $g(v)$ . The base case values were used for the adjustable breakage parameters $K_1-K_4$ . (a) $\eta_c = 1.09$ cP. (c) $\eta_c = 1.195$ cP. The parameters $K_1-K_4$ were re-estimated using a combined data set containing the continuous phase viscosity variations. (b) $\eta_c = 1.09$ cP. (d) $\eta_c = 1.195$ cP. . . . .	77
3.11	Effect of simultaneous changes in the dispersed phase volume fraction, interfacial tension, and continuous phase viscosity with the combined breakage function $g(v)$ . (a) The base case values were used for the adjustable breakage parameters $K_1-K_4$ . (b) The parameters $K_1-K_4$ were re-estimated using a combined data set containing variations in the three formulation variables. . . . .	78
3.12	Effect of the homogenization pressure on predicted drop volume distributions with the combined breakage function $g(v)$ . The base case values were used for the adjustable breakage parameters $K_1-K_4$ . (a) $P = 5000$ psig (34.47 MPa). (c) $P = 15000$ psig (103.42 MPa). The parameters $K_1-K_4$ were re-estimated using a combined data set containing the pressure variations. (b) $P = 5000$ psig (34.47 MPa). (d) $P = 15000$ psig (103.42 MPa). . . . .	79
4.1	Experimental variability calculated from 5 repeats of the base case emulsification procedure. (a) Average drop size distributions and standard deviations for the first three homogenization passes. (b) Average Sauter mean diameters $d_{32}$ and standard deviations for the premix and the first three homogenization passes. . . . .	97

4.2	Drop size distribution predictions assuming binary breakage (equation (4.7)). (a) Predicted first pass drop size distribution. (b) Predicted third pass drop size distributions (c) Prediction drop size distributions for all 3 passes. (d) Experimental and predicted Sauter mean diameters $d_{32}$ for all three passes. ....	98
4.3	Drop size distribution predictions assuming multiple breakage (equation (4.9)) with $q=1$ and $p=20$ . (a) Predicted first pass drop size distribution. (b) Predicted third pass drop size distributions (c) Prediction drop size distributions for all 3 passes. (d) Experimental and predicted Sauter mean diameters $d_{32}$ for all three passes. ....	99
4.4	Effect of the multiple drop breakage parameters $p$ and $q$ on objective function values. (a)Effect of $p$ . (b) Effect of $q$ .....	100
4.5	Effect of variable oil concentrations. (a) Experimental drop size distributions for the third pass. (b) Predicted drop size distributions for the third pass. (c) Experimental and predicted Sauter mean diameter $d_{32}$ for all three passes. (d) Predicted drop size distributions for the third pass assuming binary drop breakage. ....	101
4.6	Effect of variable surfactant concentrations. (a) Experimental drop size distributions for the third pass. (b) Predicted drop size distributions for the third pass. (c) Experimental and predicted Sauter mean diameter $d_{32}$ for all three passes. ....	102
4.7	Effect of constant oil to surfactant ratio. (a) Experimental drop size distributions for the third pass. (b) Predicted drop size distributions for the third pass. (c) Experimental and predicted Sauter mean diameter $d_{32}$ for all three passes. ....	103
4.8	Re-estimation of the breakage rate parameters from a data set containing variable oil to surfactant ratios. Experimental and predicted drop size distributions for: a) 0.5wt% oil and 0.1wt% surfactant; b) 1.0wt% oil and 0.1wt% surfactant; c) 5.0wt% oil and 0.2wt% surfactant; and d) 5.0wt% oil and 0.3wt% surfactant. ....	104
4.9	Ratio of adsorption to collision timescales. (a) Effect of oil concentration. (b) Effect of surfactant concentration. (c) Constant oil to surfactant ratio. (d) Effect of oil to surfactant ratio. ....	105

4.10	Effect of premix preparation. (a) Drop size distributions for the premixes. (b) Experimental drop size distributions for the third pass. (c) Predicted drop size distributions for the third pass. (d) Experimental Sauter mean diameters for the premixes and the third pass and predicted Sauter mean diameters for first pass. ....	106
4.11	Effect of homogenization at no applied pressure. (a) Experimental and predicted first pass drop size distributions. (b) Experimental and predicted third pass drop size distributions, (c) Experimental and predicted drop size distributions for all three passes. (d) Breakage rate function $g_3(v)$ estimated for all three passes. ....	107
5.1	Base case parameter estimation for different pressures with experimental and predicted drop volume distributions for the (P) premix, (1) the first pass, (3) the third pass, and (5) the fifth pass. $\Psi$ is the objective function value for a particular pressure set. (a) 250 bar pressure set. (b) 750 bar pressure set. (c) 1250 bar pressure set. (d) Pass by pass objective function as a function of the number of passes for the different pressures. ....	127
5.2	Effect of the inclusion of heating effects on parameter estimation for different pressures with experimental and predicted drop volume distributions. (a) Average temperature difference and the effective pressure as a function of the applied pressure with error bar representing the standard deviation. (b) 250 bar pressure set. (c) 750 bar pressure set. (d) 1250 bar pressure set. ....	128
5.3	Experimental data and model fits for interfacial tension. (a) Interfacial tension as a function of surfactant concentration with a fit to quadratic equation. (b) $\Gamma/\Gamma_\infty$ as a function of concentration. ....	129
5.4	Effect of the inclusion of change in interfacial tension with passes on parameter estimation for different pressures with experimental and predicted drop volume distributions. (a) Interfacial tension as a function of the number of passes for different pressures. (b) 250 bar pressure set. (c) 750 bar pressure set. (d) 1250 bar pressure set. ....	130
5.5	Critical diameter fits to experimental 5 <sup>th</sup> pass $d_{32}$ . (a) Mean diameter $d_{32}$ with $d_{ti}$ for 5wt% oil and 1wt% surfactant. (b) Mean diameter $d_{32}$ with pressure for 5wt% oil and 1wt% surfactant. (c) Mean diameter $d_{32}$ with $d_{ti}$ for 10wt% oil and 2wt% surfactant. (b) Mean diameter $d_{32}$ with pressure for 10wt% oil and 2wt% surfactant ....	131

5.6	Effect of critical diameter limit on parameter estimation for different pressures with experimental and predicted drop volume distributions. (a) 250 bar pressure set. (b) 750 bar pressure set. (c) 1250 bar pressure set. (d) Diameter ratio versus number of passes for different pressures before and after inclusion of the critical diameter limit. ....	132
5.7	Effect of inclusion of the surfactant depletion limit. (a) 5 wt % oil and 1 wt % surfactant at 250 bar case with experimental data and model predictions. (b) Surfactant ratio and diameter ratio versus number of passes before and after inclusion of the surfactant limit. ....	133
5.8	Effect of the number of daughter drops on parameter estimation for different pressures with experimental and predicted drop volume distributions. (a) Objective function value for different number of daughter drops. (b) 250 bar pressure set for $p = 150$ and all the previously mentioned effects. (c) 750 bar pressure set for $p = 150$ and all the previously mentioned effects. (d) 1250 bar pressure set for $p = 150$ and all the previously mentioned effects. ....	134
5.9	Trends in Objective function for different formulations and the effect of different cases discussed. 3 different formulations as listed in table 5.1 were simulated using constants optimized for 5 wt% oil and 1 wt% surfactant. ....	135
5.10	Design of target emulsions. (a) Energy dissipation rate as a function of pressure. (b) Attainable region of drops sizes at 250 bar pressure. (c) Attainable region of drops sizes for all pressures with lines of constant polydispersity and constant $d_{32}$ as guides. ....	136

# **CHAPTER 1**

## **INTRODUCTION AND LITERATURE SURVEY**

An emulsion is a dispersion of an immiscible or partly miscible liquid (dispersed phase) into another (continuous phase). The stability against drop coalescence is provided by adding small amounts of a surface-active agent i.e., a surfactant which adsorbs at the drop interface. The surfactant has two main roles to play: it lowers the surface tension, thereby facilitating drop breakup; and it minimizes re-coalescence. Common examples of emulsions are mayonnaise, margarine, and shampoos. Depending on the nature of the dispersed and the continuous phase, different types of emulsions can be distinguished such as oil-in-water (o/w), water-in-oil (w/o) emulsions and different types of multiple emulsions [67].

Emulsions can be used for a wide variety of applications like foods, petroleum recovery, cosmetics, polishes, road surfacing and agricultural sprays. In the foods industry, emulsions constitute numerous natural as well as processed products such as milk, butter, margarine, sauces and desserts. Commonly used food emulsion ingredients include an edible oil, water, a surfactant, vitamins, minerals and flavors [68]. Emulsions are also encountered in the petroleum industry with applications at many stages of petroleum recovery, transportation, and processing [12, 98]. In petroleum recovery applications, emulsion formation at the well-head is undesirable while emulsions are critical for enhanced oil recovery as drilling muds and fluids. Heavy crude oils typically have viscosities in the range of a few hundred to several thousand centipoise, and therefore they cannot be transported economically in conventional pipelines without reducing their viscosity [73]. Emulsifying heavy oils with an aqueous solution significantly reduces the viscosity, allowing for lower pumping power

requirements and more economical transportation [90,94,123].

Our focus is on emulsions used for pharmaceutical applications. These emulsions can be intended for oral administration, parenteral (intravenous or intramuscular) delivery, ophthalmic medicine, and topical and transdermal creams [67] discussed in detail in the following section. An important criteria for formulation of parenteral emulsions is that they should not be recognized as foreign by the body. Thus a good drug carrier should be biocompatible, biodegradable, often of fine and uniform particle size, be suitable for targeting and be pharmaceutically acceptable. Also selective drug targeting is essential for improved drug effectiveness, reduction in adverse reactions and for applying highly potent drugs. The choice of particular emulsion system is therefore dependent on the route of administration, the drug characteristics and the effect required.

The biodistribution of colloidal systems can be related to various physiological processes as a function of the particle size. For instance particles with mean diameter less than 7  $\mu\text{m}$  become entrapped in the capillary network of the lungs. The smaller particles tend to accumulate in the bone marrow. Particles below 100 nm are capable of escaping the vascular system as the cut-off diameter is believed to be 100 nm for the largest pores. Thus by properly selecting particle size and its distribution the behavior of a drug in the body can be partly controlled. Alteration of tissue distribution can also be made by modifying the surface structure of the emulsifier shell of the oil-droplet. The particle surface charge too has marked effects on the clearance and deposition of colloids [65,75]. As we have seen that the drop size is the key parameter for selective targeting, it becomes necessary to develop techniques for its manipulation and control.

Population Balance Equation Modeling seems to be an effective tool in such a study for tailoring optimum emulsions. Our research goal was to be able to predict important

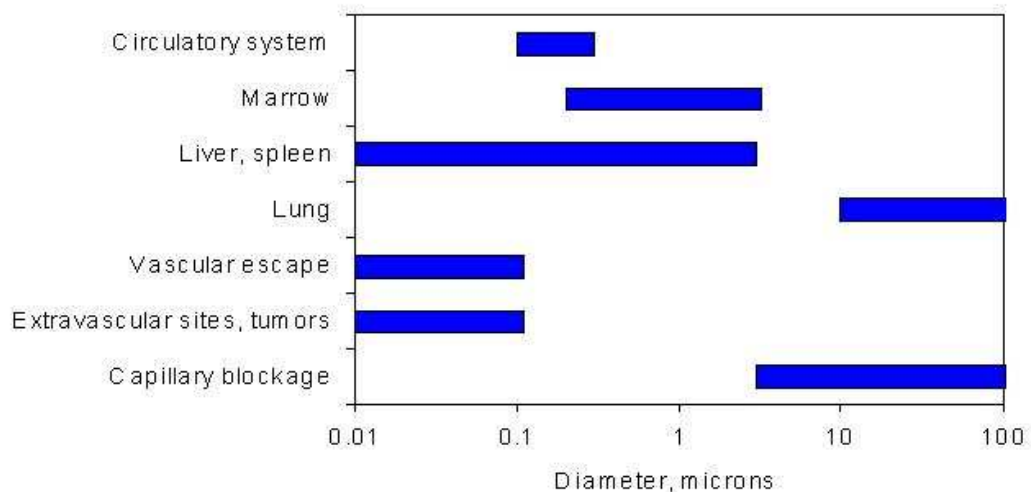


**Figure 1.1.** Biodistribution as function of emulsion drop size [75, redrawn from Chpt 5].

emulsion characteristics in high pressure homogenizers, especially drop size distribution. Emulsions are typically formulated using a high pressure homogenizers. It is necessary to understand the homogenizer mechanics and the phenomena responsible for drop disruption to be able to characterize the emulsions. The research objective was to identify appropriate functions based on theory as well as mechanics of the process rather than using some empirical relations. It was also important that the model developed be extensible to various systems and hence, should also consider system properties. Overall, we wanted the prediction to be robust enough to deal with any model system and therefore although our focus was on pharmaceutical emulsion, the model we developed was general and could be used for any emulsion application.

To put our work in the perspective of the wider state of the art research, first the relevant literature in pharmaceutical and biomedical applications of emulsions is presented. Also, what properties of emulsions are important and how they are affected is reviewed in Section 1.2

## 1.1 Pharmaceutical and Biomedical Applications of Emulsions

### Different Emulsified Systems

There are different types of emulsions in addition to the normally encountered micron scale emulsions which are used in pharmaceutical and biomedical applications. The common ones are described below

- **Submicron Emulsions (SME) or Nanoemulsions** - Submicron emulsions or nanoemulsions are emulsions with average drop-size less than a micron. They are usually of the oil - in - water type with sizes about 20-300 nm. These emulsions offer greater bioavailability than the coarse micron sized emulsions because of their higher surface area to volume ratio. These emulsions are either transparent or translucent because of their size and also possess stability against sedimentation and creaming [13, 67, 74, 100].
- **Multiple Emulsions** - Multiple Emulsions are complex systems wherein droplets of the dispersed phase contain additional but smaller droplets. These droplets can be different or identical to the continuous phase. For example, water-in-oil-in-water emulsions (w/o/w) are three phase emulsion systems in which the oil droplets dispersed in the external aqueous phase contain additional internal aqueous phase [14, 67, 75, 107].
- **Microemulsions (ME)** - Microemulsions are dispersions of immiscible liquids with a combination of several components, namely, surfactant and co-surfactant. They are thermodynamically stable, form spontaneously and are isotropically clear. Microemulsions are percolated or bicontinuous structures with no internal or external phase and no possibility of dilution [51, 67, 75, 107].
- **Self Emulsifying Drug Delivery Systems (SEDDS)** - Self Emulsifying Drug Delivery Systems (SEDDS) are stable homogeneous mixtures of oils, surfactants or alternatively, one or more hydrophilic solvents and co-solvents. They have the ability to form emulsions (SEDDS) or microemulsions (Self Microemulsifying Drug Delivery

Systems SMEDDS) upon dilution by the aqueous media, such as Gastrointestinal (GI) fluids. The digestive mobility of the stomach and the intestine provide agitation necessary for emulsification [6, 33, 36, 67, 107, 120].

### **Pharmaceutical and Biomedical applications**

Important and widely used pharmaceutical and biomedical applications are now discussed

- **Oral Administration of Drugs**

Oral administration of drugs is the oldest known route for drug delivery. Emulsions have been used for oral formulations by incorporation of the drug in the internal phase. Emulsions are also known to increase the bioavailability of poor soluble drugs and to extend their pharmacological effects by protecting from degradation by the gastric medium. For example, cefpodoxime proxetil is a lipophilic drug used to treat a variety of bacterial infections, including those of the ear, nose, throat, skin and soft tissues, genitourinary tract, respiratory tract, and other organs. It is an orally absorbed, broad spectrum, third generation cephalosporin ester. It is hydrolyzed by a cholinesterase prior to intestinal absorption resulting in incomplete absorption. Oil-in-water submicron emulsions were found to be effective in protecting the drug from enzymatic attack [74]. In this case the drug, cefpodoxime proxetil is first dissolved in a co-solvent followed by dissolution of the mixture in a medium chain triglyceride. Lecithin is used to emulsify the oil and the aqueous phase [74].

- **Parenteral Nutrition or Therapeutic Feeding**

Special oil-in-water emulsions are used to feed patients suffering from malnutrition and/or whose medical condition makes oral nutrition infeasible. In such cases the emulsion primarily comprises of a nourishing lipid (about 20%) to overcome the fatty acid deficiency. It can be used alone or with admixtures of other essential compounds (glucose, amino acids, vitamins, trace elements etc.) to constitute “Total Parenteral

Nutrition Admixtures” (TPN). The parenteral emulsion must be bacteriologically pure, and physiological compatible. They should be primarily nutritious and should have drop sizes less than 5  $\mu\text{m}$  to avoid the risk of pulmonary embolism [12, 22, 67]. Intralipid<sup>®</sup> is an example of commercially available lipid emulsion with soyabean oil (10 or 20%) as the oily phase emulsified by egg lecithin (1.2%). Glycerol (2.5%), a water-miscible solvent is added to improve stability and reduce the drop size to less than 5  $\mu\text{m}$  [12, 67].

- Parenteral Emulsions for Drug Delivery

Many drugs have insufficient aqueous solubility and/or problem of water hydrolysis. If such drugs have sufficient lipid solubility they can be incorporated into the interior oil phase of fat emulsions. The drug incorporation can either be extemporaneous, addition of the drug in preformed fat emulsion or by a *de novo* process, drug incorporated into the oil during the manufacturing process. Such parenteral formulations avoid use of conventional co-solvents and therefore problems of drug precipitation at the site [67, 107]. For example, Paclitaxel is a drug with significant anti-tumor activity against various tumors such as breast cancer, advanced ovarian carcinoma, lung cancer, head and neck carcinoma and acute leukemia. A microemulsion formulation has been proposed with Cremaphor EL<sup>®</sup> as solubilizer. This formulation to be administered intravenously was found to exhibit reduced hypersensitivity reactions as against the current clinical paclitaxel injection Taxol<sup>®</sup> (solution of paclitaxel in 50% Cremaphor EL<sup>®</sup>) [39, 44].

- Red Cell Substitutes or Oxygen Therapeutics

Blood loss is a common occurrence during surgery, and often blood must be rapidly replaced. This is done either using the patient’s own blood (autologous) or a donor’s blood (allogenic). Blood substitutes i.e., artificial oxygen carriers, are desired as alternatives to allogenic blood transfusion. Such substances can also be required to

improve tissue oxygenation or as adjuncts to balloon angioplasty and cancer therapy. They are more appropriately called “red cell substitutes” or “oxygen therapeutics” as these fluids on injection into the blood make significant contribution to the systemic oxygen transport and flow characteristics. Increasing public negative perceptions about blood safety coupled with the potential risk of transmitting diseases such as hepatitis, and HIV. has necessitated development of these blood substitutes. Two kinds of solutions are available in this area: 1) fluids based on natural respiratory pigment, haemoglobin (Hb) and 2) use of synthetic, inert, fluorinated compounds called perfluorochemicals (PFCs). Since the PFC-emulsion based blood substitutes are almost exclusively synthetic, concerns about the source and purity of the components is eliminated. PFCs have the highest gas dissolving capacity of any liquids ( $\approx$  40-50 vol % for oxygen). Oxygent<sup>®</sup> is a third generation improved PFC based injectable emulsion. It contains perflubron (58 w/v %) and perfluorodecyl bromide C<sub>10</sub>F<sub>21</sub>Br (2 w/v %) stabilized by egg yolk phospholipids (3.6 w/v %). Perflubron is highly lipophilic because of its terminal bromine and is therefore excreted quickly by the body. The Oxygent<sup>®</sup> emulsion is sterile, non-pyrogenic and stable. Oxygent<sup>®</sup> was found to be effective during its evaluation in advanced clinical trials as oxygenation fluid for patients with high blood loss [51, 60–62, 88, 104].

- Pulmonary Delivery

Emulsions have also been used for delivering drugs into the lungs i.e. pulmonary administration. Inhalation of drugs, proteins, peptides etc. shows promise because it allows their rapid deposit in the target organs. This causes lesser side effects than administration by other routes and allows deposit of the larger concentrations at the sites of disease. A reverse water-in-Fluorocarbon emulsion in a pressurized metereddose has been used for *in vivo* delivery of caffeine in a homogeneous and reproducible way [15]. A hydrofluoroalkane (Solkane<sup>®</sup> 227) was used as the propellant as it showed no sealing or leakage problems. Such Fluorocarbon emulsions are a promis-

ing delivery systems for drugs like enzymes, proteins, peptides (insulin ,  $\alpha$ -interferon, calcitonin, immunoglobulin, antibiotics) etc. to the lungs [15,20].

- **Ophthalmic Medicine**

A number of lipophilic and poorly water soluble drugs are used for treatment of different extra and intra-ocular etiological conditions such as glaucoma, keratitis, dry eye syndrome etc. Oil in water lipid emulsions have been investigated as a vehicle to improve the ocular bioavailability of such drugs [54–56, 79, 106, 107, 124]. Natural biodegradability, nanometer size range, sterilizability and substantial drug solubilization at the dispersed oil phase or o/w interface coupled with improved bioavailability has made lipid emulsions promising ocular delivery vehicle. Cyclosporin A (CsA) is an immunosuppressive drug and is used for prevention of corneal graft rejection and dry eye syndrome. CsA possesses lipophilic properties preventing aqueous formulations and hence oil-in-water emulsions and microemulsions have been used for its ophthalmic delivery. Restasis<sup>®</sup> is a Food and Drug Administration (FDA) approved Cyclosporin A emulsion formulation (0.05 %) for treatment of patients with keratoconjunctivitis sicca whose lack of tear production is presumed to be due to ocular inflammation [54]. Since epithelial corneal cells exhibit negative charges on their surface, it is hypothesized that a positively charged emulsion would interact with corneal cells and prolong residence time on the surface of the cornea. Cationic emulsions containing CsA when administered to rabbits produced higher drug levels at the ocular surface (cornea and conjunctiva) [79, 106]. A new approach employing water soluble prodrug of Cyclosporin A has been proposed for ocular delivery [54–56].

- **Topical and Transdermal Delivery**

The skin is the most accessible and largest organ of the body that receives about one third of the blood supply. Topical and transdermal delivery is a non invasive way of administering active drugs. When using topical routes, selection of an appropri-

ate vehicle is important in order to increase the flux of the given drug. As topical vehicles emulsions are gaining attention because of their characteristics, namely, enhanced drug solubility, good kinetic stability, reduced side effects, prolonged pharmacological effects and ease of manufacture [26, 67]. Nano/Submicron emulsions have been investigated for the topical delivery of Flurbiprofen, a chiral non steroidal anti-inflammatory drug used to treat gout, osteoarthritis, rheumatoid arthritis, sunburn etc [26]. Lipid emulsions composed of isopropyl myristate, soyabean oil or coconut oil with egg lecithin as the emulsifier containing Flurbiprofen in the oil phase were formulated and successfully tested in vitro as well as in vivo. Submicron emulsion vehicles have also been investigated for the delivery of non-steroidal anti-inflammatory agents (diclofenac, indomethacin, naproxen, piroxicam) and steroidal anti-inflammatory agents (betamethasone esters) [30]. A transdermal therapeutic delivery system for aceclofenac using microemulsion was also formulated with the goal of maximizing flux through skin in the systemic circulation [59]. The microemulsion system was composed of 1.5% aceclofenac in oil (Labrafil<sup>®</sup> M 1944 CS), surfactant (Cremophor<sup>®</sup> EL), co-surfactant (ethanol) and water.

- Gene/ DNA Carriers

Gene transfection implies delivery to and subsequent expression of the functional genetic material in special cells to manipulate their intrinsic genetic profiles. The genetic materials can be carried either by viral vectors (retrovirus, adenovirus, herpes-simplex virus) or non-viral vectors (liposomes, emulsions, nanoparticles etc.). The nonviral vectors are preferred since they are easy to handle and have better safety profiles. Because lipids are main components of cell membrane, nonviral vectors are generally lipid based so that the vectors can be effectively incorporated in the cell membrane and facilitate delivery of genetic material into specific cells [2, 13, 76, 100]. DNA being negatively charged, cationic emulsions show promise as nonviral carriers because of the tendency to form stable complexes via electrostatic interaction.

A cationic emulsion loaded with VIJns plasmid encoding Antigen 85 of *Mycobacterium tuberculosis* was investigated for pulmonary immunization against the inhaled pathogens [13]. A number of researchers have successfully demonstrated the use of cationic lipid emulsions for delivery of plasmid DNA (pDNA) [8, 42, 47]. The success of such systems for gene transfection is however hampered by the associated cellular toxicity of cationic lipids. An artificial lipoprotein delivery system consisting of nanoemulsion cores made of natural lipids and surface lipidized polyLlysine has been developed. This artificial lipoprotein delivery system efficiently carried plasmid DNA containing - galactosidase gene and successfully transfected human SF-767 glioma tumor cells [76]. The same system was used to carry the gene encoding rabies virus glycoprotein and thus used as rabies DNA vaccine. It demonstrated highly effective transfection capability of rabies DNA vaccine in cell culture [2].

- Molecular Imaging and Therapy

Emulsions mainly perfluorocarbon based have been used for the purpose of molecular imaging i.e. detection of molecular markers like proteins and other cell surface receptors. These emulsions also have potential for targeted drug delivery permitting verification and quantification of treatment i.e. rational targeted therapy. Important target pathologies include inflammation, atherosclerosis, tumor related angiogenesis and thrombi. The agent used is a ligand targeted, lipid encapsulated, non gaseous fluorocarbon emulsion which is stable to handling pressure, atmospheric exposure, heat and shear. An enhanced acoustic reflectivity of the emulsion is derived from its collective deposition along various tissue planes creating a layering effect. The emulsion cores exhibit low velocity and high density when compared with water and surrounding tissues. The acoustic enhancement can be effectively measured by an acoustic transmission line model. Incorporation of a paramagnetic material, for example, a gadolinium complex into the lipid layer of the emulsions provides contrast agents for both ultrasound and magnetic resonance imaging modalities [51, 58, 87, 89].

Having reviewed the relevant literature, we now take a close look at the important properties of pharmaceutical emulsion.

## 1.2 Important Properties of Pharmaceutical Emulsions

Some of the important properties of pharmaceutical emulsions are discussed [9–12, 17, 26, 67, 70, 75, 78, 93, 100, 107]. These are the properties that characterize the emulsion and few of them can be determined experimentally.

- Conductivity and Type

Emulsion type is the most important property. Emulsions can be of o/w or w/o type or even multiple emulsions. Our model experimental system is an oil-in-water type emulsion. The type of emulsion could be characterized by electrolytic conductivity. For such a measurement the electrolyte is incorporated in the aqueous phase and the electrolytic conductivity  $\kappa_{em}$  can be approximated to be proportional to the conductivity of the external phase  $\kappa_{ext}$  and its volumetric proportion  $\phi_{ext}$ .

$$\kappa_{em} = \kappa_{ext} \times \phi_{ext}$$

- Drop Size and Distribution

Emulsification is a random process with breakage and coalescence steps being in equilibrium. The resulting emulsion is a polydispersed system consisting of a range of drop sizes. Factors like lower surface tension or an increase in stirring energy and duration increases breakage, while a higher fluid viscosity decrease it. On the other hand increase in temperature would increase the coalescence rate. The drop size distribution also determines the stability and viscosity of the system. The drop size distribution is commonly measured using various light scattering techniques.

- Emulsion Viscosity

Emulsions generally show non-Newtonian behavior. For rheology only stable (non-settling) emulsions subjected to mechanical stress are considered. A plot of emulsion

viscosity versus dispersed phase fraction should be plotted for particular application and emulsifying device. However, it is generally observed that at low dispersed phase fractions ( $\phi_{int}$ ), the relative viscosity ( $\eta_r$ ) is  $\eta_r = 1 + 2.5\phi_{int}$  [75]. An increase in dispersed phase fractions increases number of drops and therefore drop-drop interactions. The resulting frictional effects cause a viscosity increase. Beyond 60-65% dispersed phase pseudoplastic behavior is seen with power law dependence of viscosity on the applied shear rate and above 85-90% dispersed phase fraction a viscoelastic behavior is seen. As mentioned earlier the drop size and distribution affects emulsion viscosity. The interdrop friction is related to surface area. Thus with higher surface area i.e. smaller drops there is an increase in viscosity generally by the following relation [75].

$$\log \frac{\eta}{\eta_0} = -B \log \frac{d}{d_0}$$

Bimodal emulsions show a significant viscosity reduction compared to the base emulsions if the mode of separation is large enough [75]. This can be employed in practice to reduce the viscosity by mixing a coarse emulsion with a fine one. The effect is more pronounced when a narrowly dispersed coarse emulsion is mixed with a poly-dispersed fine emulsion.

- Biodistribution

Emulsion systems are used as carriers of poorly soluble or lipophilic drugs primarily due to their ability to solubilize such drugs. A good drug carrier should be biocompatible, stable, biodegradable, of fine and uniform size in addition to being pharmaceutically acceptable. By controlling the physicochemical properties of the carrier such particle size, dosage, charges etc. the biodistribution can be tuned. This is a passive control. In active control involves modifying the surface by incorporating a ligand for specific targeting.

- Surface Characteristics

Since colloidal particles are opsonized (i.e. susceptible to the action of phagocytes) in the bloodstream, modifying the structure of the emulsifier shell by changing the composition can alter the tissue distribution. It is commonly observed that hydrophobic particles are taken up by macrophages without opsonization. The droplet surface can therefore be coated with hydrophilic polymers to reduce macrophage uptake. This is due to combination of steric stabilization alongwith reduction in the uptake of opsonising blood components at droplet surface. Carriers with hydrophilic surface (e.g. PEG coated) are ignored by phagocytotic cells. Using nonionic coemulsifier like poloxamine reduces uptake by liver and spleen. Presence of methyl groups on the outer surface reduces adhesion of the droplet on the macrophage. For this reason, the emulsions using Pluronics are not engulfed by macrophages. The surface characteristics are thus determined by the constituents of the formulation.

- Surface Charge

The surface charge is an important property of emulsion carrier systems and can be measured by Zeta Potential measurements. Emulsions in general can be classified as anionic or cationic. Several common emulsions are anionic. Cationic emulsions can be formulated by using cationic lipids like stearylamine or polysaccharides. In the bloodstream neutral emulsions are taken up slowly as compared to charged ones. Anionic emulsions have higher liver and spleen uptake, wheres cationic emulsions show initial accumulation in the lungs and are then relocated to the liver and spleen. For topical applications like ocular or transdermal delivery, cationic emulsion show better uptake. This is assumed to be due to the negative charge on the surface (cornea and skin respectively). However the toxicity of cationic emulsions is a major concern.

- Stability Concerns

Emulsion breaking or instability can be stimulated by temperature changes, gravity,

and Brownian motion. The breaking process comprises of a) long-distance approach between drop and flat interface, b) interdrop film drainage and c) coalescence. Settling is a separation process driven by the density difference of the dispersed phase and continuous phase. The drop size also affects settling rate which is higher for bigger drops (macroemulsion range 1-100  $\mu\text{m}$ ) than smaller (miniemulsion range 100-500  $\text{\AA}$ ). The approach of drops close to each other is followed by the drainage process and is the second step of emulsion decay. There are several different mechanisms that drive the drainage process like Van der Waals attractive force, viscosity or interfacial phenomena. If the emulsions are small i.e. in the nanometer range, Ostwald ripening or molecular diffusion, arising from emulsion polydispersity is the primarily mechanism for emulsion destabilization. This is because, the Brownian motion or diffusion rate is higher than gravity induced sedimentation rate. The Lifshitz-Slezov and Wagner theory (LSW) predicts a linear relation between the cube of the radius and time. Experimentally, the stability can be analyzed by visual observation and measurement of drop size distribution versus time [100]. Incorporation of a drug normally decreases the stability of emulsions. To stabilize the emulsion, the strength of the interfacial film should be increase either by steric or electrostatic stabilization. Use of charged surfactants or mixed emulsifying agents is found to improve stability.

- Structure of emulsion carriers

The excipients used in manufacturing emulsion carriers are also important. Primary concern is solubility of the drug in the carrier followed by bioacceptance. Lecithins, phospholipids are used as emulsifiers. Certain L-isomeric phospholipids produce neurotoxic side effects if their gel transition temperature is close to body temperature. Cationic emulsions have cationic lipids which can be toxic.

In the following section, the population balance equation model with its applications and associated functions is discussed.

### 1.3 Population Balance Equation Modeling of Emulsions

The drop-size distribution produced is the one of the most essential property for characterizing an emulsion. Other emulsion properties like viscosity are also dependant on the drop-size-distribution. Population Balance Models are used to simulate the process of generation of emulsions or dispersions. The extensive use of the population balance model is because they allow a detailed description of the two rate processes that occur in the system: drop breakage due to flow conditions and drop coalescence due to collisions between drops. The population balance equation gives the evolution of the drop size distribution with time. The population balance concept requires that for any volume element  $dv$ , the number of particles moving in and out of that range and those accumulating within it are balanced. If  $n(v, t)dv$  represent the number of droplets per unit volume of the dispersion at time  $t$  with size between volumes  $v$  and  $v + dv$ , the population balance equation takes the following form [18]:

$$\frac{\partial n(v, t)}{\partial t} + \frac{\partial}{\partial v}[\dot{v}n(v, t)] + \frac{1}{\tau}[n(v, t) - n_F(v, t)] = E(v, t) - D(v, t) \quad (1.1)$$

where,

$v$	volume of the particle
$\dot{v} = dv/dt$	particle growth rate
$\partial[\dot{v}n(v, t)]/\partial v$	convective flux along the size axis
$\tau$	residence time
$n_F(v, t)$	feed size distribution
$E(v, t), D(v, t)$	Birth rate and Death rate functions respectively

Since there is no growth rate as drops do not grow by itself,  $\dot{v} = 0$ , the equation for the batch case can be written as [92]:

$$\frac{dn(v, t)}{dt} = -g(v)n(v, t) - n(v, t) \int_0^\infty \eta(v, v')n(v', t)dv' + \int_v^\infty \beta(v, v')\nu(v')g(v')n(v', t)dv' + \frac{1}{2} \int_0^\infty \eta(v - v', v')n(v', t)dv' \quad (1.2)$$

Here,

$g(v)$  breakage frequency (fraction of drops of size  $v$  breaking per unit time)

$\nu(v')$  number of daughter drops formed by breakage of drop of size  $v'$

$\beta(v, v')$  probability density function (probability of forming drops of size  $v$  from breakage of drops of size  $v'$ )

$\eta(v, v')$  coalescence frequency between drops of size  $v$  and drops of size  $v'$

The first two terms on the right hand side of equation 1.2 represent the rate of disappearance of drops of size  $v$  by breakage and coalescence, respectively. The third and the fourth terms represent the rate of appearance of drops of size  $v$  by breakage and coalescence. The model requires specification of appropriate functions that describe breakage and coalescence processes. If the volume fraction of the dispersed phase is sufficiently small and surfactant concentration is high enough, coalescence can be neglected [109, 113, 114]. The balance equation then reduces to:

$$\frac{dn(v, t)}{dt} = -g(v)n(v, t) + \int_v^\infty \beta(v, v')\nu(v')g(v')n(v', t)dv' \quad (1.3)$$

Coulaloglou and Tavlarides [19] used the drop population balance model (eqn 1.2) to describe the interaction processes in continuously agitated liquid-liquid dispersions. They proposed phenomenological models for breakage and coalescence for turbulently agitated dispersions. The breakage model was based on drop deformation and breakup under local pressure fluctuations and time required for a critically deformed drop to break in a locally isotropic field. The coalescence model proposed assumed the coalescence rate to be proportional to collision rate times coalescence frequency of deformable drops in the kinetic regime of locally isotropic turbulent fields. Ramkrishna *et al.* [52, 53, 64, 71, 72, 83, 84,

86, 95, 96] have used the population balance model framework to a number of particulate systems like lean liquid-liquid dispersions, microbial populations etc. They have modeled pure breaking, pure aggregating and also combination of both breaking and aggregating systems. They have also accomplished analysis on dispersed systems by a cumulative volume (or mass) distribution rather than the number density function. This evolution equation in terms of the cumulative distribution for pure breakage processes is as follows.

$$\frac{\partial F(v, t)}{\partial t} = \int_0^\infty g(v') G(v, v') \partial_v F(v', t) \quad (1.4)$$

where  $F(v, t)$  is the cumulative volume fraction of drops of size less than or equal to  $v$  at time  $t$  and  $G(v, v')$  is the cumulative volume fraction of drops of size less than or equal to  $v$  formed by breakage of drops of size  $v'$ . The primary advantages of using the cumulative distribution are: 1) Many chemical process systems are more influenced by the amount of the dispersed phase and not the number of particles, 2) The integrodifferential equations satisfied by the cumulative volume fraction form are simpler and involve lesser number of functions and 3) It become easy to characterize the distributions as “self-similar” as seen by the invariance of the cumulative fraction along curves on which the similarity variable remains fixed [84]. However the decision of the form of population balance equation used is dictated by the particulate process being investigated and so both the forms are being used as per the need. Majority of the work in this thesis uses the number distribution form because of the high sensitivity of the inverse method to errors in measurements.

Chen *et al.* [18] used the steady state version of the population balance model for prediction of drop distribution in a continuous flow screw-loop reactor. A simplified form of the model was used neglecting coalescence. The breakage rate was derived from turbulence theory considering the effect of both viscosity and interfacial tension. A functional expression was proposed for the daughter distribution function and the model parameters were evaluated by fitting the experimental data. Alopaeus *et al.* [3–5] have used a multiblock

mixed tank model along with the population balance equation for simulating drop populations in mixed tanks. Since the local turbulence and flow values of the mixed tank were used in their model, it was possible to have a closer look at the breakage and coalescence phenomena. They proposed that the flow model can be obtained from measurement or from Computational Fluid Dynamic (CFD) simulations. It has been argued that this method is advantageous over a vessel-averaged population balance approach since it is capable of predicting inhomogeneities occurring in a mixed tank.

Ruiz and Padilla [91, 92] have applied the population balance model to simulate the drop size distribution for liquid-liquid extraction. In their work, only breakage event was considered and coalescence was eliminated by using very low dispersed phase volume fractions. They critically analyzed various breakage functions along with different distribution functions. Some of these functions were used with the population balance model to predict theoretical transient and steady state drop distributions. They compared the results with experimentally obtained distributions to find functions that provided the best fit. They observed that the breakage frequency function,  $g(v)$ , has a little influence on the evolution of the drop size distribution whereas,  $\beta(v, v')$  influenced the shape of the distribution. The equilibrium distribution was found to depend on the maximum stable drop size and daughter distribution function while being independent of the functional form of the breakage frequency function. It was also observed that coalescence even at low dispersed phase volume fractions, becomes significant under equilibrium conditions and cannot be ignored.

Soon *et al.* [101] used an ultra-high velocity jet homogenizer for emulsification of a coarse suspension. The theory of turbulent breakage of drops by eddy velocities developed by Kolmogorov was stated to propose the dependence of drop breakage on local fluid energy dissipation rate. They used computational fluid dynamics (CFD) to map velocity profile of the jet and the associated local energy dissipation rate. Simulations carried out for evo-

lution of drop distribution were based on the population balance equation proposed by Coualoglou and Tavlarides [19] which is similar to one represented by equation 1.2. Turbulent flow in the jet was assumed to be homogeneous and isotropic and breakage was considered to occur due to local turbulent energy dissipation in the high-energy region of the orifice. Drop coalescence was considered to be negligible and justified by presence of adequate amounts of surfactant. Crude dispersions were subjected to disruption in the homogenizer under different conditions like varying pressure and number of drops and drop size measurements were obtained. The CFD predicted energy dissipation rate at the orifice was used in the population balance model to obtain theoretical drop size distributions. The values of unknown parameters were obtained by comparing with experimental data and were found to be independent of the operating conditions. Integration of the CFD simulations of the energy dissipation rates with the population balance model was found to be successful in predicting drop size distributions that compared well with experimental data for their case of non-coalescing oil-in-water emulsions.

Vankova *et al.* have applied a steady state version of the population balance equation model to a custom built homogenizer. They have investigated the capability of the said homogenizer for making food emulsions and explored various dispersed phase and surfactants [109, 113, 114]. They have also a CFD study of the homogenization zone and have identified appropriate breakage and distribution functions for the same. Hakansson *et al.* have simulated the effect of pressure for milk-homogenizers using a full version of the PBE model and added surfactant adsorption effects as well [37, 38]. Although binary breakage is commonly assumed, several researchers have also considered multiple drop breakage with the PBE modeling framework, including the development of alternative daughter drop distribution functions [7, 24, 40, 49, 109, 115, 125]

Ramkrishna *et.al* [52, 53, 64, 71, 72, 83, 84, 86, 95, 96] have used the concept of similar-

ity in population balances. The similarity property was used to characterize and also to identify key model parameters associated with system behavior. The property of similarity manifests in the form described as self-similar which involves invariant domains in space of the independent variable along which the solution remains the same or contains a part that is the same. Ramkrishna *et al.* extended the concept self-similar distribution to develop a mathematical and computational procedure which can extract quantitative information from transient drop size distributions. This technique works with the transient population balance model in terms of the cumulative distribution. For instance when applied to pure breakage process, the breakage frequency and the cumulative daughter drop distribution can be extracted using experimental data. The main advantage of this model is that it is not committed to any specific form of the model function. The argument is that when an available model form is inappropriate, parameter-fitting procedures will lead to compromise choices of the parameters resulting in inadequate particle models. It was noticed that when self-similarity is observed, solution of the inverse problem provides a satisfactory estimate of the breakage function. An evidence of self-similarity was also shown to exist in drop breakage under a wide variety of experimental conditions.

### **Associated Functions**

Simulation of the population balance model requires specification of appropriate models for breakage and coalescence. A lot of work is being done on the effect of physical properties or geometrical and operating conditions on the average drop size and drop size distribution so obtained. However, only a limited number of studies focus on developing breakage and coalescence models. For the process of emulsification many times it is reasonable to assume that coalescence is absent which can be justified by using low dispersed phase volume fractions and adequate amounts of the surfactant. This reduces the model problem to a pure breakage one thereby simplifying it. However coalescence becomes

crucial under certain conditions like high oil concentration and surfactant deficiencies and needs to be considered.

A number of mechanisms for drop breakage have been proposed, the prominent ones being drop elongation in shear flow field (Taylor [108]), turbulent pressure fluctuations (Hinze [41]), relative velocity fluctuations (Narsimhan *et al.* [72]), and drop-eddy collision (Coulaloglou and Tavlarides [19]). Cavitation and impact are also equally likely but turbulence is considered to be the dominant mechanism. A number of breakage functions have been used of which a few are listed below

- A linear dependence is shown by sub-Kolmogorov drops [21]  $g(v) \approx kv$ .
- The power law was proposed by Valentas *et al.* [110–112] and is of the form  $g(v) = kv^n$ . The linear and the power law functions do not provide any insight into the possible breakage mechanism. Also it is specific to one system and is not robust to be extensible to a different process or formulation.
- Coulaloglou and Tavlarides [19] derived an equation based on hydrodynamics of the dispersion. They assumed that breakup of a drop is the result of a collision with a turbulent eddy. If the energy imparted to the drop by the eddy is greater than the drop surface energy, it deforms and breaks. The function so developed has the form given below.

$$g(v) = k_1 v^{-2/9} \epsilon^{1/3} \exp \left[ -\frac{k_2 \sigma (1 + \phi)^2}{\rho_d v^{5/9} \epsilon^{2/3}} \right] \quad (1.5)$$

- Chen *et al.* [18] proposed a mechanistic model for the breakage of drops incorporating both interfacial tension and viscosity.

$$g(v) = k_1 \exp \left[ -\frac{k_2 \sigma (1 + \phi)^2}{\rho_d v^{5/9} \epsilon^{2/3}} - \frac{k_3 \eta_d (1 + \phi)}{\rho_d v^{4/9} \epsilon^{1/3}} \right] \quad (1.6)$$

These equations involve system properties like dispersed phase volume fraction ( $\phi$ ), interfacial tension ( $\sigma$ ), dispersed phase density and viscosity ( $\rho_d, \eta_d$ ), energy dissipation rate ( $\epsilon$ ) and proportionality constants ( $k's$ ).

It is also important to consider the number of drops formed on breakage and their distribution. Some drops break in a large number of small drops called thorough breakage (Narsimhan *et al.* [72]). Under erosive breakage conditions a number of small drops are stripped out of a large one. Binary breakup is also possible and most of the modeling works generally view breakage as a series of binary breakage events. Multiple drop breakage has also been used by some authors [24, 40, 49, 109]. Starting initially with binary breakage, we have later used a power law product form of the generalized Hill-Ng distributions [24, 40, 125]. Some of the commonly used daughter distribution functions are listed below.

- Uniform Distribution

$$\beta(v, v') = \frac{1}{v'} \quad (1.7)$$

- Truncated normal density function with maximum probability of equal size drops.

$$\beta(v, v') = \frac{2.4}{v'} \exp \left[ -4.5 \frac{(2v - v')^2}{(v')^2} \right] \quad (1.8)$$

- Beta distribution

$$\beta(v, v') = 30 \left( \frac{v}{v'} \right)^2 \left( 1 - \frac{v}{v'} \right)^2 \quad \text{such that, } \int_0^1 \beta(v, v') d \left( \frac{v}{v'} \right) = 1 \quad (1.9)$$

- U-shaped distribution with zero probability of two equal size drops

$$\beta(v, v') = \left( \frac{1}{\frac{v}{v'} + b} + \frac{1}{1 - \frac{v}{v'} + b} + \frac{2(g-1)}{b+0.5} \right) \frac{I}{v'}$$

$$I = \frac{0.5}{\ln(1+b) - \ln(b) + \frac{g-1}{b+0.5}} \quad g = \frac{0.5a}{2b(1+b)(1-a)} \quad (1.10)$$

- Power-law product- This is the only daughter drop distribution function for multiple drop breakage that we have considered

$$\beta(v, v') = \frac{p}{\mathbf{B}(q, r)} \left( \frac{v}{v'} \right)^{q-1} \left( 1 - \frac{v}{v'} \right)^{r-1}, \quad r = q(p-1) \quad (1.11)$$

Even though coalescence has been neglected for most of the cases, it would be worthwhile to look at the coalescence functions used. According to Coualaloglou and Tavlarides [19], the coalescence frequency of drops of size  $v$  and  $v'$  is given by the product of the drop collision frequency ( $h(v, v')$ ) and the coalescence efficiency ( $\lambda(v, v')$ ) as follows

$$F(v, v') = h(v, v')\lambda(v, v')n(v)n(v') \quad (1.12)$$

- Collision Frequency - The commonly used collision frequency is based on the assumption that drops in turbulent flow behave like gas molecules.

$$h(v, v') = k_1 \frac{\epsilon^{1/3}}{1 + \phi} (v^{2/3} + v'^{2/3})(v^{2/9} + v'^{2/9})^{1/2} \quad (1.13)$$

- Coalescence Efficiency - According to Coualaloglou and Tavlarides coalescence occurs when the contact time is greater than time required for coalescence i.e. the time required for the liquid film between two drops to drain out.

$$\lambda(v, v') = \exp \left[ -k_2 \frac{C\mu_c \rho_c \epsilon}{\sigma^2} \left( \frac{v^{1/3} v'^{1/3}}{v^{1/3} + v'^{1/3}} \right)^4 \right] \quad (1.14)$$

Sovova [102, 103] suggested that above relation favors coalescence of smaller drops and proposed a function based on energy of drop collision. Here the exponential term represents the ratio of interfacial energy over the energy of collision. Many other coalescence functions have been proposed most of which are modifications of the one by Coualaloglou and Tavalariades [19].

$$\lambda(v, v') = \exp \left[ -k_2 \frac{\sigma(v^{2/3} + v'^{2/3})}{\rho_d N^2 D_i^{4/3} (v^{11/3} + v'^{11/3})} \right] \quad (1.15)$$

### **Organization of the thesis**

So far we have reviewed the relevant literature related to PBE modeling, the remainder of the thesis includes my contribution towards using population balance equation model for predicting emulsion drop size distribution. In chapter 2, I have used the inverse method based on concept of self-similarity to extract functions for breakage rate and distribution functions. We examined the sensitivity of the method for errors in input data which was generated from simulation. The method was found to be highly sensitive even to small errors in input and also required re-estimation of the functions for different experiments. Hence, for all future studies we used the direct version of the PBE model as given in equation 1.2 and tried to include mechanistic functions for breakage and coalescence. In chapter 3, we develop such a PBE model considering turbulence and binary breakage of drops and also tested extensibility of the model for changes in formulation variables and pressure. In chapter 4, we extended our model to a pilot-plant scale homogenizer and also relaxed the assumption of binary breakage. In the chapter 5, we improved the pressure dependance in our model and made an attempt at using the model for design.

## CHAPTER 2

### INVERSE POPULATION BALANCE EQUATION MODELING: SENSITIVITY TO MEASUREMENT ERRORS

In this chapter, we consider an inverse PBE modeling method developed by [84] and co-workers, which is based on the concept of self-similar solutions [52, 53, 85, 86]. Transient particle size distribution data is first tested for self-similarity, and then used for non-parametric reconstruction of the functions for drop breakup and the creation of daughter drops if the self-similarity property holds. This inverse PBE method has been applied to both simulated and experimental data for various dispersions prepared with turbulent agitation in well-mixed batch vessels [71, 72, 83, 95, 96, 122]. Because different combinations of single drop functions can provide agreement with the limited transient drop size distribution data typically available for estimation, the inverse problem is inherently ill-posed [84]. Consequently, function approximation results are expected to be highly sensitive to the quality and quantity of the input data.

Techniques for measuring emulsion drop size distributions include optical microscopy and various light scattering techniques. Dynamic light scattering (DLS) [97] allows for measurement of droplets in the 10 -1000 nm range, and is ideal for many pharmaceutical applications that target droplets in the 100 nm range. These small droplets cannot be observed by optical microscopy. In addition, DLS enables much larger sample volumes to be probed than is possible using optical microscopy. However, DLS measurements are subject to various errors that degrade data quality like sensor noise. Because larger drops scatter more strongly than small drops, DLS has a tendency to skew the size distribution towards larger drops. Dust particles can introduce artificial peaks at large drop sizes that may be difficult to remove. Automated signal filtering can inadvertently remove signals associated

with large droplets, while emulsion sample filtering can induce changes in the the drop size distribution due to shearing. The calculation of the autocorrelation function and subsequent inversion to produce the particle size distribution involves binning operations that reduce resolution. While numerous application studies of the inverse PBE approach have been reported, we are not aware of any investigations focusing on the effects of such input data errors.

In this chapter, we utilize a previously published model of a well-mixed batch emulsification vessel [96] to examine the effect of transient drop size distribution measurement errors on the quality of the function approximation results obtained with the inverse PBE method of Ramkrishna and co-workers. The remainder of the chapter is organized as follows. The PBE model and the inverse PBE method are described in sections 2.1 and 2.2, respectively. New results on the sensitivity of the PBE method to input data errors are presented and discussed in section 2.3. Finally, we summarize our main findings and discuss their implications for PBE modeling of drop size distributions in pharmaceutical emulsions prepared with high pressure homogenization in section 2.4.

## 2.1 Population Balance Equation Model

The population balance equation (PBE) describes the evolution of the drop size distribution that results from particulate processes such as formation, aggregation and breakup. We utilize a volume structure model in which drops are characterised by their volume. The population balance requires that for any volume element  $dv$ , the number of drops moving in and out of the element are balanced by drops accumulating within the element. Let  $n(v, t)dv$  represent the number of drops per unit volume of the dispersion at time  $t$  with volumes between  $v$  and  $v + dv$ . We neglect drop coalescence by assuming a small dispersed phase volume fraction and the presence of large amount of surfactant.

This formulation yields the following PBE for a well-mixed, batch vessel [19, 84]:

$$\frac{dn(v, t)}{dt} = -\Gamma(v)n(v, t) + \int_v^\infty \beta(v, v')\nu(v')\Gamma(v')n(v', t)dv' \quad (2.1)$$

where  $\Gamma(v)$  is the breakage rate (fraction of drops of volume  $v$  breaking per unit time),  $\beta(v, v')$  is the probability density function (probability of forming drops of volume  $v$  from breakage of drops of volume  $v'$ ), and  $\nu(v')$  is the number of daughter drops formed by breakage of drop of volume  $v'$ . The initial condition  $n(v, 0)$  is the number density of the coarse emulsion introduced to the vessel and can be measured experimentally.

For application of the inverse modeling approach of Ramkrishna and co-workers [84], the PBE model is conveniently reformulated in terms of the cumulative distribution rather than the number distribution as in (2.1). In this case, the PBE for a pure breakage process assumes the form:

$$\frac{\partial F(v, t)}{\partial t} = \int_0^\infty \Gamma(v')G(v, v')\partial_v F(v', t) \quad (2.2)$$

where  $F(v, t)$  is the cumulative volume fraction of drops of volume less than or equal to  $v$  at time  $t$ ,  $\Gamma(v)$  is the breakage rate of drops of volume  $v$ , and  $G(v, v')$  is the cumulative volume fraction of drops of volume less than or equal to  $v$  formed by breakage of drop of volume  $v'$ . The function  $G(v, v')$  combines the two functions  $\beta(v, v')$  and  $\nu(v')$  in (2.1).

The PBE model (2.2) is completed by specifying the breakage rate  $\Gamma(v)$  and the daughter drop distribution function  $G(v, v')$ . A wide variety of functional forms have been proposed for dispersed phase systems [84]. In this chapter, we employ the functions introduced in [96] for drop breakage in a well-mixed dispersion. While these functions were not determined from experimental data, the inverse PBE method has been extensively studied for this problem under the assumption of perfect input data. We will utilize these results as the basis for assessing the impact of input data errors on the quality of the function approximation results. The breakage rate function used in our analysis has the form [96]:

$$\Gamma(v) = 1.2 \exp[0.12(\ln v + 3.5) - 0.20(\ln v)^2 - 12.25] \quad (2.3)$$

The assumption of self-similarity allows the daughter drop distribution function to be represented compactly as:

$$G(v, v') = g(x) = g \left[ \frac{\Gamma(v)}{\Gamma(v')} \right] \quad (2.4)$$

We have used the following function in our analysis [96]:

$$g(x) = \frac{8}{3}\sqrt{x} - \frac{5}{3}x^{0.8} \quad (2.5)$$

## 2.2 Inverse Population Balance Equation Modeling

The objective of the inverse PBE modeling approach of Ramkrishna and co-workers [84, Chpt. 6] is to construct functions for single particle processes from transient measurements of the particle size distribution. A desirable feature of this methodology is that *a priori* specification of functional forms is not required. The concept of self-similarity is exploited repeatedly, starting with the assumption that the daughter drop distribution function can be represented as a function of the breakage rate function as in (2.4). While this functional form might appear to be highly restrictive, it subsumes power law relationships often used to describe drop breakage processes [72, 96]. The interested reader is referred elsewhere for a detailed treatment of self-similarity [84, Chpt. 6]. In this chapter, we investigate approximation of the breakage rate function  $\Gamma(v)$  and the daughter drop distribution function  $g(x)$  from transient drop volume distributions obtained by simulating the PBE model (2.2) with the functions in (2.3) and (2.4). This simulation approach allows direct comparison of the approximated and actual functions to assess the impact of input data errors on the effectiveness of the inversion procedure.

### 2.2.1 Breakage Rate Function

The calculation of the breakage rate function requires testing of the similarity hypothesis and then determination of the breakage function if the similarity hypothesis is valid [84,

96, Chpt. 6]. Curves of  $\ln t$  versus  $\ln v$  are plotted for different values of the cumulative distribution  $F$ . The similarity property can be tested by evaluating the arc lengths of different  $\ln t$  versus  $\ln v$  curves using the following formula:

$$s(x) = \int_{x_0}^x \left[ 1 + \left( \frac{dy}{dx} \right)^2 \right]^{1/2} dx \quad (2.6)$$

where  $x = \ln v$  and  $y = \ln t$ . The arc length calculation requires evaluation and integration of the first derivative. If a single arc length curve is obtained from the different  $\ln t$  versus  $\ln v$  curves, then the data is self-similar. Typically, self-similarity is validated by visual inspection of the arc length curves. We found that each  $\ln t$  versus  $\ln v$  curve must be fit to a different linear or quadratic equation to obtain acceptable results.

From the arc length equation (2.6), a relation for the complete  $\ln t$  versus  $\ln v$  curve can be obtained:

$$\frac{d \ln t}{d \ln v} = \left[ \left( \frac{ds}{d \ln v} \right)^2 - 1 \right]^{1/2} \quad (2.7)$$

This relation can be used to evaluate the partial derivative in the following equation, which allows calculation of the breakage function up to a multiplicative constant  $\gamma$ :

$$\Gamma(v) = \gamma \exp \left[ - \int_{\ln v_0}^{\ln v} \left( \frac{\partial \ln t}{\partial \ln v} \right)_F d \ln v \right] \quad (2.8)$$

where  $\gamma$  is the breakage function evaluated at the reference volume  $v_0$  used in the arc length calculations:  $\gamma = \Gamma(v_0)$ . The unknown constant  $\gamma$  is determined as part of the procedure for approximating the daughter drop distribution function.

### 2.2.2 Daughter Drop Distribution Function

The calculational procedure for the daughter drop distribution function utilizes the similarity variable defined as:

$$\xi = \frac{\Gamma(v)t}{\gamma} \quad (2.9)$$

where the ratio  $\Gamma(v)/\gamma$  is obtained from the breakage rate calculation (2.8). Application of the similarity transformation  $F(v, t) \rightarrow f(\xi)$  to the cumulative form of the PBE (2.2) yields the following equation for the similarity distribution  $\xi f'(\xi)$  [84, 96]:

$$\xi f'(\xi) = \int_0^1 \frac{\xi^2}{x^3} f' \left( \frac{\xi}{x} \right) \gamma g(x) dx \quad (2.10)$$

where  $x = \Gamma(v)/\Gamma(v')$  as in (2.4). This equation is the basis for determining the daughter drop distribution function  $g(x)$  and the unknown breakage constant  $\gamma$ .

As suggested in [96], the unknown product  $\gamma g(x)$  is expanded in terms of orthogonal basis functions chosen to be the modified Jacobi polynomials [1]:

$$\gamma g(x) = \sum_{i=1}^{nb} a_i G_i(x) = \sum_{i=1}^{nb} a_i x^\mu J_i(x) \quad (2.11)$$

Three basis functions were used for our analysis. We found that  $nb = 3$  was the minimum number of basis function required for approximating the distribution function without the need for regularization [96]. Because  $\xi f'(\xi) \sim \xi^\mu$  for  $\xi \approx 0$ , the power  $\mu$  can be obtained from the behavior of the self-similar distribution as  $\xi \rightarrow 0$ . We found that small, trial-and-error adjustments in this  $\mu$  value may produce improved distribution predictions. Once the product  $\gamma g(x)$  is determined via the procedure described below, the constant  $\gamma$  is readily determined since  $g(1) = 1$ .

The similarity variable  $\xi$  is discretized to generate  $\{\xi_i\}$  and the matrix  $X = \{X_{ij}\}$  associated with (2.10) is defined as:

$$X_{ij} = \int_0^1 \frac{\xi_i^2}{x^3} f' \left( \frac{\xi_i}{x} \right) G_j(x) dx \quad (2.12)$$

As suggested in [96], the similarity distribution  $\xi f'(\xi)$  was expanded in terms of gamma distributions:

$$\xi f'(\xi) = \sum_{k=1}^{n_{term}} A_k \xi^{\alpha_k - 1} \exp(-\beta_k \xi) \quad (2.13)$$

We used two-term expansions ( $n_{term} = 2$ ) for our analysis. The unknown parameters ( $A_k$ ,  $\alpha_k$ ,  $\beta_k$ ) of the expansion are determined from the known similarity distribution using non-linear regression. By substituting the expansion (2.13) into (2.12) and performing the necessary integration, an explicit formula for the elements  $X_{ij}$  can be derived [96]:

$$X_{ij} = \sqrt{2j} \sum_{k=1}^{n_{term}} A_k \sum_{m=1}^j (-1)^{m-1} \frac{(2j-m)!}{(m-1)!(j-m)!(j-m+1)!} \xi_i^{j-m+\mu} \frac{\gamma_c(\alpha_k + m - j - \mu, \beta_k \xi_i)}{\beta^{\alpha_k + m - j - \mu}} \quad (2.14)$$

where  $\gamma_c$  is the complementary incomplete gamma function.

Let the vector  $a$  contain the coefficients  $a_j$  of the expansion (2.11) and define the vector  $\Phi = \{\Phi_i\} = \xi_i f'(\xi_i)$ . Then the inverse problem arising from (2.10) can be written as:  $\Phi = Xa$ . This inverse problem is ill-posed in the sense that small changes in the similarity distribution  $\xi f'(\xi)$  can induce large changes in the approximated function  $\gamma g(x)$ . This difficulty is addressed by posing the inverse problem as a least-squares minimization problem:

$$\min_{a \in \mathbb{R}^{n_b}} \|Xa - \Phi\| \quad (2.15)$$

that is solved subject to the following constraints on the daughter distribution function:

$$g(x) > 0, \quad g'(x) \geq 0, \quad g'(1) = 0 \quad (2.16)$$

The first two constraints ensure that the distribution function is positive and monotonically increasing. The third constraint results from the assumption that breakup cannot produce

daughter drops of near zero volume. The minimization problem equation (2.15) can be rewritten as

$$\min_{a \in \mathbb{R}^{nb}} a^T X^T X a - 2a^T X^T \Phi \quad (2.17)$$

The least-squares problem (2.17) is solved by enforcing the constraints (2.16) at each discretization point  $\xi_i$  [96].

### 2.3 Simulation Results and Discussion

The number distribution form of the PBE model (2.1) was solved numerically by approximating the integral expression using Simpson's Rule with 500 equispaced node points, which was sufficient to obtain a converged solution. This discretization method was used primarily due to its simplicity and ease of implementation. The daughter drop distribution function  $G(v, v')$  (2.4) was converted to the form  $\beta(v, v')$  used in the number distribution PBE model. The resulting system of 500 nonlinear ordinary differential equations describing the evolution of the number distribution at each node point ( $v_i$ ) was solved using Matlab integration code `ode45`. A single simulation run was used to generate transient drop volume distribution data for the initial coarse distribution:

$$n(v) = \frac{1}{\sigma\sqrt{2\pi}} \exp\left(-\frac{a(v - \mu)^2}{2\sigma^2}\right) = \frac{1}{50\sqrt{2\pi}} \exp[-5000(v - \mu)^2] \quad (2.18)$$

Unless otherwise stated, the number distributions at six time points  $t = 5, 10, 15, 30, 60$  and 90 minutes were converted to cumulative distributions for the inverse algorithm [96]. These time points were chosen to concentrate data at small times when rapid changes were observed and to include a single data point at a large time when the cumulative distribution was changing very slowly. In the subsequent figures, result at only 4 time points are shown for better readability of the plots. For each test presented below, the cumulative distribu-

tions were manipulated before being used as input data to the inverse algorithm to mimic various types of measurement errors. Each data was judged to be self-similar by visual inspection of the arc length curves and allowed application of the inversion procedure. The approximate functions for the breakage rate  $\Gamma(v)$  and the daughter drop distribution  $g(x)$  were compared directly to the actual functions. The impact of measurement errors were further assessed by performing dynamic simulation with the approximate functions and comparing the computed cumulative distributions with the original distributions obtained with the actual functions.

### 2.3.1 “Perfect” Data

We first solved the inverse problem with six unaltered, transient drop volume distributions generated directly from the PBE model. This data was not manipulated by introducing measurement errors and was used to determine the upper limit of estimation performance. The term “perfect data” thus denotes data without any manipulation. Turbulent agitation reduced the mean drop size and produced a more monodispersed emulsion than the original coarse emulsion (Figure 2.1(a)). Good approximation results were obtained for both the breakage rate and the daughter distribution function (Figure 2.1(b)) over a wide range of drop volumes. PBE model simulation with the approximated functions produced good agreement with the actual cumulative (Figure 2.1(c)) and number (Figure 2.1(d)) distributions).

We recalculated the cumulative distributions using two other combinations of the breakage and daughter distribution functions to assess the impact of each function on prediction accuracy. When the approximate breakage function was combined with the actual daughter distribution function (Figure 2.2(a)), the cumulative distribution ( $t = 5$  min) was skewed towards larger drops for small drop volumes and skewed towards smaller drops for large drop volumes. These errors were a direct result of the breakage rate (Figure 2.1(b)), which was slightly underestimated for small drop volumes and overestimated for large drop vol-

umes. When the approximate distribution function was combined with the actual breakage function (Figure 2.2(b)), the cumulative distribution was skewed towards smaller drops for small drop volumes. This trend was caused by the distribution function being skewed towards smaller  $x$  values (Figure 2.1(b)), which corresponds to a larger distribution of small drops.

The interpretation of results is more complicated when both approximate functions were used to generate the cumulative distributions, which is the case of primary interest. The individual errors obtained with the approximate breakage function (Figure 2.2(a)) and the approximate distribution function (Figure 2.2(b)) were largely cancelled when the approximate functions were combined to generate the final distribution (Figure 2.2(c)). However, the effects of the approximation errors were more evident in the transient prediction (Figures 2.1(c), 2.1(d)). The distributions were skewed towards smaller drops at small times due to underprediction of the distribution function, while they were skewed towards larger drops at large times due to underprediction of the breakage rate.

### 2.3.2 Noisy data

To investigate the impact of measurement noise, we corrupted the drop volume distribution data with artificial noise as follows:

$$\bar{n}(v, t) = n(v, t) + \nu(r - 0.5)n(v, t) \quad (2.19)$$

where  $n(v, t)$  is the number distribution data obtained with the actual functions (see Figure 2.1(a)),  $r$  is a random number between 0 and 1,  $\nu = 0.3$  and  $\bar{n}(v, t)$  is the noisy number distribution data used to generate the input data for the inverse algorithm. We utilized uniform rather than normal noise to ensure that the noisy data  $\bar{n}(v, t)$  remained positive, which is expected from any measurement device.

First we solved the inverse problem with six cumulative distributions generated from the noisy number distributions at  $t = 5, 10, 15, 30, 60,$  and  $90$  minutes (Figure 2.3(a)). Figure

2.4(a) shows the associated cumulative distributions. The noisy cumulative distributions had fewer large drops than the noise-free distributions, leading to underestimation of the breakage rate at large drop volumes (Figure 2.3(b)). More difficult to explain was the behavior of the daughter distribution function, which produced a larger number distribution of small drops and a smaller number distribution of large drops than the actual function (Figure 2.3(b)). These approximation errors were manifested in the predicted cumulative (Figure 2.3(c)) and number (Figure 2.3(d)) distributions. Both functions were important at short times, thereby yielding overprediction of small drops and underprediction of very large drops. At longer times the breakage rate became dominant, and a larger proportion of large drops was predicted compared to the original noise-free data.

We repeated the noisy data test with twelve cumulative distributions generated from the noisy number distributions at  $t = 5, 7.5, 10, 12.5, 15, 22.5, 30, 45, 60, 75, 90$  and 105 minutes with the expectation that more transient data would improve the function approximation results. The daughter distribution function was significantly improved, while the breakage rate was slightly degraded (Figure 2.4(b)). Consequently, only modest improvements in transient distribution predictions at short times were obtained (Figure 2.4(c), 2.4(d)). Because the noisy cumulative distributions were skewed towards smaller drops, these results suggest that the collection of more transient data will prove largely ineffective if the data is uniformly skewed.

### 2.3.3 Skewed Data

Available technologies such as dynamic light scattering (e.g. [97]) have a tendency to skew measured drop size distributions. To examine the impact of such measurement errors, we skewed the drop volume distribution data as follows:

$$\bar{n}(v, t) = n(\bar{v}, t), \quad \bar{v} = v \pm \delta v \quad (2.20)$$

where  $n(v, t)$  is the number distribution data obtained with the actual functions (Figure 2.1(a)),  $\bar{v}$  is the skewed volume.  $\delta$  determines the amount of skewness, the sign determines the direction of skewness, either towards smaller drops (negative) or larger drops (positive), and  $\bar{n}(v, t)$  is the skewed distribution. Skewed distributions at  $t = 5, 10, 15, 30, 60,$  and  $90$  minutes were used as input data to the inverse algorithm.

First, we examined skewing towards larger drops with  $\delta = +0.0005$ , which produced number distributions that increasingly deviated from the original distributions at large drop volumes (Figure 2.5(a)). Substantial underestimation of the breakage rate was observed, while only small errors were obtained in the daughter distribution function (Figure 2.5(b)). The predicted cumulative distributions consistently trailed the actual distributions (Figure 2.5(c)) in that the number of large drops was generally overpredicted. This behavior is easily interpreted from the number distribution predictions (Figure 2.5(d)), which show an overprediction of small drops at small times and a consistent overprediction of large drops.

Next, the number distributions were skewed towards smaller drops with  $\delta = -0.0005$ . Because the number distributions were more skewed towards small drops at large drop volumes (Figure 2.6(a)), the breakage rate function only agreed with the actual function at very small drop volumes (Figure 2.6(b)). Interestingly, the daughter distribution was significantly underestimated except at large drop volumes where the data was most skewed (Figure 2.6(b)). The predicted cumulative distributions led the actual distributions until the approximate breakage function approached the actual function at large times (Figure 2.6(c)). The predicted number distributions produced a larger number of small drops than the actual distributions (Figure 2.6(d)), which was consistent with overprediction of the breakage rate.

#### **2.3.4 Dust Particles**

Drop size distribution measurements produced by dynamic light scattering are sensitive to contaminants such as dust particles that create artificial peaks at large drop sizes [97].

For emulsions, dust particles are not easily removed by filtering because shearing can cause drop breakage. While dust peaks can be eliminated by restricting the size range analyzed, this approach requires *a priori* knowledge about the drop size distribution. Therefore, we investigated the effect of artificial peaks in the number distribution data at large drop volumes. For simplicity, a single peak was assumed to be normally distributed about a large drop volume and to remain constant with time (Figure 2.7(a)). This peak caused significant underestimation of the breakage rate (Figure 2.7(b)) and produced a daughter distribution that predicted a larger proportion of small drops (Figure 2.7(b)). The tradeoff between these two errors was evident in the predicted cumulative (Figure 2.7(c)) and number (Figure 2.7(d)) distributions, where the daughter distribution function was dominant for small drop volumes and the breakage rate function was dominant for large drop volumes. The breakage function became dominant at longer times when the predicted distributions trailed the actual distributions due to underestimation of drop breakage.

### 2.3.5 Binned Data

In the previous simulation tests, the distribution data was essentially a continuous function of the drop volume due to the large number (500) of node points used for numerical solution. By contrast, drop size distributions measured by dynamic light scattering (DLS) have limited resolution due to binning operations. We have used DLS (Brookhaven Instruments) to measure drop size distributions for mineral oil ( $\approx 0.04$  wt%) in water emulsions with Pluronic F-68 ( $\approx 0.008$  wt%) as the surfactant. Initial coarse emulsions prepared using a stator-rotor device (*Ultra-Turrax, T 25 basic*, IKA Works, Inc.) were introduced to a high pressure homogenizer (*Emulsiflex C-3*, Avestin, Inc.) operated at 25,000 psig. The mean and variance of the coarse drop size distribution (Figure 2.8(a)) were significantly reduced by a single homogenization pass (Figure 2.8(b)). However, the instrument produced low resolution distributions due to the small number of bins used.

We conducted a final set of simulation tests to investigate the impact of drop size binning on the inverse algorithm. Number drop distributions were used as input data by holding the distribution constant at the mean volume across each bin. Each number distribution was converted to a cumulative distribution from which volume values were interpolated to generate the  $\ln t$  vs  $\ln v$  plots. Then the inversion procedure was implemented as described earlier. Initially, 10 bins were used to mimic the DLS experimental results (Figure 2.9(a)). The breakage rate was underestimated at large drop volumes, and the daughter distribution function exhibited errors at intermediate volumes (Figure 2.9). Consequently, the predicted cumulative distributions (Figure 2.9(c)) trailed the actual continuous distributions. The number distributions (Figure 2.9(d)) showed that a greater number of large drops are predicted due to the underestimation of the breakage rate.

We repeated the test with 50 bins to determine if the continuous data results could be recovered (Figure 2.10). While the breakage rate was estimated slightly more accurately than with 10 bins, the daughter distribution function exhibited larger errors at large drop volumes (Figure 2.10). As a result, the predicted cumulative distributions (Figure 2.10(c)) were only slightly improved compared to ten bins (Figure 2.9) and significantly degraded compared to continuous data (Figure 3.5). The number distributions (Figure 2.10(d)) showed underprediction of small drops and overprediction of large drops, especially at long times. To validate the binning procedure, we repeated the test with 200 bins (Figure 2.11). The breakage rate and daughter distribution functions (Figure 2.11), the cumulative distributions (Figure 2.11(c)), and the number distributions (Figure 2.11(d)) compared favorably to those obtained with continuous data (Figure 3.5). Very close agreement was obtained when 500 bins were used (results not shown). Taken together, these results suggest that the inverse method can be rather sensitive to data binning.

## 2.4 Conclusions and Future Work

We investigated the impact of measurement errors in transient particle size distributions on the inverse population balance equation modeling method of Ramkrishna and co-workers. A previously published model of liquid-liquid dispersion drop volume evolution in a turbulently agitated batch vessel was used to generate transient distribution data, which were subjected to various types of errors before being used as input data to the inverse algorithm. The quality of the inversion results were assessed by comparing the estimated breakage rate and daughter distribution functions, as well as predicted distributions, to the original model.

We found that most errors considered degraded estimation of the breakage rate function at large drop volumes, presumably due to the limited data available for large drops in the transient distributions used as input data. The daughter distribution function also exhibited significant errors for most of the cases considered. However, the breakage function, and to a lesser extent the distribution function, often showed good agreement with the actual functions at small drop volumes. Consequently, predicted distributions tended to be more accurate at longer times when there was a preponderance of small drops due to repeated breakage. Our results suggest that the inverse algorithm can generate PBE functions that allow sufficiently accurate prediction of final drop size distributions despite errors in measured distributions used as input data.

Our long-term goal is to develop inverse-based methods for extracting PBE model functions of emulsion drop breakage and coalescence in high-pressure homogenization. This future work will require modification of the inverse method presented because homogenization is not properly modeled as a well-mixed, batch process. However, the sensitivity analysis techniques presented in this chapter will provide a suitable framework for assessing the impact of distribution measurement errors on the inversion procedure.

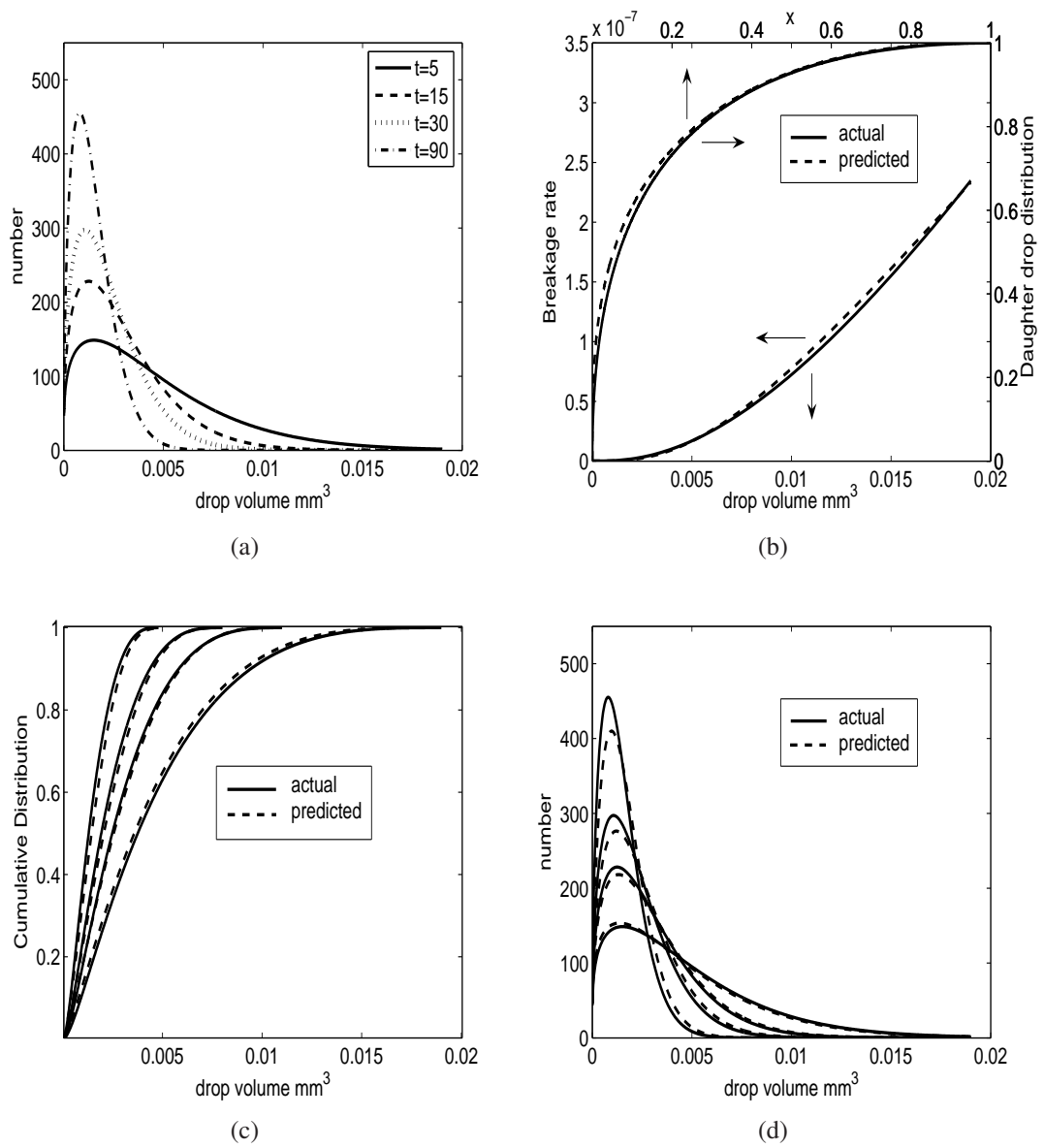
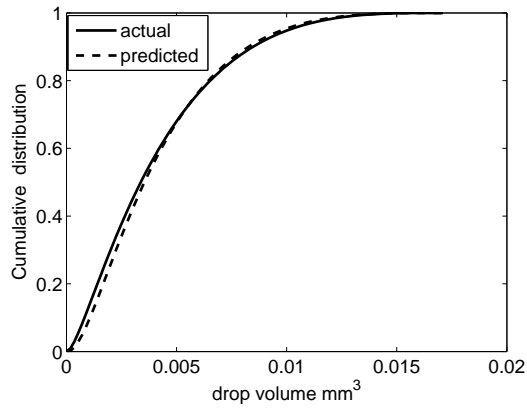
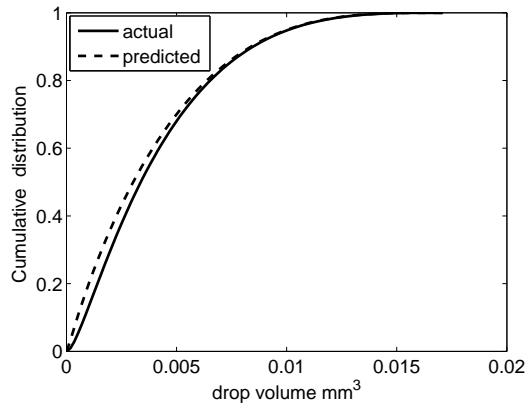


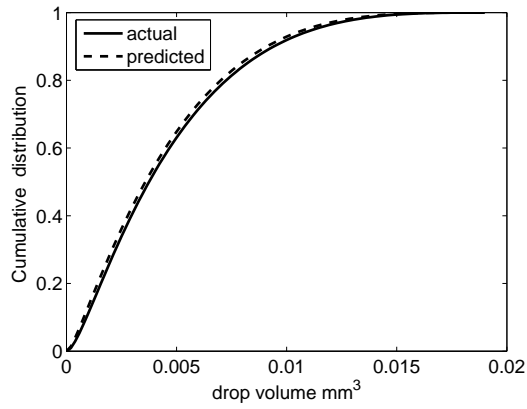
**Figure 2.1.** Inverse population balance modeling results for perfect drop volume distribution data. (a) Transient number drop distributions. (b) Predicted and actual drop breakage rate and daughter drop distribution functions. (c) Predicted and actual transient cumulative drop distributions. (d) Predicted and actual transient number drop distributions.



(a)



(b)



(c)

**Figure 2.2.** Effect of the drop breakage and daughter drop distribution functions on the predicted cumulative distribution ( $t = 5$  min). (a) Estimated breakage function and actual distribution function. (b) Actual breakage function and estimated distribution function. (c) Estimated breakage and distribution functions.

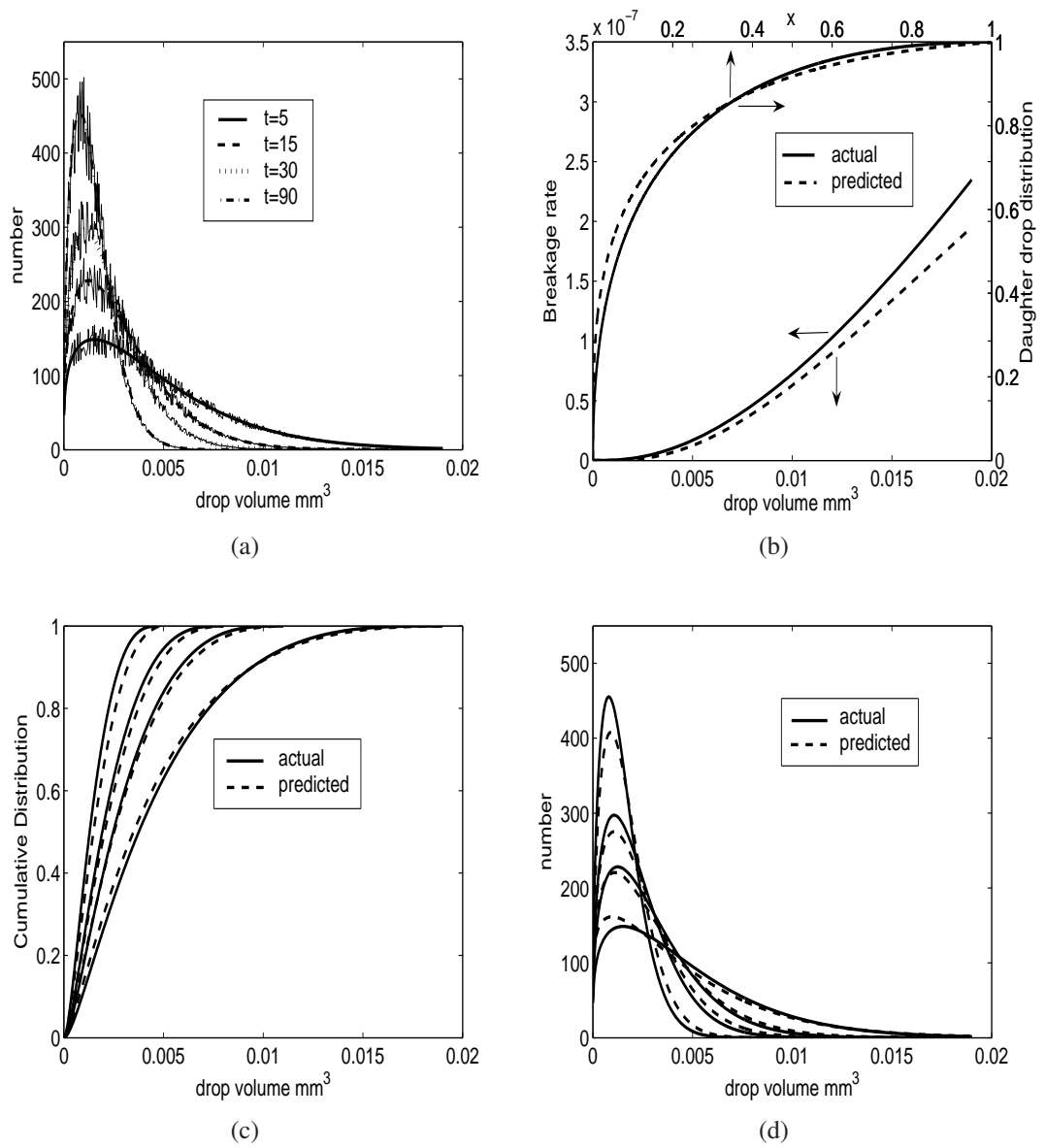


**Figure 2.3.** Inverse population balance modeling results with six noisy drop volume distributions. (a) Noisy and actual transient number drop distributions. (b) Predicted and actual drop breakage rate and daughter drop distribution functions. (c) Predicted and actual transient cumulative drop distributions. (d) Predicted and actual transient number drop distributions.

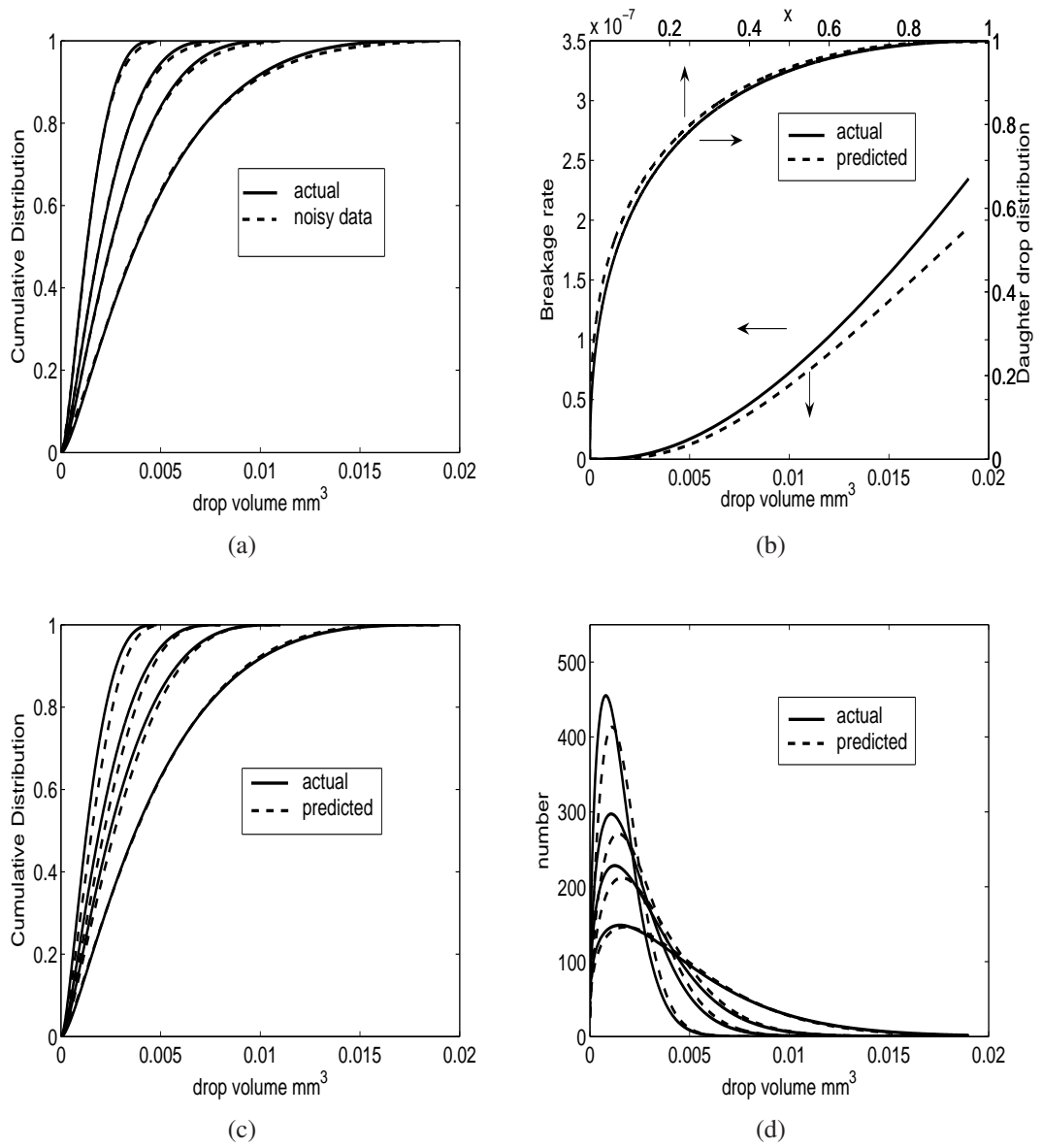


**Figure 2.4.** Inverse population balance modeling results with twelve noisy drop volume distributions. (a) Noisy and actual transient cumulative drop distributions. (b) Predicted and actual drop breakage rate and daughter drop distribution functions. (c) Predicted and actual transient cumulative drop distributions. (d) Predicted and actual transient number drop distributions.

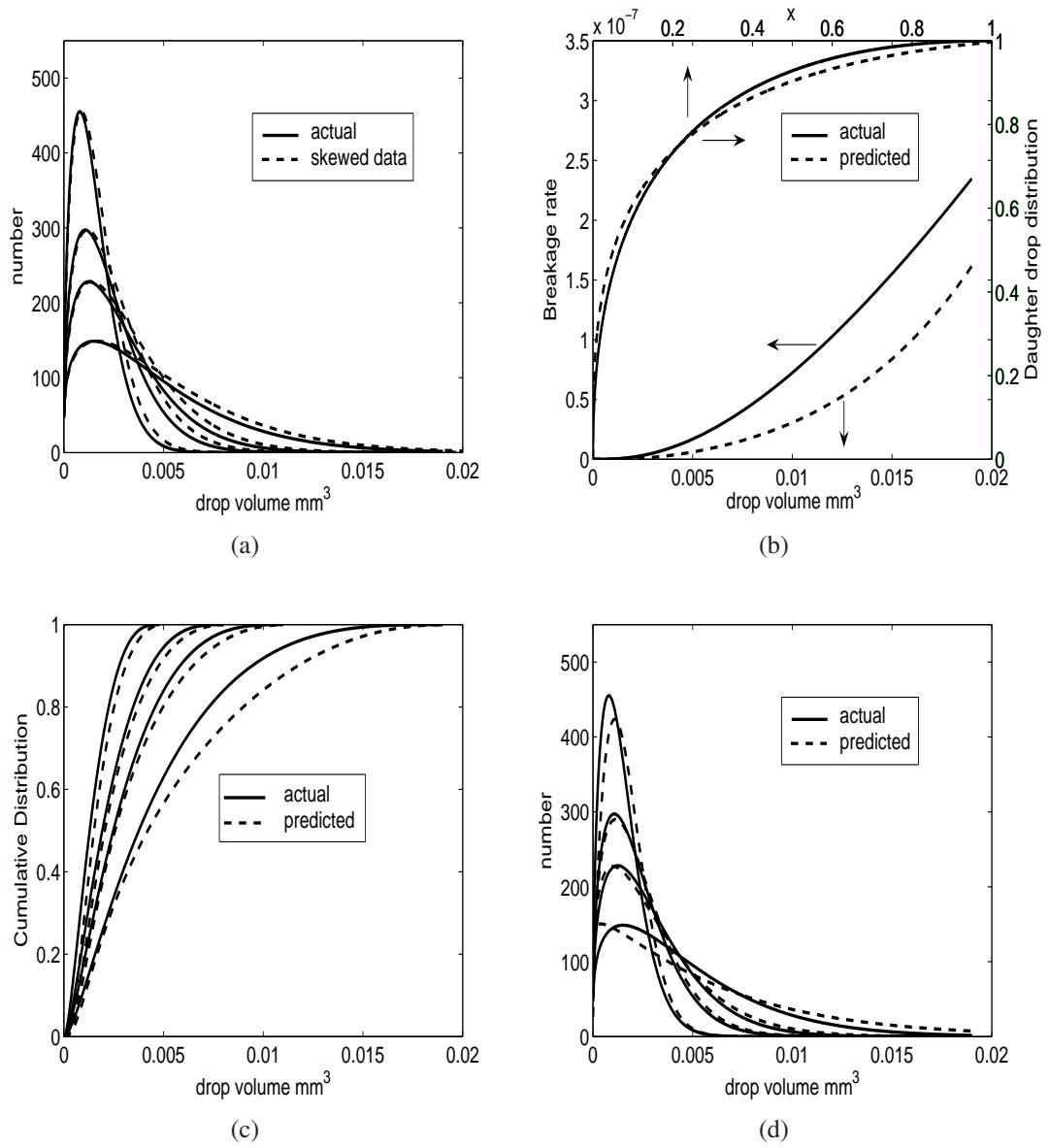


**Figure 2.5.** Inverse population balance modeling results with transient drop volume distributions skewed towards larger drops. (a) Skewed and actual transient number drop distributions. (b) Predicted and actual drop breakage rate and daughter drop distribution functions. (c) Predicted and actual transient cumulative drop distributions. (d) Predicted and actual transient number drop distributions.

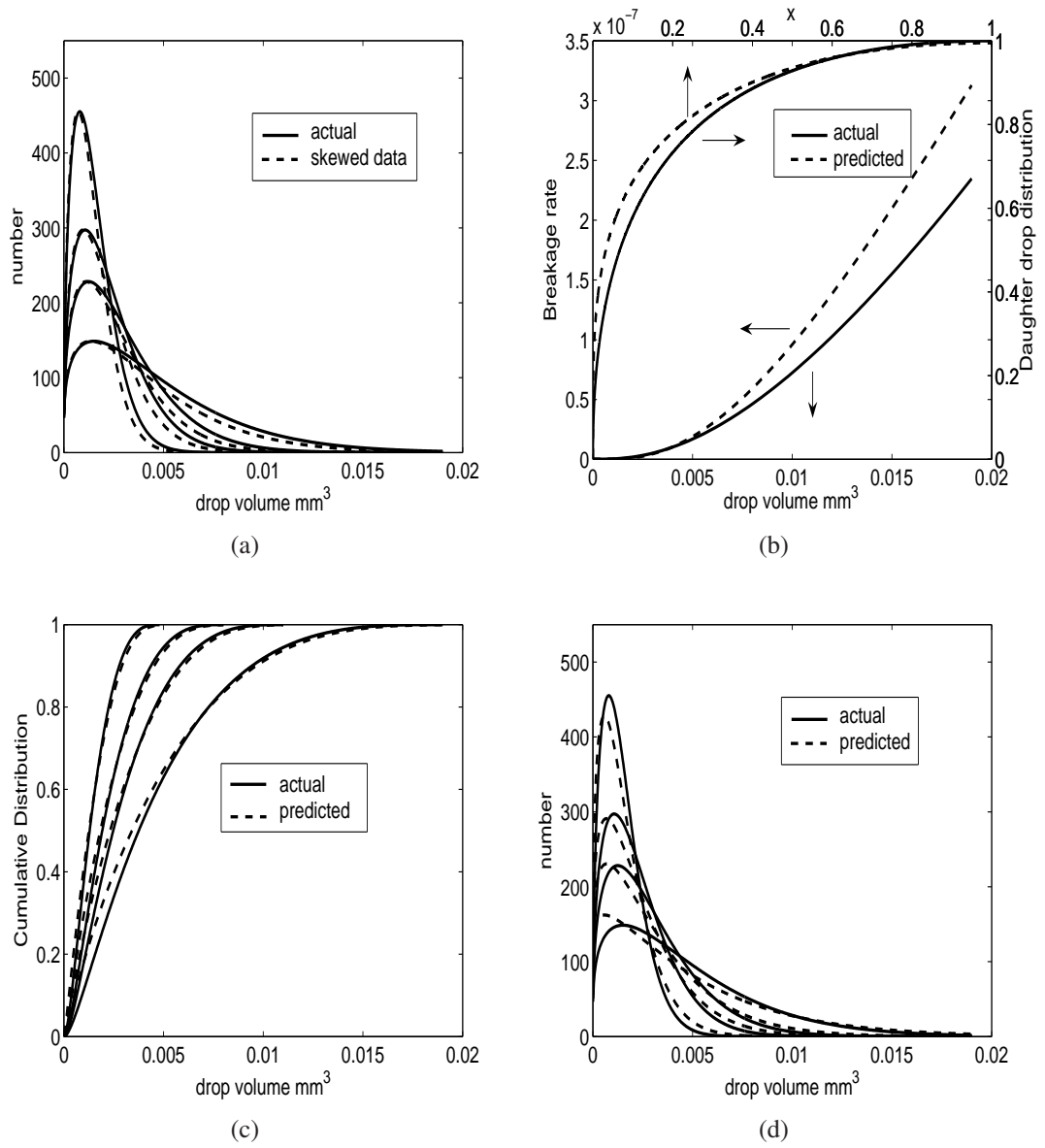


**Figure 2.6.** Inverse population balance modeling results with transient drop volume distributions skewed towards smaller drops. (a) Skewed and actual transient number drop distributions. (b) Predicted and actual drop breakage rate and daughter drop distribution functions. (c) Predicted and actual transient cumulative drop distributions. (d) Predicted and actual transient number drop distributions.

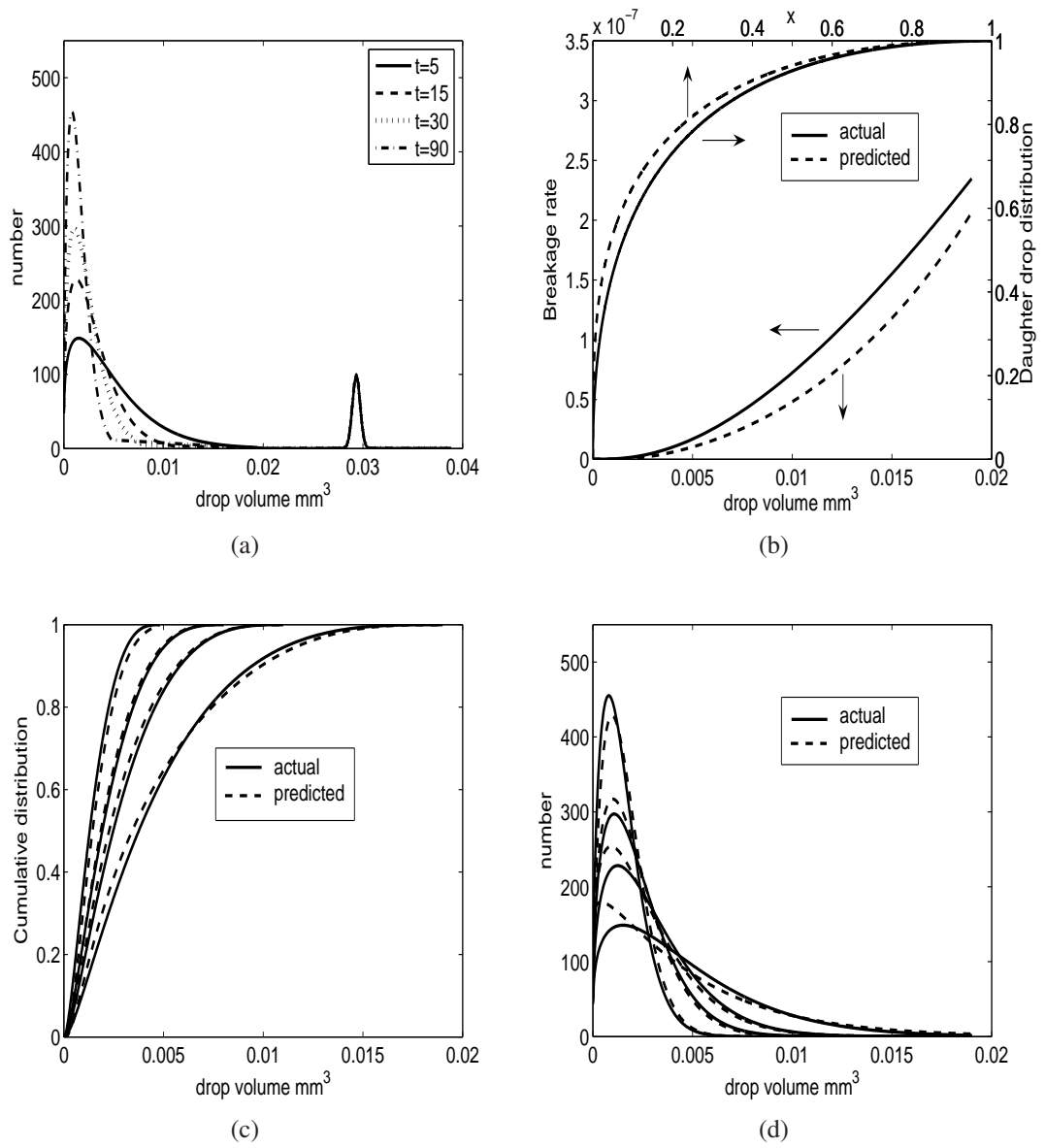


**Figure 2.7.** Inverse population balance modeling results with transient drop volume distributions skewed by dust peak. (a) Skewed transient number drop distributions. (b) Predicted and actual drop breakage rate and daughter drop distribution functions. (c) Predicted and actual transient cumulative drop distributions. (d) Predicted and actual transient number drop distributions.

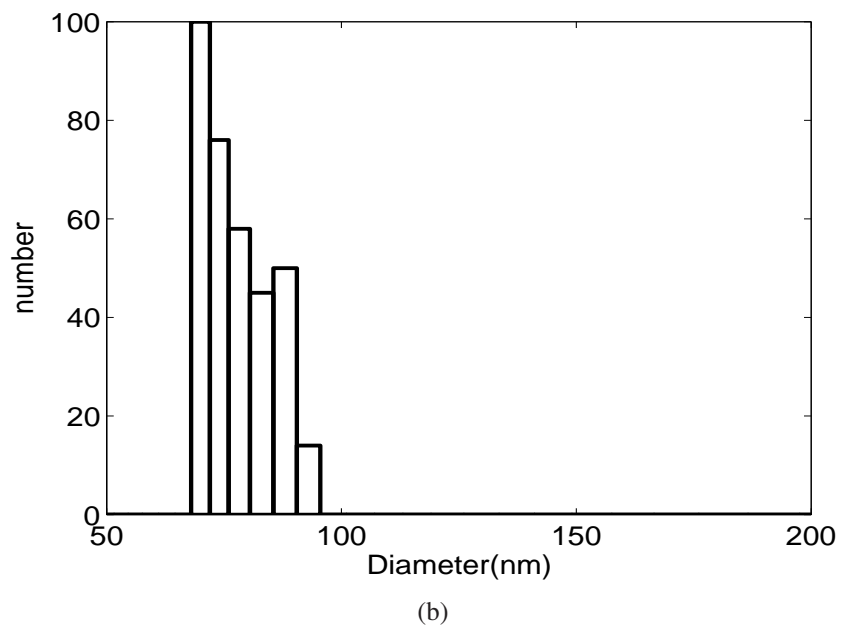
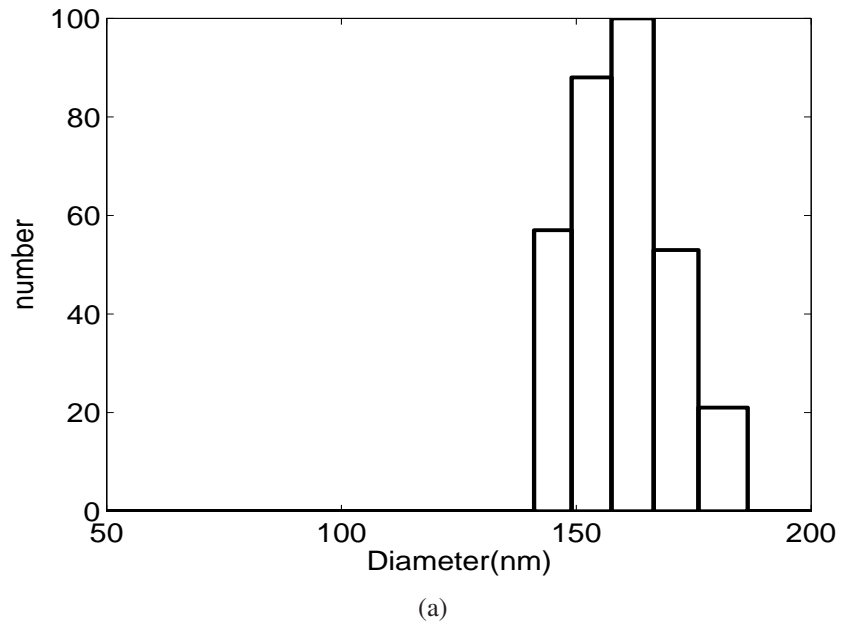


**Figure 2.8.** Drop size distribution measurements obtained with dynamic light scattering for a mineral oil in water emulsion with Pluronic F-68 as the surfactant. (a) Results for a coarse emulsion obtained with a stator-rotor device. (b) Results for a processed emulsion obtained with a single pass of a high-pressure homogenizer.

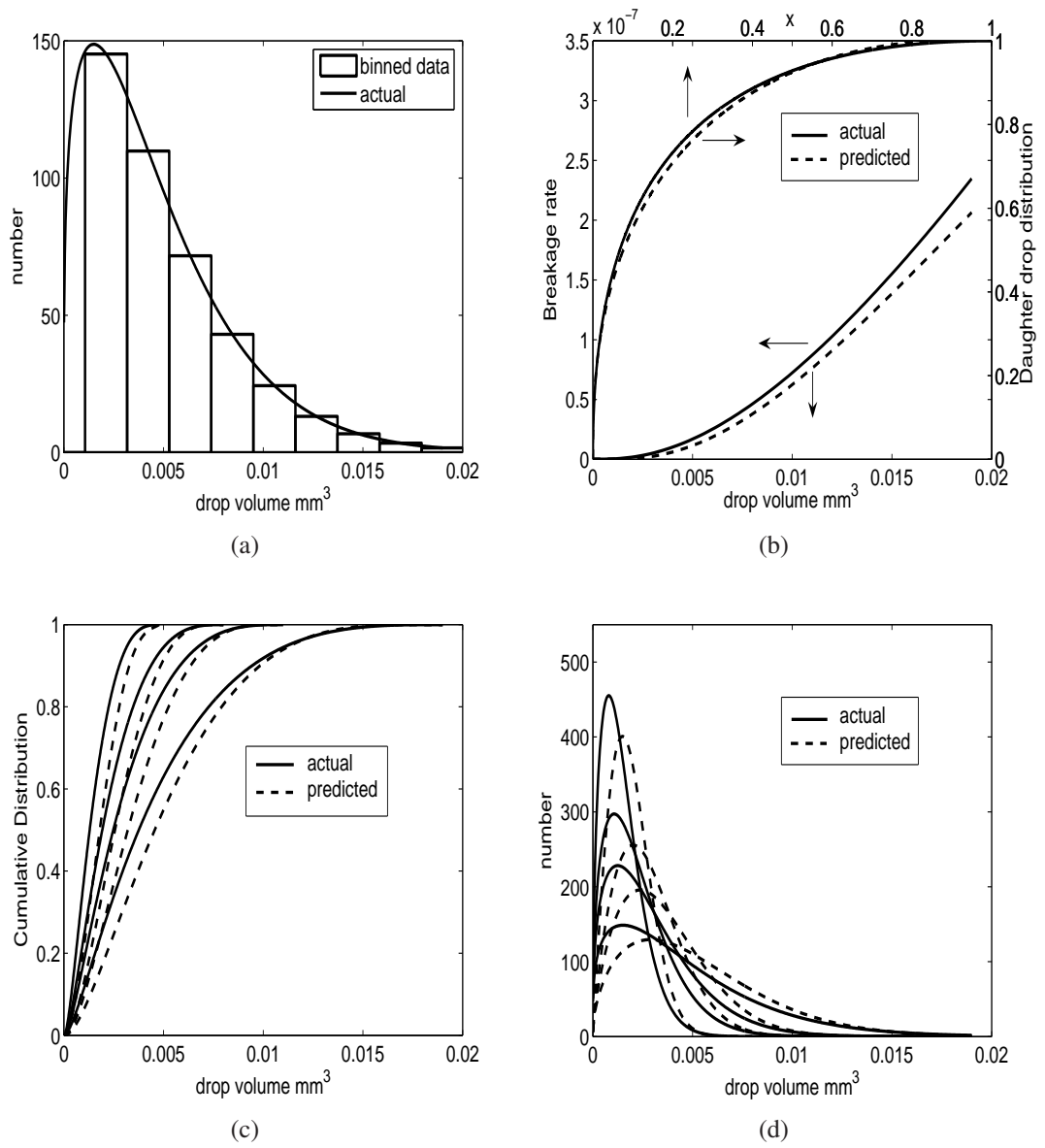


**Figure 2.9.** Inverse population balance modeling results with transient drop volume distributions represented by 10 bins. (a) The binned transient number drop distribution at  $t = 5$  min. (b) Predicted and actual drop breakage rate and daughter drop distribution functions. (c) Predicted and actual transient cumulative drop distributions. (d) Predicted and actual transient number drop distributions.

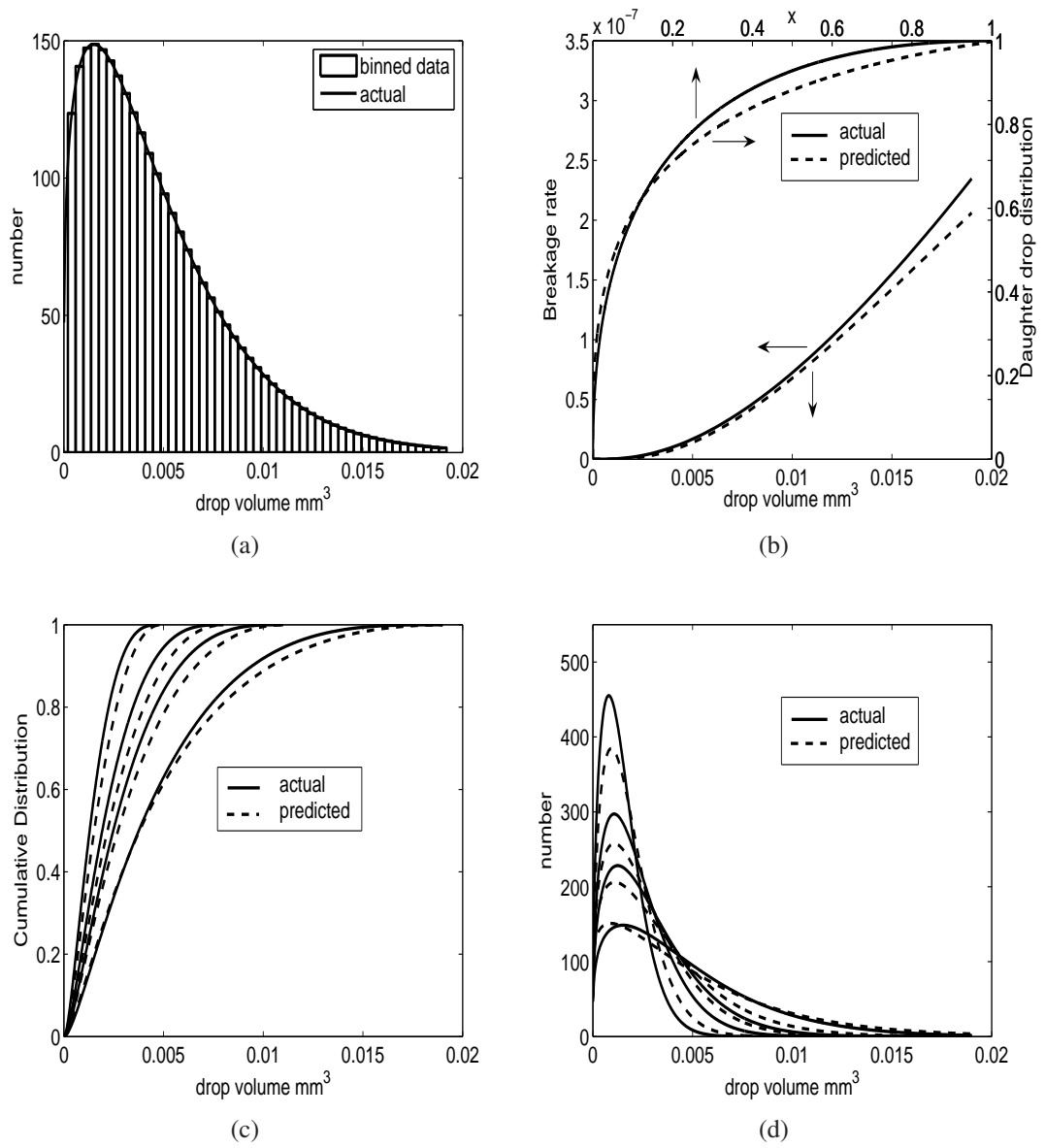


**Figure 2.10.** Inverse population balance modeling results with transient drop volume distributions represented by 50 bins. (a) The binned transient number drop distribution at  $t = 5$  min. (b) Predicted and actual drop breakage rate and daughter drop distribution functions. (c) Predicted and actual transient cumulative drop distributions. (d) Predicted and actual transient number drop distributions.

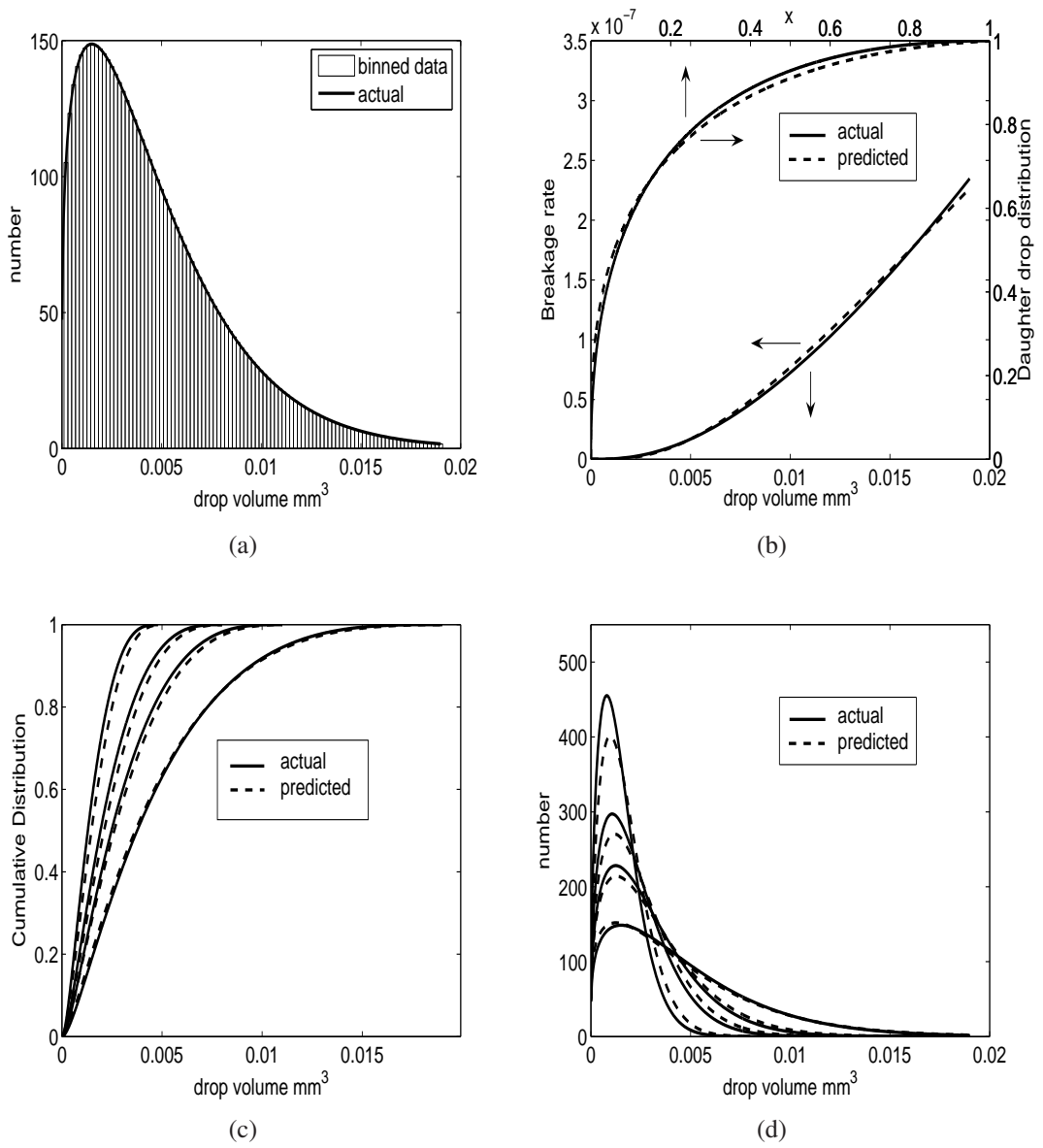


**Figure 2.11.** Inverse population balance modeling results with transient drop volume distributions represented by 200 bins. (a) The binned transient number drop distribution at  $t = 5$  min. (b) Predicted and actual drop breakage rate and daughter drop distribution functions. (c) Predicted and actual transient cumulative drop distributions. (d) Predicted and actual transient number drop distributions.

## **CHAPTER 3**

### **EXPERIMENTAL STUDIES AND POPULATION BALANCE EQUATION MODELS FOR BREAKAGE PREDICTION OF EMULSION DROP SIZE DISTRIBUTIONS**

In this chapter, we develop a PBE model for pure drop breakage processes by fitting model parameters to data collected from high-pressure homogenization experiments and evaluate model extensibility over a range of emulsion formulation and homogenizer operating variables. Homogenizer flow regimes are investigated using computational fluid dynamics (CFD) to better understand relevant drop breakage mechanisms and to motivate development of two mechanistic breakage functions. Nonlinear least-squares optimization is used to estimate adjustable parameters in breakage rate functions from measured drop volume distributions. Model extensibility is evaluated by comparing predictions generated with the base case parameters to drop volume distributions measured for different dispersed phase volume fractions, interfacial tensions, continuous phase viscosities, and homogenizer pressures.

### **3.1 Experimental Methods**

#### **3.1.1 Materials**

We used soybean oil (Spectrum Organic) as the dispersed phase, nanopure water as the continuous phase, and the non-ionic surfactant Pluronic F-68 (Sigma Aldrich) as the emulsifier. The base case emulsion consisted of 0.5wt% oil and 0.1wt% surfactant with the remainder water (Table 3.1). Relatively low oil and high surfactant concentrations were used to minimize the possibility of coalescence, an assumption tested experimentally

through a specific coalescence experiment (see section 3.3.2). Emulsions were prepared at concentrations different than the base case listed in Table 3.2 to test extensibility of the PBE model for varying bulk emulsion properties. The dispersed phase volume fraction was changed by adjusting the amount of oil, and the interfacial tension was changed by adjusting the amount of surfactant. To change the continuous phase viscosity, varying amounts of sucrose (Fisher Scientific) were added to the nanopure water.

### **3.1.2 Emulsion Preparation**

Emulsions were prepared using a two-step process. First about 100 ml of coarse pre-emulsion was prepared by mixing the chemical ingredients in a stator-rotor device (Ultra-Turrax Model T25, Rose Scientific Ltd.) at 13000 rpm for 1 minute (Table 3.1). Approximately 5 ml of the pre-emulsion was sampled for measuring the drop size distribution (see below). The pre-emulsion was then processed in a high-pressure homogenizer (Emulsiflex C-3, Avestin Inc.) where the liquid was pressurized to 10000 Psig (68.95 MPa) and then expanded through a narrow valve gap to create turbulent shear conditions favoring drop breakage. Multiple passes each approximately 2 min long were performed by reprocessing the emulsion obtained from the previous homogenizer pass. Five passes were performed for each experiment, and after each pass 5 ml of the emulsion was sampled for drop size distribution measurement. Experiments were also performed at different pressures (5000–20000 Psig) than the base case value to test extensibility of the PBE model (Table 3.2).

### **3.1.3 Emulsion Characterization**

Drop size distributions were measured using a static light scattering device (Coulter LS230 Particle Size Analyzer, Beckman Coulter). Optical microscopy (Olympus IX71 Inverted Microscope, Olympus) at a magnification of 20x and 40x was used to visually analyze drop sizes. Oil-water interfacial tensions were measured by drop shape analysis (KRUSS Instruments Model DSA-10 Tensiometer, KRUSS) at 25°C. Continuous and dispersed phase viscosities were measured using a Ubbelohde type capillary viscometer

(Model CT-1000, Canon Instruments Company) at 25°C. We found that large amounts of added sucrose designed to vary the continuous phase viscosity also slightly changed the interfacial tension. This issue is discussed further in the results section.

## **3.2 Theory**

### **3.2.1 Computational Fluid Dynamics**

A computational fluid dynamics (CFD) study was performed to better understand the flow field near the homogenizer valve. Because our goal was to identify possible turbulent mechanisms for drop breakage rather than to model the effects of inhomogeneous flow fields on drop breakage, the CFD computations were performed separately from the PBE model solution. The interested reader is referred elsewhere for CFD studies in which the PBE model is coupled to the flow field calculations [25, 32, 43, 46, 121].

Because our intention was to analyze bulk flow fields and not to track droplets, only continuous phase properties were considered under the assumption that the flow properties of our very dilute emulsions were dictated by the continuous phase fluid (water). The CFD analysis was restricted to a two-dimensional axisymmetric representation of the homogenizer valve near the narrow gap shown in Figure 3.3 [45, 57, 69]. The geometry was meshed using Gambit v2.2.30, and the flow field calculations were performed using Fluent v6.2.16 [34]. Interactions between the water liquid and vapor phases were captured using the Fluent cavitation model. The standard  $k$ - $\epsilon$  model was used for turbulence with no-slip boundary condition at the walls, and pressure-velocity coupling was captured using the SIMPLEC algorithm. A constant velocity of 0.42 m/s calculated from the homogenizer flow rate and the valve gap was introduced normal to the inlet plane, and the outlet pressure was set to 950 psig (6.5 MPa) since only a truncated section of the homogenizer was considered. The numerical solution was considered converged when the normalized residuals were less than  $10^{-5}$  and subsequent iterations did not change the flow field results.

### 3.2.2 Population Balance Equation Model

The analysis in this chapter is restricted to pure breakage processes under the assumption of negligible drop coalescence [99]. Under this assumption, the population balance equation for a batch system can be written as [16, 18, 19],

$$\frac{\partial n(v, t)}{\partial t} = -g(v)n(v, t) + \int_v^\infty \beta(v, v')\nu(v')g(v')n(v', t)dv' \quad (3.1)$$

where:  $n(v, t)dv$  is the number of drops with volume in the range  $[v, v + dv]$  per unit volume of the dispersion;  $g(v)$  is the breakage rate representing the fraction of drops of volume  $v$  breaking per unit time;  $\nu(v)$  is the number of daughter drops formed by breakage of a mother drop of volume  $v$ ; and  $\beta(v, v')$  is the daughter drop distribution function representing the probability of forming a daughter drop of size  $v$  from breakage of a mother drop of size  $v'$ . We model the high-pressure homogenizer as a well-mixed batch system in which the initial drop volume distribution is the measured distribution of the coarse pre-emulsion, and each pass corresponds to one dimensionless time unit. Our particle size analyzer provided measurements of the volume percent distribution  $n_p(v, t)$  rather than the number density  $n(v, t)$  as in PBE model (3.1). Consequently, the PBE model was reformulated in terms of volume percent distribution using the following relation based on the assumption of spherical drops consistent with experiments,

$$n(v, t) = \frac{V_{tot}n_p(v, t)}{v} \quad (3.2)$$

where  $V_{tot}$  is the conserved total volume of the drops. Simple manipulations produced the following alternative form of the PBE model:

$$\frac{\partial n_p(v, t)}{\partial t} = -g(v)n_p(v, t) + v \int_0^\infty \frac{g(v')\nu(v')\beta(v, v')n_p(v', t)}{v'}dv' \quad (3.3)$$

The PBE model (3.3) contains three breakage kernels ( $g(v)$ ,  $\beta(v, v')$ ,  $\nu(v)$ ) that must be specified to generate predictions. To our knowledge, mechanistic functions are not available for the number of drops formed upon breakage  $\nu(v)$  and the daughter drop distribution

$\beta(v, v')$ . Although the breakage of mother drops into multiple daughter drops has been reported by some investigators [50,95, 109, 113], we have assumed binary breakage such that  $\nu(v) = 2$  for simplicity and to examine the possible limitations of assuming that multiple breakage events can be modeled as a series of binary breakage events. We further assumed that  $\beta(v, v')$  follows the truncated normal distribution such that breakage has the highest probability of forming two equally sized daughter drops [63, 92, 101]:

$$\beta(v, v') = \frac{2.4}{v'} \exp \left[ -4.5 \frac{(2v - v')^2}{(v')^2} \right] \quad (3.4)$$

We limited our consideration of the breakage rate  $g(v)$  to two mechanistic functions that explicitly depend on the physical properties of the emulsion and allowed the resulting PBE models to account for chemical composition variations. The first function  $g_1(v)$  is a modified version of two previously proposed functions [18, 19] which were derived assuming that breakage results from drop collision with turbulent eddies. Unlike the breakage function proposed by Chen *et al.* [18], our function does not account for the small effect of the dispersed phase viscosity, but the breakage time  $t_B$  is assumed to be dependent on drop volume rather than being constant:

$$t_B = c_1 v^{2/9} \left( \frac{\epsilon}{\rho_d} \right)^{-1/3} \quad (3.5)$$

The breakage function was specialized to high-pressure homogenizers by using the following relation between the energy dissipation rate  $\epsilon$  and the homogenization pressure  $P$  [9, 10, 27, 28, 116]:

$$\epsilon = c_2 P^{3/2} v^{-1/3} \rho_d^{-3/2} \quad (3.6)$$

Following the procedure in Chen *et al.* [18], the following breakage rate function was derived,

$$g_1(v) = K_1 v^{-1/3} P^{1/2} \rho_d^{-1/2} \exp \left[ -\frac{K_2 \sigma (1 + \phi)^2}{v^{1/3} P} \right] \quad (3.7)$$

where  $K_1$  and  $K_2$  are parameters determined from measured drop size distributions (see below). Note that the breakage rate depends on the homogenizer pressure  $P$  and bulk emulsion properties including the dispersed phase volume fraction  $\phi$ , the dispersed phase density  $\rho_d$ , and the interfacial tension  $\sigma$ .

The second breakage rate function  $g_2(v)$  accounts for drop breakage resulting from turbulent shear. The derivation shown in the Appendix A produces the following functional form,

$$g_2(v) = K_3 \left( \frac{2}{\pi} \right)^{1/2} \left( \frac{P^{3/4}}{\eta_d^{1/2} \rho_d^{1/4} v^{1/6}} \right) \exp \left( \frac{-2K_4 \sigma^2 \lambda}{\eta_c P^{3/2} \rho_d^{-1/2} v^{1/3}} \right) \quad (3.8)$$

where  $\lambda = \frac{\eta_d}{\eta_c}$  and  $K_3$  and  $K_4$  are adjustable constants. In addition to depending on the same emulsion properties as  $g_1(v)$ , the turbulent shear function  $g_2(v)$  also depends on the continuous phase viscosity  $\eta_c$  and the dispersed phase viscosity  $\eta_d$ .

A variety of numerical techniques have been developed for solving PBE models of particulate processes [25, 32, 52, 84]. In this study, the PBE model (3.3) was solved numerically by approximating the integral expression using Simpson's Rule with 100 equally spaced node points. The resulting system of 100 nonlinear ordinary differential equations describing the time evolution of the volume percent distribution at each node point was solved using the Matlab integration code `ode45`. The measured distribution of the coarse pre-emulsion was used as the initial condition  $n_p(v, 0)$ .

### 3.2.3 Parameter Estimation

The constants  $K_1$ – $K_4$  in the breakage rate functions (3.7) and (3.8) were estimated from drop volume distribution measurements using a systematic nonlinear optimization procedure rather than an inefficient trial-and-error procedure. The data available for parameter estimation consisted of measured bulk emulsion properties ( $\phi$ ,  $\sigma$ ,  $\rho_d$ ,  $\eta_d$ ,  $\eta_c$ ) and drop

volume distribution measurements for the coarse pre-emulsion  $n(v, 0)$  and the processed emulsion obtained after the  $i$ th homogenizer pass  $n(v, i)$ . In addition to approximating the integral expression with Simpson's rule, the PBE model (3.3) was spatially and temporally discretized to produce a large set of nonlinear algebraic equations suitable for the application of constrained optimization codes. Spatial discretization in the volume space was performed using a finite difference approximation with 100 node points. Temporal discretization was performed using orthogonal collocation on finite elements where each pass corresponded to a single finite element and 2 internal collocation points were employed within each finite element. We found that additional spatial node points, finite elements, and/or collocation points had a negligible effect on the parameter estimates but increased the computational effort significantly.

The parameter estimation problem was posed as the constrained minimization of the following least-squares objective function,

$$\Psi = \sum_{i=1}^N \sum_{j=1}^n \frac{[\hat{n}_p(v_j, i) - n_p(v_j, i)]^2}{[n_p(v_j, i)]^2} \quad (3.9)$$

where  $n_p(v_j, i)$  is the measured value of the drop volume distribution at drop volume  $v_j$  and homogenizer pass  $i$ ,  $\hat{n}_p(v_j, i)$  is corresponding predicted value from the PBE model (3.3),  $n$  is the total number of spatial node points, and  $N$  is the number of passes. The objective function was minimized subject to a large number of equality constraints representing the discretized model equations and continuity conditions across the finite elements. The decision variables in optimization problem were the constants  $K_1$  and  $K_2$  if  $g(v) = g_1(v)$ , the constants  $K_3$  and  $K_4$  if  $g(v) = g_2(v)$ , or the four constants  $K_1-K_4$  if  $g(v) = g_1(v) + g_2(v)$ . The optimization problem was formulated in AMPL [29] and solved using the nonlinear program code CONOPT. For some cases, multiple data sets were used and the objective function  $\Psi$  included a third sum over the data sets. Relative values of the objective function were used to judge the quality of model predictions.

### **3.3 Results and Discussion**

#### **3.3.1 Homogenized Drop Volume Distributions**

We prepared 5 sample emulsions at the base case conditions (Table 3.1), performed 5 homogenization passes for each sample, and measured the drop volume distribution after each pass for each sample to analyze data reproducibility. The maximum standard deviation in the measured drop size distribution based on five repeats for any pass was about 9%, indicating that the experimental procedure and the distribution measurements were quite reproducible.

Figure 3.1(a) shows a representative set of drop distribution measurements for the base case conditions. The pre-emulsion produced a bimodal distribution with the two peaks exhibiting large differences in drop diameter. Successive homogenizer passes had the effect of reducing the volume percentage of large drops, increasing the percentage of small drops, and sharpening the two peaks. The peak diameter of larger drops was noticeably reduced with successive passes, while the peak diameter of smaller drops remained roughly constant. Each pass produced a smaller relative change in the distribution, indicating that the breakage rate decreased with decreasing drop size. Figures 3.1 (b–d) show optical microscopy images at 20x magnification of the pre-emulsion, the first pass, and the fifth pass, respectively. The images were consistent with the measured drop distributions, with subsequent passes producing a larger fraction of small drops and all three samples having a noticeable bimodal nature.

#### **3.3.2 Recoalescence Test**

The PBE model (3.3) used in this study is based on the assumption of negligible drop coalescence in the homogenizer. The term recoalescence is used to denote coalescence occurring in the homogenizer from newly formed drops. While the base case emulsion (Table 3.1) was formulated to have a low dispersed phase volume fraction and a high surfactant concentration to minimize recoalescence, we performed a targeted experiment to

test this assumption. A base case emulsion was prepared and successively homogenized for six passes at 10000 psig (68.95 MPa) until the Sauter mean diameter and drop distribution remained approximately constant, at which time the rates of drop breakage and drop coalescence (if present) were expected to be equal. The sample obtained after the sixth pass at 10000 psig was reprocessed with five additional passes at 5000 psig (34.47 MPa), which was expected to produce a reduced breakage rate and an increased coalescence rate if significant recoalescence was occurring. If the mean diameter and drop volume distribution remained approximately constant after successive passes at 5000 psig, then the coalescence rate was judged to be negligible relative to the breakage rate.

Figures 3.2(a) and 3.2(b) show the results of this experiment, with the six passes at 10000 psig (68.95 MPa) labeled H10K-1–H10K-6 and the five passes at 5000 psig labeled H5K-1–H5K-5. Convergence of the Sauter mean diameters and the drop distributions support the assumption of negligible coalescence at the base case condition. While this assumption was not validated for the other conditions studied, we were confident that the coalescence rate remained small. We also calculated the theoretical surface load from measured values of the interfacial tension versus surfactant concentration. The ratio of the adsorption to collision time scale [117] shown below provides a qualitative measure of the extent of recoalescence,

$$\frac{\tau_{ads}}{\tau_{coll}} = \frac{6\pi\Gamma\phi}{dC_s} \quad (3.10)$$

where  $\Gamma$  is the surface load and  $C_s$  is surfactant concentration. For negligible recoalescence, the ratio of  $\tau_{ads}/\tau_{coll}$  should be less than 1. At our base case conditions this ratio was in the range of 0.15 – 0.3, further indicating that recoalescence is negligible.

### 3.3.3 Computational Fluid Dynamics

Figure 3.3 shows CFD results for the homogenizing valve and the truncated section near the valve that constituted the domain for flow field calculations. Although not included in

our simple PBE model, the CFD calculations indicated strong spatial heterogeneities over the homogenizer domain. The contours demonstrated that the turbulence intensity was large in and at the exit of the valve gap and comparatively small elsewhere. Reynolds numbers in the range of 2000-4000 were calculated for most of the gap section, indicating the presence of a turbulent flow field. These results suggested that turbulence is an important mechanism for drop breakage in the gap region and provided a mechanistic basis to apply the breakage rate functions (3.7) and (3.8) to our system.

### 3.3.4 Base Case Parameter Estimation

We performed parameter estimation for the base case emulsion (Table 3.1) to better understand the relevant mechanisms for drop breakage. First parameter estimation was performed using the breakage rate function  $g_1(v)$  (3.7) derived under the assumption that breakage results from drop collision with turbulent eddies. Measured drop volume distributions for the pre-emulsion and for the five processed emulsions sampled after each pass were used to estimate the unknown constant  $K_1$  and  $K_2$ . Figure 3.4(a) shows the resulting dependence of  $g_1(v)$  on the drop diameter. The breakage function exhibited a maximum rate at a drop diameter of approximately  $5 \mu\text{m}$ , suggesting reduced breakage for very large drops, and small breakage rates below  $1 \mu\text{m}$ , indicating negligible breakage of small drops. The corresponding drop distribution predictions are shown in Figure 3.4(b) along with the objective function value  $\Psi$ . The parameterized PBE model generated poor predictions, with the peak for larger drops poorly tracked and the movement of the peak for smaller drops not captured whatsoever due to the negligible breakage rates predicted at small drop sizes. The decreasing breakage rate above  $5 \mu\text{m}$  appeared to have a relatively small effect on drop distribution predictions as the model emulsions had only a small number of such large drops.

Next parameter estimation was performed to determine the constants  $K_3$  and  $K_4$  of the breakage rate function  $g_2(v)$  (3.8) derived under the assumption that turbulent shear was

the primary mechanism for drop breakage. The results (Figure 3.5(a)–3.5(b)) were very similar to those obtained for the other breakage function. The optimizer determined that the objective function  $\Psi$  was minimized by placing the breakage rate peak at a relatively large drop diameter due to the greater contribution of the large drop region to  $\Psi$ . As a result, very little breakage of small drops was predicted and the experimentally observed movement of the smaller drop peak could not be tracked. These results demonstrated that neither of two breakage rate functions alone could capture experimentally observed trends and suggested that some relevant physics were not modeled.

Although the large deviations observed between experimental and predicted drop distributions could be attributed to other factors, we investigated the possibility that the two turbulent breakage mechanisms were simultaneously active. For this case, the breakage rate function  $g(v) = g_1(v) + g_2(v)$  and the four constants  $K_1$ – $K_4$  were estimated. We found that the optimizer could converge to two locally optimal solutions that produced identical  $\Psi$  values depending on the initial parameter guesses. Each solution produced a slightly bimodal breakage function, with the first peak for small drops corresponding to one function and the second peak for large drops corresponding to the other function. The solutions differed according to which function corresponded to which peak. Based on timescale arguments presented in Appendix B, we determined that the more physically meaningful solution was  $g_1(v)$  representing the first peak and  $g_2(v)$  representing the second peak (Figure 3.5(c)). The combined breakage function produced much closer agreement to the experimental data (Figure 3.5(d)) than either function alone, as reflected by the smaller  $\Psi$  value (0.202 versus 0.414 in Figure 3.4(b)). The movement of both peaks in the drop distribution was qualitatively captured, although noticeable differences between the measured and predicted distributions remained. We judged these base case modeling results to be acceptable.

### 3.3.5 PBE Model Extensibility

We sought to investigate the extensibility of the PBE model with the combined breakage rate function to conditions other than the base case. The dispersed phase volume fraction ( $\phi$ ), the interfacial tension ( $\sigma$ ), the continuous phase viscosity ( $\eta_c$ ), and the homogenizer pressure ( $P$ ) were varied from their base case values (Table 3.1) to determine if the  $K_1$ – $K_4$  values estimated from the base case data could produce satisfactory drop distribution predictions over a range of conditions. For each case, the four parameters were also re-estimated from a combined data set that included variations in the associated emulsion property or the homogenizer pressure to determine if improved predictions could be generated.

First we compared experimental and predicted values of the De Brouckere mean moment diameter  $d_{43}$  [68] to determine if the PBE model could capture the general trends observed experimentally. The mean diameter  $d_{43}$ , which is defined as the ratio of the fourth moment over the third moment of the drop distribution, provides a meaningful scalar measure of the mean diameter for the bimodal distributions observed in our data sets. To investigate the effect of the dispersed phase volume fraction ( $\phi$ ), the oil concentration was reduced by 50% ( $\phi = 2.78 \times 10^{-3}$ ) and increased by 200% ( $\phi = 0.0112$ ) and 400% ( $\phi = 0.0228$ ) from the base case value ( $\phi = 5.59 \times 10^{-3}$ ). The experimental (Figure 3.6(a)) and predicted (Figure 3.6(b)) results show good agreement, demonstrating that the model can capture trends in  $\phi$ . The effect of the interfacial tension ( $\sigma$ ) was examined by varying the surfactant concentration by 50% ( $\sigma = 14.32$  mN/m), 200% ( $\sigma = 13.06$  mN/m), and 300% ( $\sigma = 12.68$  mN/m) from the base case value ( $\sigma = 13.68$  mN/m). The model (Figure 3.6(d)) captured the decreasing mean diameter observed experimentally (Figure 3.6(c)) for increasing surfactant concentration.

The continuous phase viscosity ( $\eta_c$ ) was increased from its base value ( $\eta_c = 1$  cP) by adding varying amounts of sucrose to the water. While the model (Figure 3.7(b)) captured the decreasing mean diameter observed experimentally (Figure 3.7(a)) for increasing continuous phase viscosity, the results for the largest value ( $\eta_c = 1.3$  cP) were only qual-

itatively correct. The homogenizer pressure ( $P$ ) was varied over the range 5000–20000 Psi (34.47–137.9 MPa), with the nominal value being  $P = 10000$  Psi. The model (Figure 3.7(d)) reproduced the experimental trend (Figure 3.7(c)) that the mean diameter decreased with increasing pressure. However the predicted results show significant errors, especially for the lowest pressure ( $P = 5000$  Psi). Taken collectively, these results suggested that the functional dependencies of the combined breakage rate functions  $g(v)$  was reasonable but that quantitative predictions with the base case model parameters may be difficult. Below we further examine this issue by analyzing results for the full drop size distribution.

### **Dispersed phase volume fraction**

The base case dispersed phase volume fraction was reduced by half ( $\phi = 2.78 \times 10^{-3}$ ) and doubled ( $\phi = 0.0112$ ) by changing the oil concentration. Drop distributions predicted with the base case parameter values are compared to experimentally measured distributions in Figures 3.8(a) and 3.8(c). Also shown are objective function  $\Psi$  values calculated directly from (5.15). For the reduced  $\phi$  value, re-estimation of the  $K_1$ – $K_4$  parameters did not provide any improvement in prediction accuracy (Figure 3.8(b)). By contrast, re-estimation produced significant improvement for the increased  $\phi$  value (Figure 3.8(d)). We concluded that the functional dependence of the breakage rate on the dispersed phase volume fraction was reasonable, but that parameter estimation with data generated for varying  $\phi$  would be necessary to more accurately predict the effect of this formulation variable.

### **Interfacial tension**

The base case surfactant concentration was reduced by half and doubled, and the resulting changes in the interfacial tension  $\sigma$  were measured to be 14.32 mN/m and 13.06 mN/m, respectively. Comparison of predicted drop distributions obtained with the base case parameter values and experimentally measured distributions showed that the PBE model was better able to predict the effects of surfactant concentration increases (Figures 3.9(a) and 3.9(c)). Re-estimation of the  $K_1$ – $K_4$  parameters produced small decreases in the objective

function values at the expense of degraded distribution predictions at large drop diameters and eventual disappearance of model bimodality (Figures 3.9(b) and 3.9(d)). We concluded that the PBE model satisfactorily accounted for surfactant concentration changes, but that parameter estimation with data generated for varying  $\sigma$  may not improve predictive capability with respect to this formulation variable.

### **Continuous phase viscosity**

The continuous phase viscosity  $\eta_c$  was changed by adding varying amounts of sucrose to nanopure water used for emulsion preparation. Moderate and large additions of sucrose produced increased continuous phase viscosities of 1.09 cP and 1.195 cP, respectively, compared to the base case. The large sucrose addition also produced a slight change in interfacial tension, which was incorporated within the breakage rate function. Predicted drop distributions obtained with the base case parameter values are compared to experimentally measured distributions in Figures 3.10(a) and 3.10(c). As measured by relative objective function values, the PBE model predictions showed larger deviations from data than observed for  $\phi$  and  $\sigma$  variations. However, significantly improved predictions were obtained when the  $K_1$ – $K_4$  parameters were re-estimated (Figures 3.10(b) and 3.10(d)). We concluded that the functional dependence of the breakage rate on the continuous phase viscosity was reasonable, but that parameter estimation with data generated for varying  $\eta_c$  would be necessary to satisfactorily predict the effect of this formulation variable.

### **Multiple formulation variables**

Rational design of emulsified products will require models capable of predicting the coupled effects of multiple formulation variables. To this end, we performed additional experiments in which the dispersed phase volume fraction, interfacial tension, and continuous phase viscosity were changed simultaneously from their base case values. Predicted drop distributions obtained with the base case parameter values are compared to experimentally measured distributions for a representative case in Figure 3.11(a). The PBE model

captured most of the qualitative trends with the exception of the predicted distributions approaching unimodality more quickly than the measured distributions. Re-estimation of the  $K_1$ – $K_4$  parameters with a combined data set in which all the formulation variables were changed simultaneously produced a significant decrease in the objective function value (Figure 3.11(b)), but the predicted distributions become unimodal even more rapidly than with the base case parameters. We concluded that the PBE model was capable of capturing the coupled effects of multiple formulation variables given an appropriate data set for parameter estimation.

### **Homogenization pressure**

The homogenization pressure  $P$  was lowered to 5000 psig (34.47 MPa) and increased to 15000 psig (103.42 MPa) from the base case value. Comparison of predicted drop distributions obtained with the base case parameter values and experimentally measured distributions showed that the PBE model was not able to satisfactorily capture pressure variations (Figures 3.12(a) and 3.12(c)). Moreover, re-estimation of the  $K_1$ – $K_4$  parameters with a combined data set in which the pressure was varied did not substantially improve the model predictions (Figures 3.12(b) and 3.12(d)). These results suggest that the pressure dependence of the energy dissipation rate (3.6) was incorrect. However, additional parameter estimation tests in which the pressure exponent in (3.6) was considered to be another adjustable parameter did not significantly improve the model predictions (not shown).

We believe that our CFD study may provide insights into this model deficiency. The turbulence intensity contours in Figure 3.3 show strong spatial heterogeneities over the homogenizer domain, while the PBE model treats the homogenizer as a well-mixed system. Similar heterogeneities were observed in the pressure contours (not shown), with a large pressure drop from the valve gap inlet to the outlet. Accordingly, the assumption of a single homogenizer pressure is questionable and improved predictions over large pressure ranges may require the incorporation of spatial heterogeneities into the PBE model [63].

### **3.4 Conclusion**

We believe that the population balance equation (PBE) modeling approach presented in this chapter represents a necessary first step towards addressing the emulsion design problem for homogenized products. By invoking assumptions such as negligible drop coalescence, binary drop breakage and homogeneous flow fields in the homogenizer, we investigated the ability of a simplified PBE model to match experimental data. Drop breakage functions that depend explicitly on formulation and processing variables were used such that the PBE model has the potential to reproduce qualitative trends in the drop volume distribution that result when these variable are changed. Consequently, the model can be used to predict the effects of different formulation properties before performing the associated experiments. This capability will not only allow new formulations to be identified but also will enable unacceptable solutions to be eliminated more rapidly and with less experimental effort. The current version of our PBE model does not adequately describe the effects of the homogenization pressure. Our future work will focus on better capturing the pressure effect, relaxing the assumption of binary breakage, including mechanistic descriptions of drop coalescence, and combining predicted drop distributions with physical property estimation techniques to allow the prediction of end-use characteristics.

**Table 3.1.** Base case emulsion formulation and homogenization values

Soybean Oil	0.5 wt %
Pluronic F-68	0.1 wt%
Dispersed phase volume fraction ( $\phi$ )	$5.59 \times 10^{-3}$
Interfacial tension ( $\sigma$ )	13.68 mN/m
Continuous phase viscosity ( $\eta_c$ )	1 cP
Homogenizer pressure ( $P$ )	10000 psig (68.95 MPa)

**Table 3.2.** Range of emulsion formulations and homogenization pressures studied

Dispersed phase volume fraction ( $\phi$ )	$2.78 \times 10^{-3} - 0.0228$
Interfacial tension ( $\sigma$ )	14.318 – 12.68 mN/m
Continuous phase viscosity ( $\eta_c$ )	1 – 1.3 cP
Homogenizer pressure ( $P$ )	5000 – 20000 psig (34.48 – 137.9 MPa)

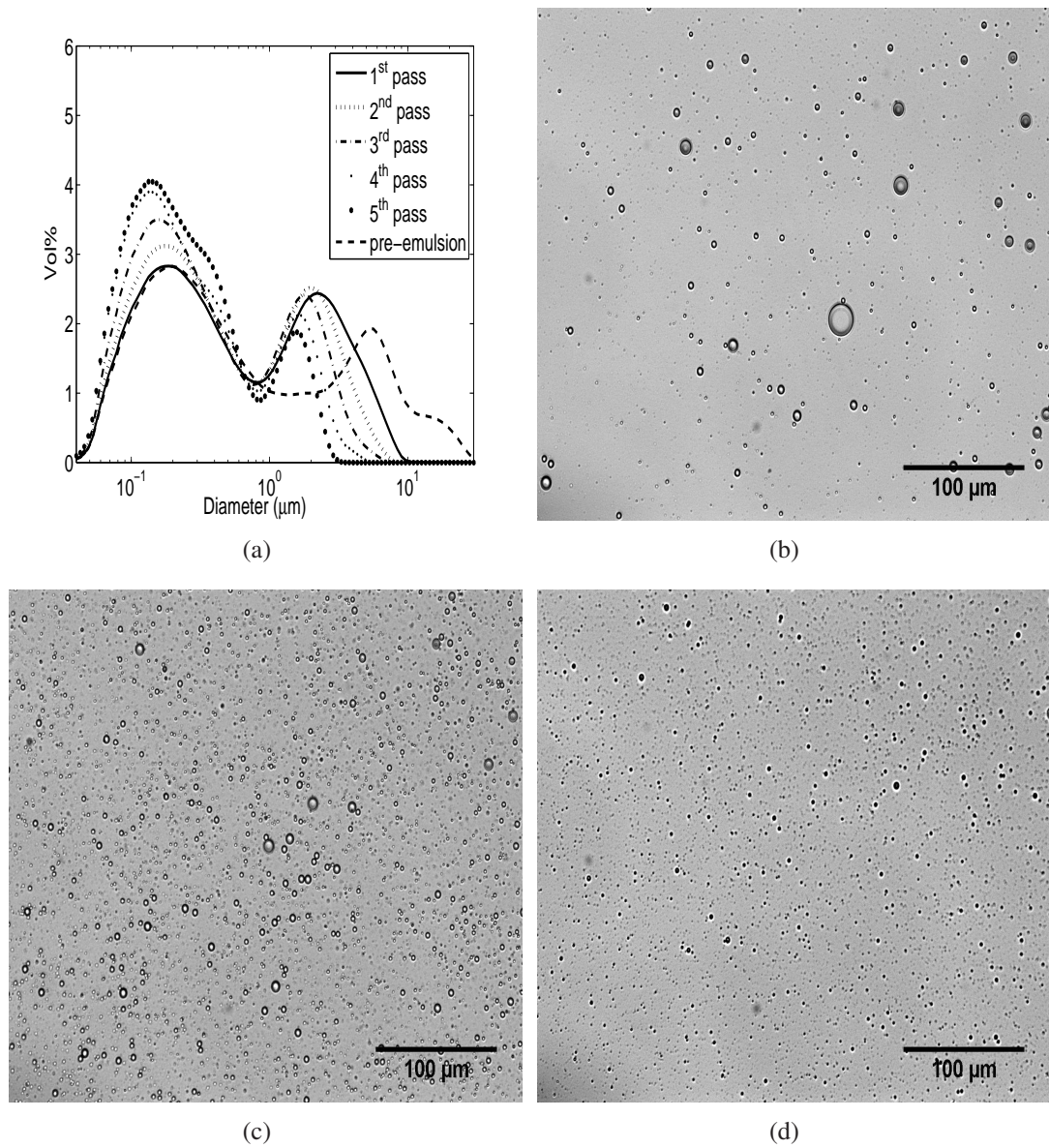
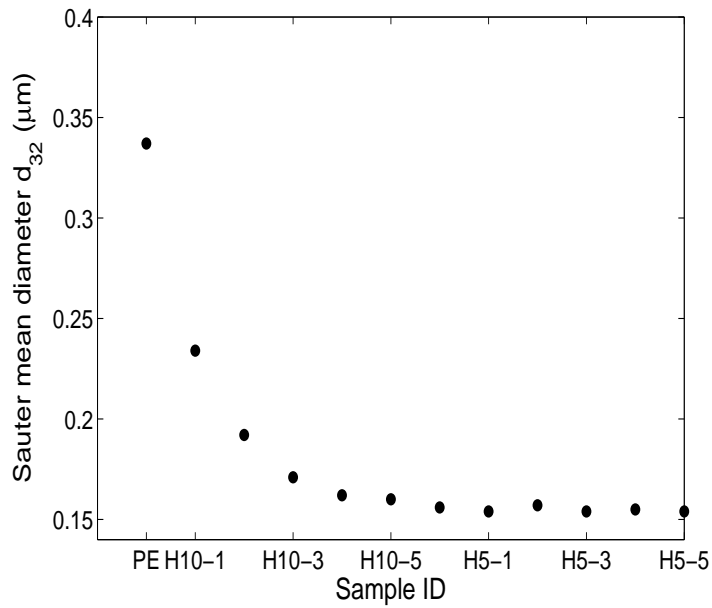
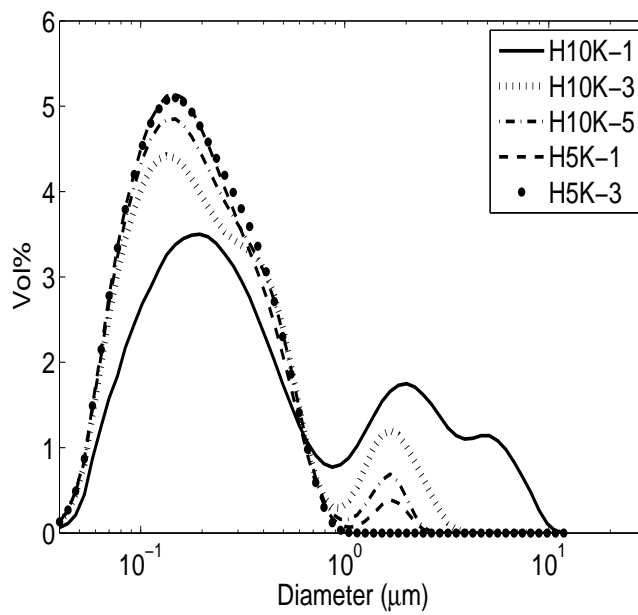


**Figure 3.1.** (a) Measured drop volume distributions for the base case conditions. Optical microscopy image at 20x magnification of (b) the pre-emulsion, (c) the homogenized sample after the first pass, and (d) the homogenized sample after the fifth pass.



(a)



(b)

**Figure 3.2.** Recoalescence test where the base case formulation was homogenized for six passes at 10000 psig (labeled H10K-1 through H10K-6) and then homogenized for five passes at 5000 psig (labeled as H5K-1 through H5K-5). (a) Sauter mean diameters  $d_{32}$ . (b) Drop volume distributions.

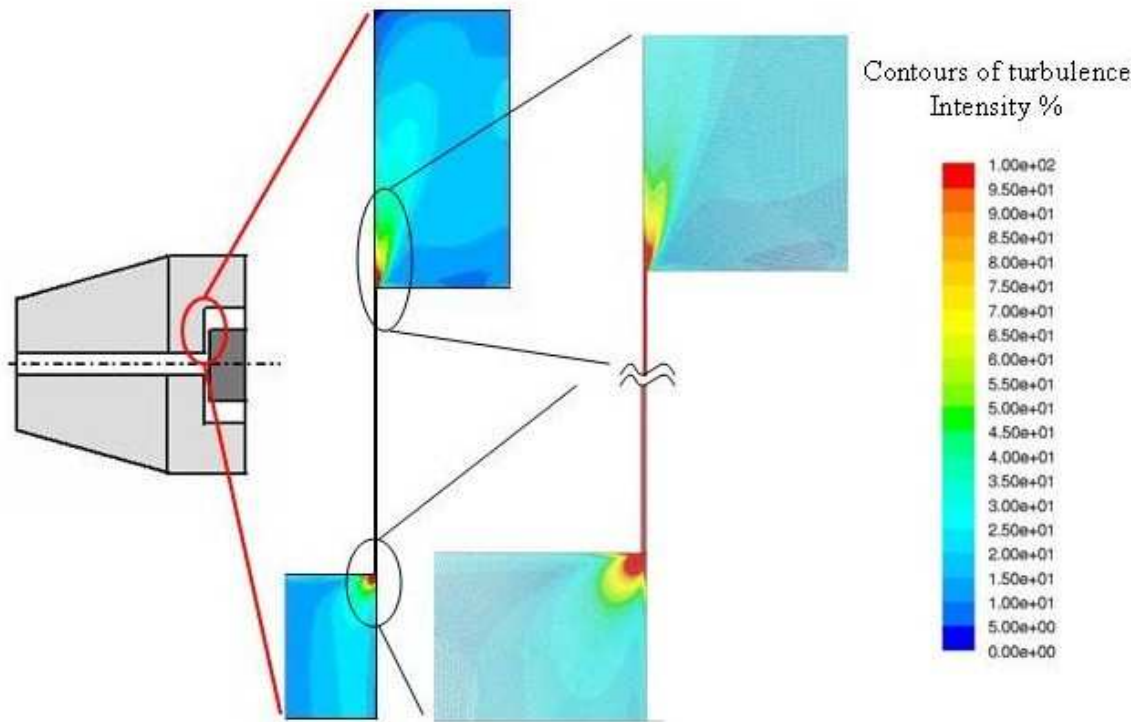


**Figure 3.3.** Computational fluid dynamics simulation of the homogenizing valve gap showing contours of turbulence intensity (%) near the valve. The section of the homogenizing valve is shown at the extreme left. The portion of the valve gap used for CFD calculation is shown in the center. Enlarged sections of the gap inlet, the middle part of the gap, and the gap outlet are shown on the right.

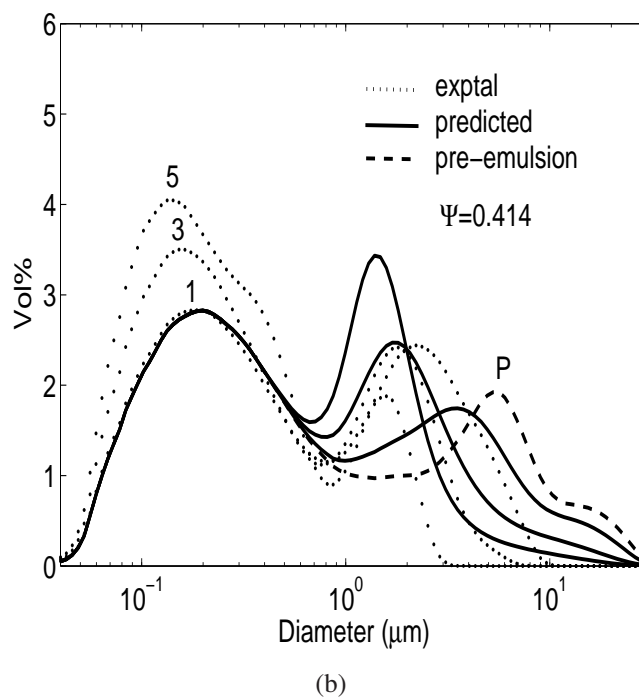
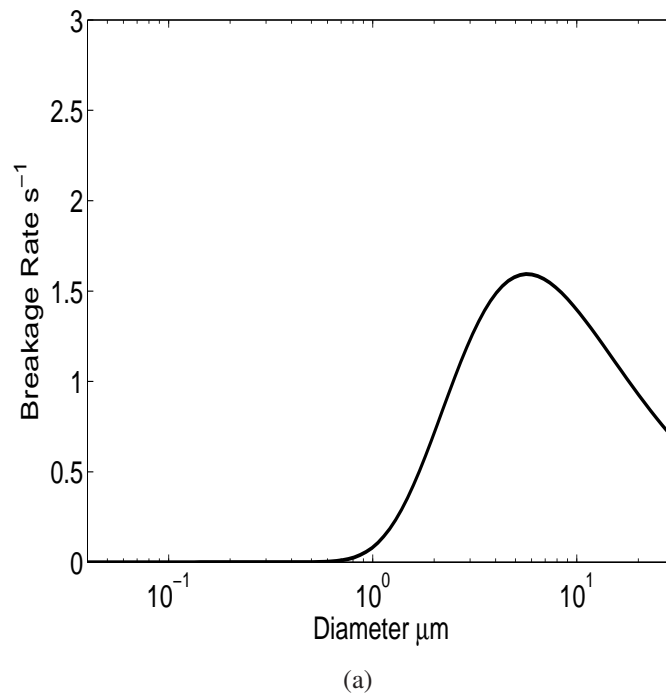


**Figure 3.4.** Base case parameter estimation results with the drop-eddy collision breakage function  $g_1(v)$ . (a) Breakage rate. (b) Predicted and experimental drop volume distributions for the pre-emulsion (P), the first pass (1), the third pass (3), and the fifth pass (5).  $\Psi$  is the objective function value.

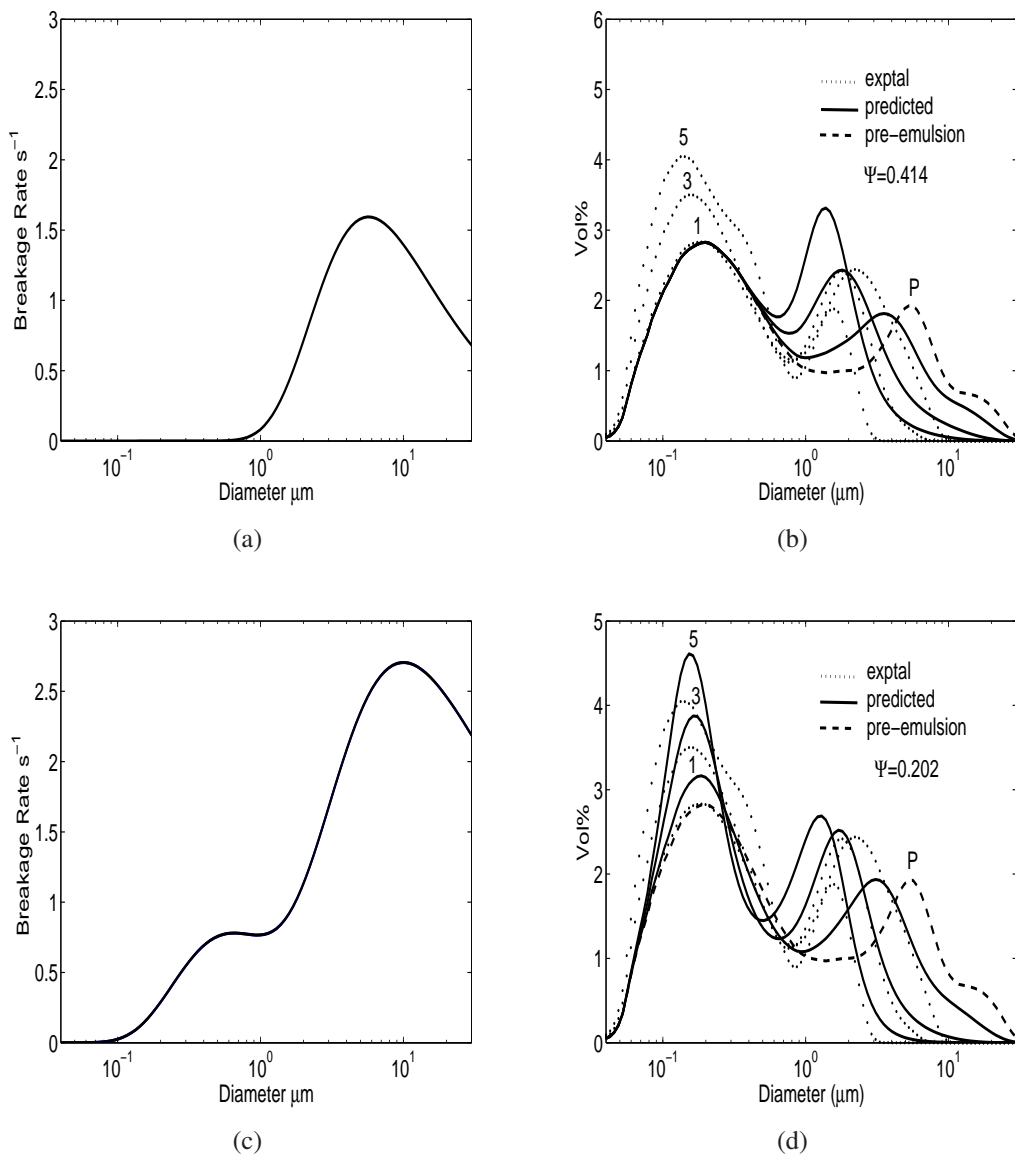
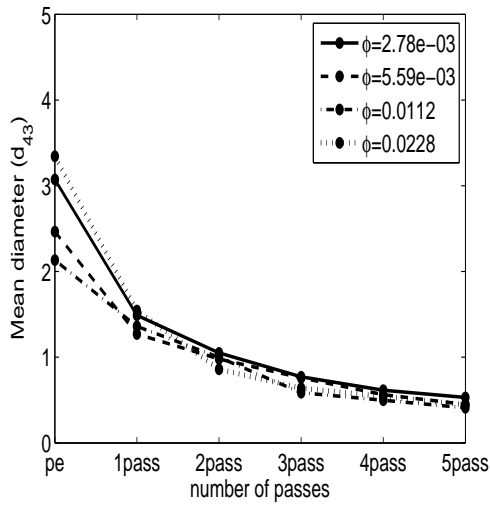
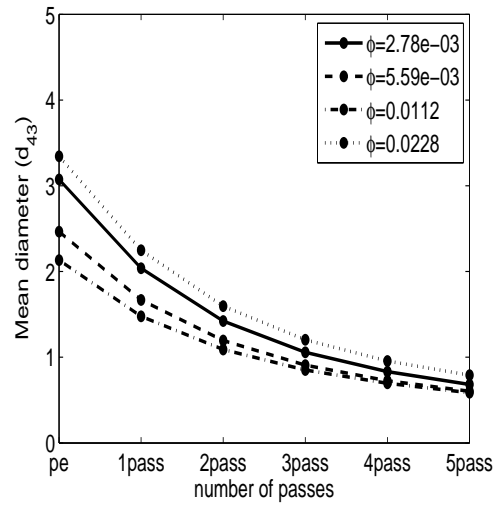


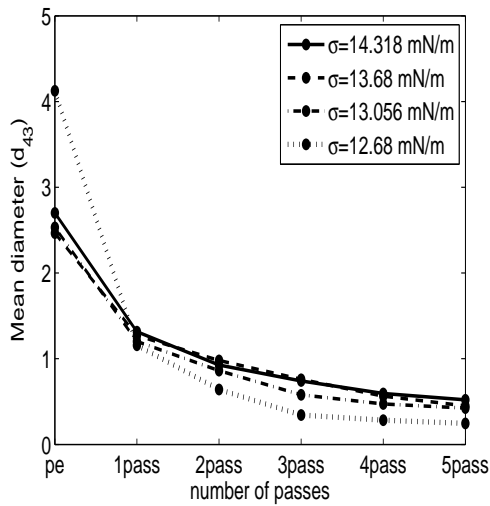
**Figure 3.5.** Base case parameter estimation results with the shear breakage function  $g_2(v)$ . (a) Breakage rate. (b) Predicted and experimental drop volume distributions. Base case parameter estimation results with the combined breakage function  $g(v) = g_1(v) + g_2(v)$ . (c) Breakage rate. (d) Predicted and experimental drop volume distributions.



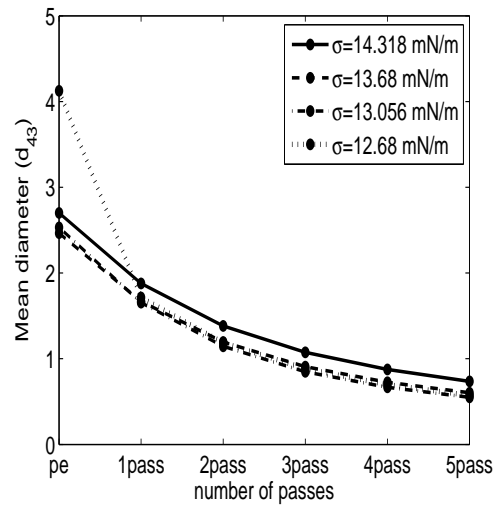
(a)



(b)



(c)



(d)

**Figure 3.6.** Effect of dispersed phase volume fraction and interfacial tension on the experimental and predicted mean diameters. a) Experimental mean diameters  $d_{43}$  for changes in dispersed phase volume fraction. b) Predicted mean diameters  $d_{43}$  using base case values for changes in dispersed phase volume fraction. c) Experimental mean diameters  $d_{43}$  for changes in interfacial tension. d) Predicted mean diameters  $d_{43}$  using base case values for changes in interfacial tension.

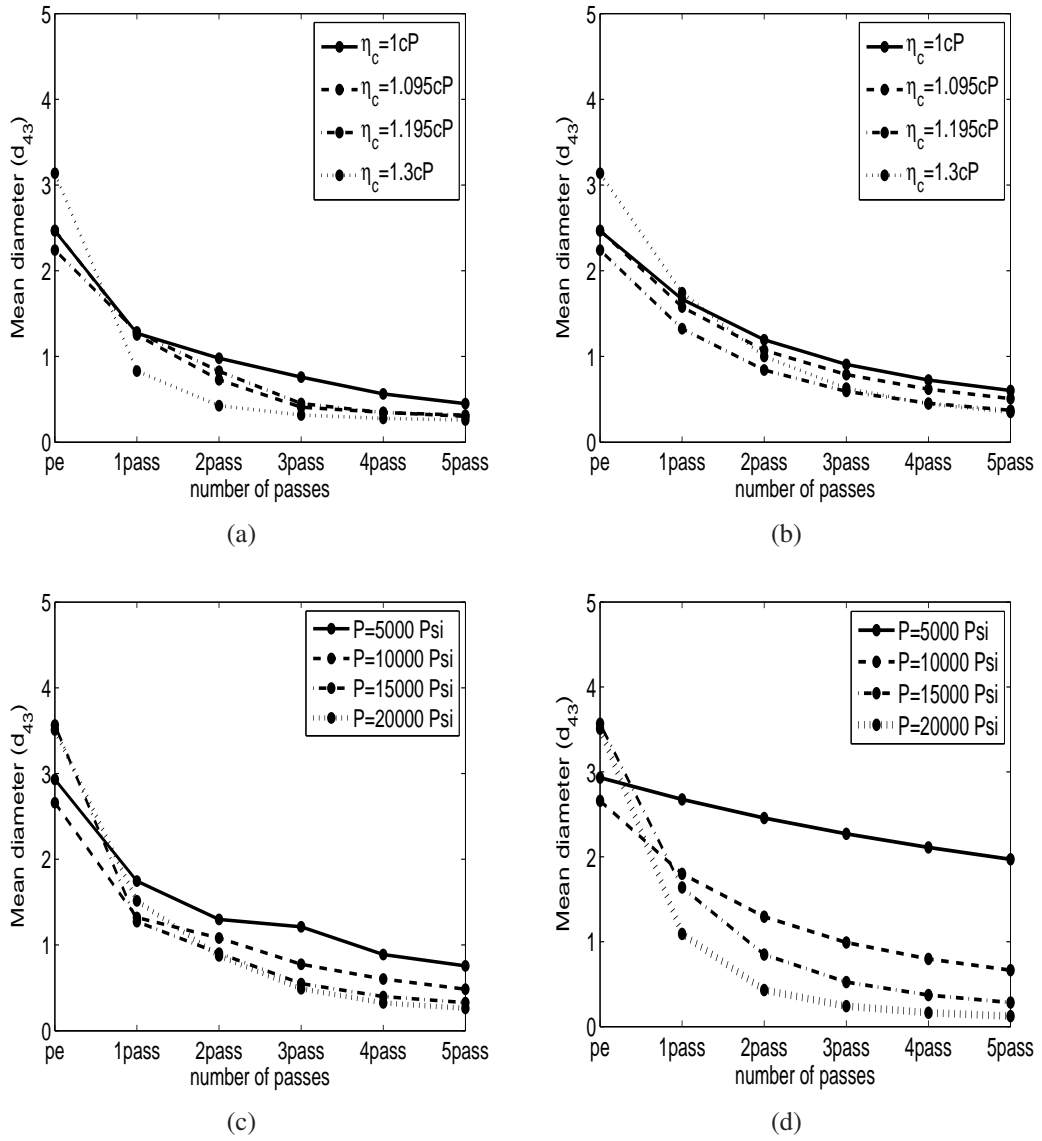


**Figure 3.7.** Effect of continuous phase viscosity and pressure on the experimental and predicted mean diameters. a) Experimental mean diameters  $d_{43}$  for changes in continuous phase viscosity. b) Predicted mean diameters  $d_{43}$  using base case values for changes in continuous phase viscosity. c) Experimental mean diameters  $d_{43}$  for changes in pressure. d) Predicted mean diameters  $d_{43}$  using base case values for changes in pressure.

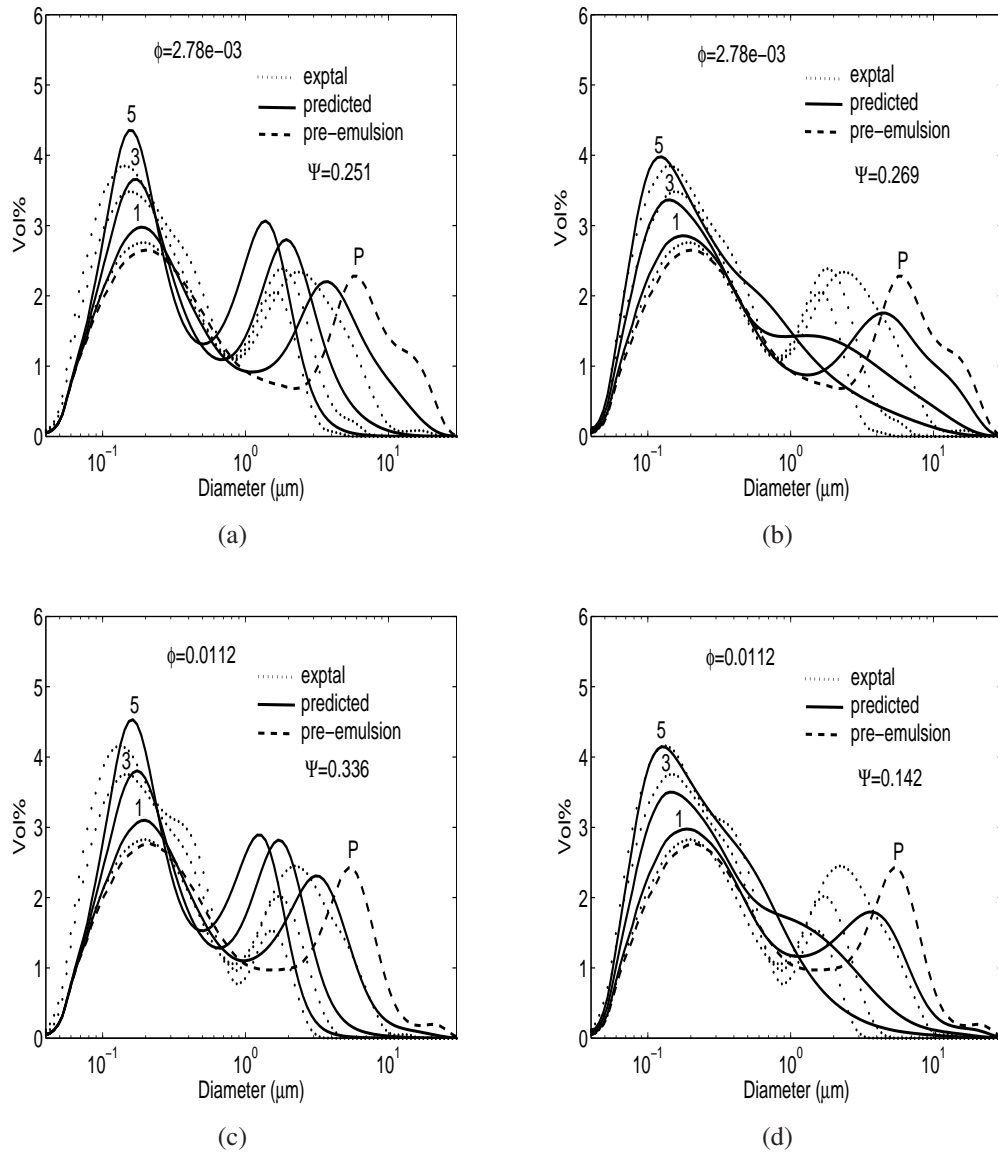


**Figure 3.8.** Effect of the dispersed phase volume fraction on predicted drop volume distributions with the combined breakage function  $g(v)$  for the pre-emulsion (P), the first pass (1), the third pass (3), and the fifth pass (5).  $\Psi$  is the objective function value. The base case values were used for the adjustable breakage parameters  $K_1-K_4$ . (a)  $\phi = 2.78 \times 10^{-3}$ . (c)  $\phi = 0.0112$ . The parameters  $K_1-K_4$  were re-estimated using a combined data set containing the dispersed phase volume fraction variations. (b)  $\phi = 2.78 \times 10^{-3}$ . (d)  $\phi = 0.0112$ .

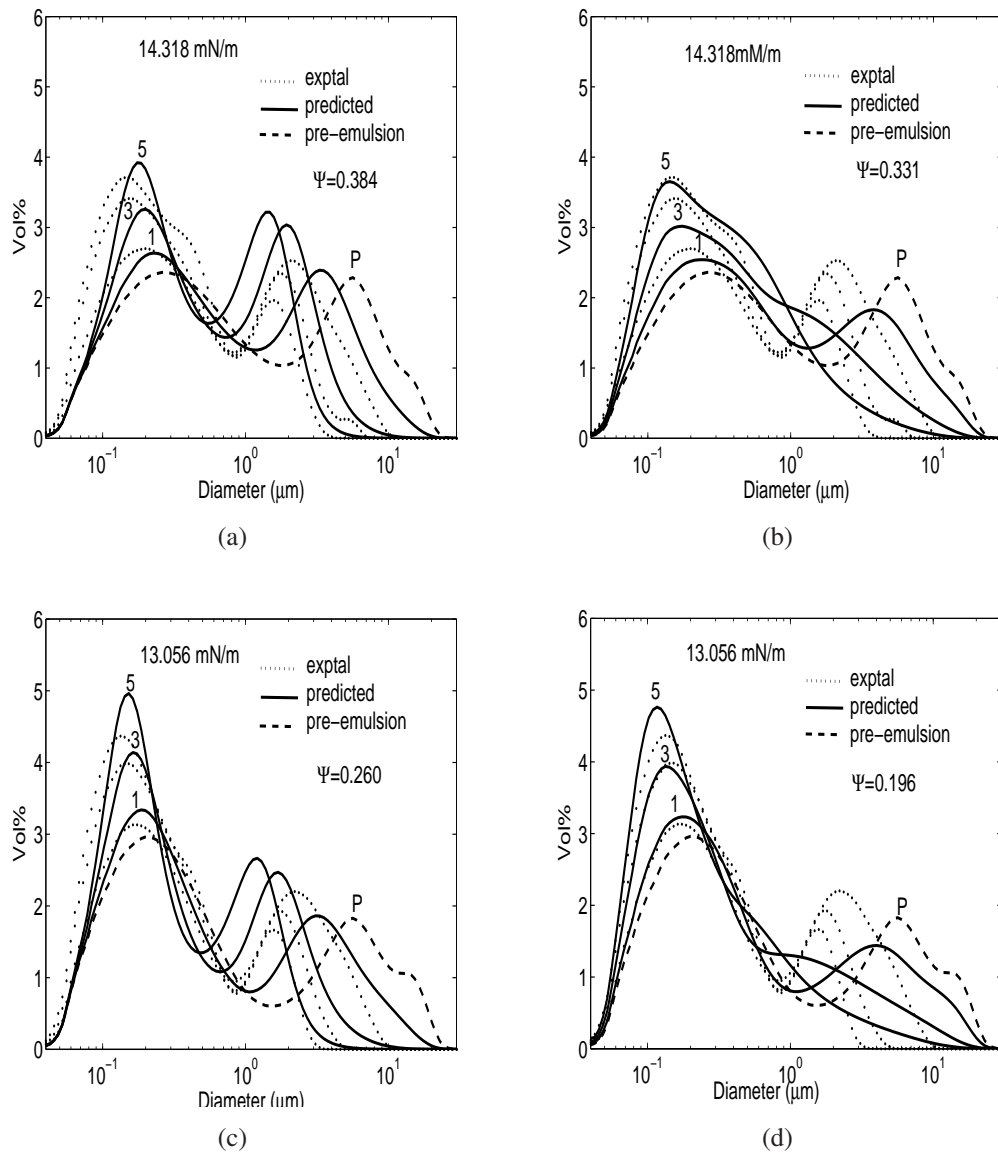


**Figure 3.9.** Effect of the interfacial tension on predicted drop volume distributions with the combined breakage function  $g(v)$ . The base case values were used for the adjustable breakage parameters  $K_1-K_4$ . (a)  $\sigma = 14.318$  mN/m. (c)  $\sigma = 13.056$  mN/m. The parameters  $K_1-K_4$  were re-estimated using a combined data set containing the interfacial tension variations. (b)  $\sigma = 14.318$  mN/m. (d)  $\sigma = 13.056$ .

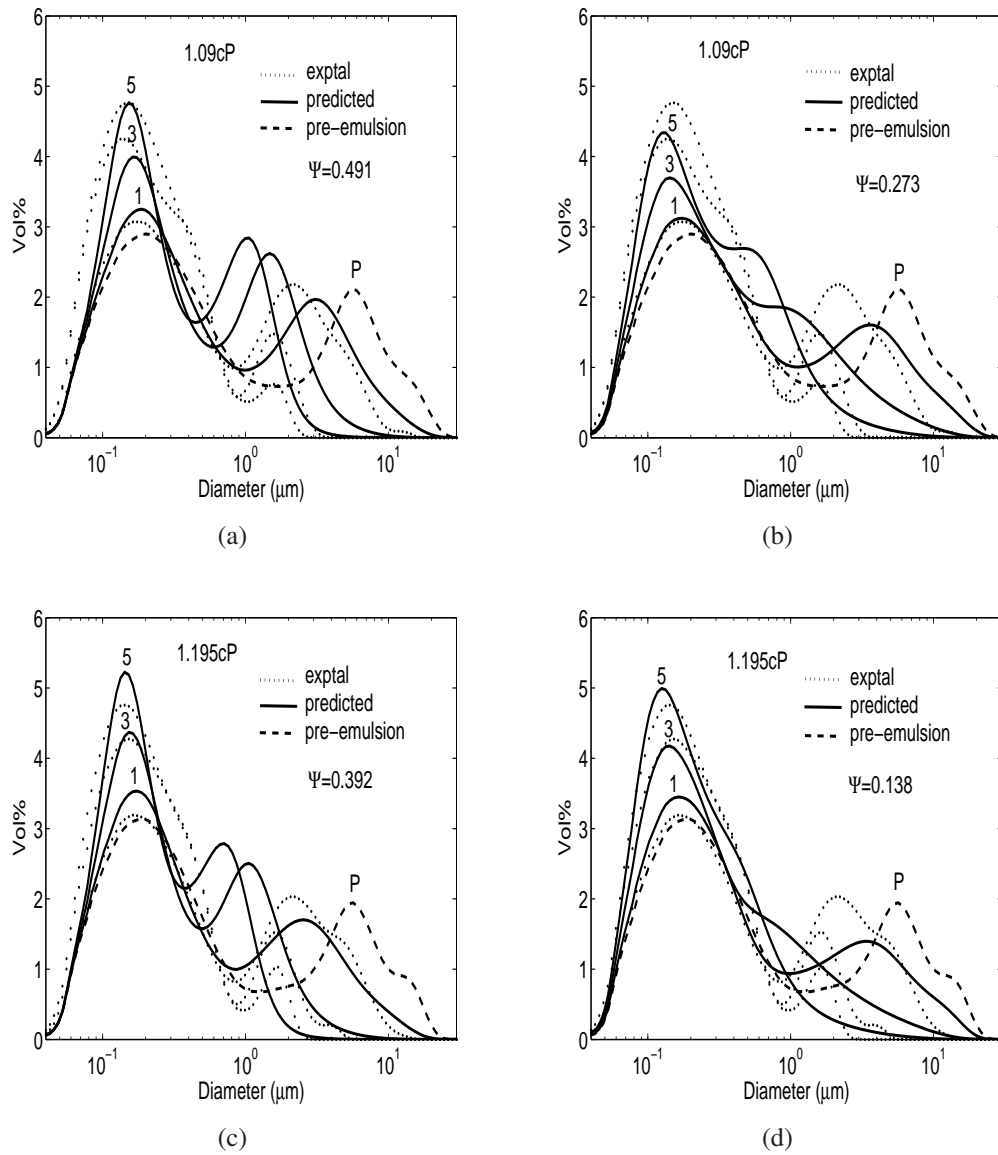
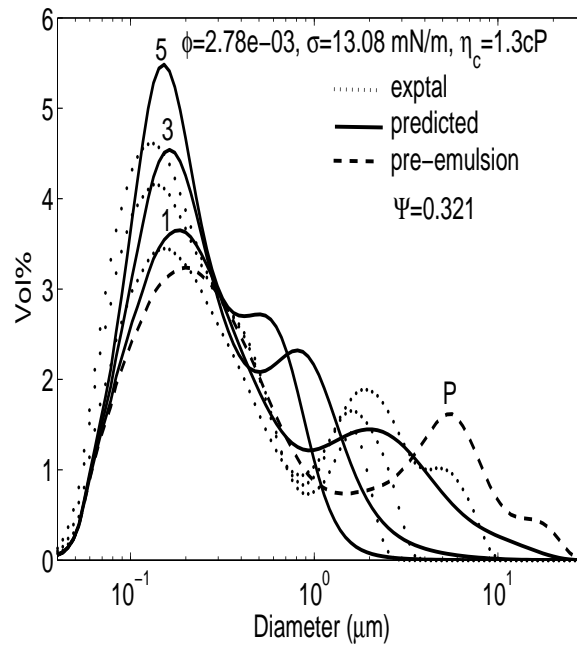
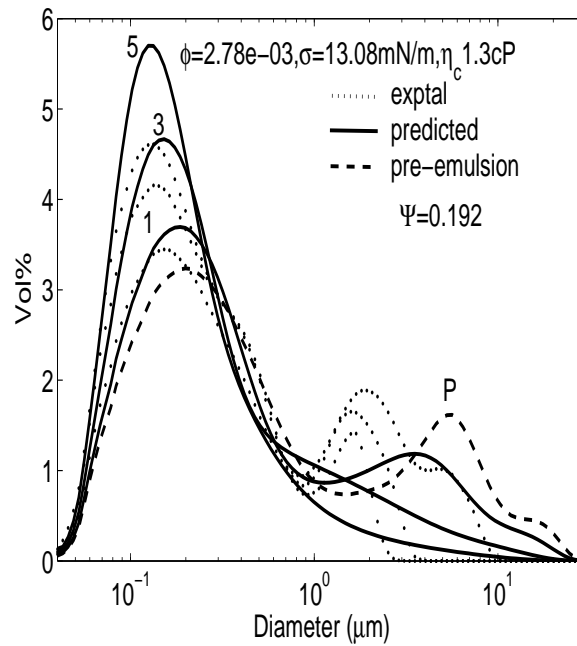


**Figure 3.10.** Effect of the continuous phase viscosity on predicted drop volume distributions with the combined breakage function  $g(v)$ . The base case values were used for the adjustable breakage parameters  $K_1-K_4$ . (a)  $\eta_c = 1.09$  cP. (c)  $\eta_c = 1.195$  cP. The parameters  $K_1-K_4$  were re-estimated using a combined data set containing the continuous phase viscosity variations. (b)  $\eta_c = 1.09$  cP. (d)  $\eta_c = 1.195$  cP.



(a)



(b)

**Figure 3.11.** Effect of simultaneous changes in the dispersed phase volume fraction, interfacial tension, and continuous phase viscosity with the combined breakage function  $g(v)$ . (a) The base case values were used for the adjustable breakage parameters  $K_1-K_4$ . (b) The parameters  $K_1-K_4$  were re-estimated using a combined data set containing variations in the three formulation variables.

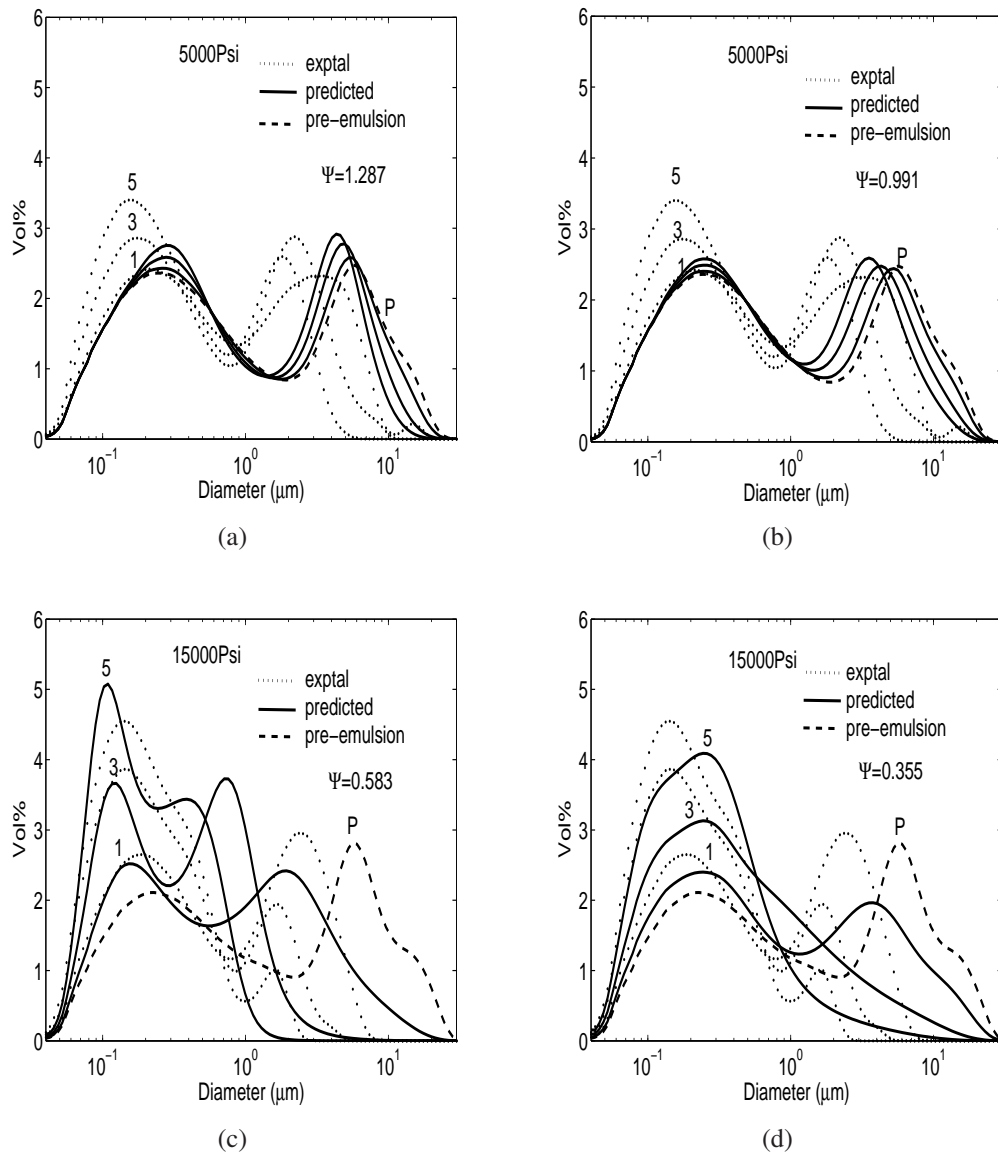


**Figure 3.12.** Effect of the homogenization pressure on predicted drop volume distributions with the combined breakage function  $g(v)$ . The base case values were used for the adjustable breakage parameters  $K_1-K_4$ . (a)  $P = 5000$  psig (34.47 MPa). (c)  $P = 15000$  psig (103.42 MPa). The parameters  $K_1-K_4$  were re-estimated using a combined data set containing the pressure variations. (b)  $P = 5000$  psig (34.47 MPa). (d)  $P = 15000$  psig (103.42 MPa).

## CHAPTER 4

### PREDICTION OF EMULSION DROP SIZE DISTRIBUTIONS WITH POPULATION BALANCE EQUATION MODELS OF MULTIPLE DROP BREAKAGE

In this chapter, we develop a PBE model with multiple drop breakage and evaluate model predictions for an oil-in-water emulsion processed in a pilot-scale homogenizer. Two distinct rate functions [81], one for drop breakage due to turbulent eddies and another for turbulent shear are used to reproduce the observed bimodal distributions. Multiple drop breakage is modeled using the generalized Hill-Ng distribution [24, 40, 125] and determining the assumed number  $p$  of daughter drops formed that provides the best agreement with measured drop size distributions. The PBE model with multiple drop breakage is compared to the analogous binary breakage PBE model when adjustable model parameters are determined by nonlinear optimization. The multiple breakage PBE model is evaluated for different emulsion formulations by using the base case model parameters to predict the effects of oil concentration, surfactant concentration, oil to surfactant ratio and emulsion premix distribution on predicted drop size distributions.

#### 4.1 Experimental Methods

##### 4.1.1 Materials

Oil-in-water emulsions were prepared using sunflower oil (Albert Heijn brand) as the dispersed phase, water as the continuous phase, and the non-ionic surfactant Pluronic F-68 (Sigma) as the emulsifier. The base case emulsion consisted of 5wt% oil and 0.1wt% surfactant with the remainder water as listed in Table 4.1. Experiments were performed at

the base case conditions and at other concentrations different from the base case conditions. Additional oil and/or surfactant were added to the base case amounts to obtain the desired concentrations.

#### **4.1.2 Emulsion Preparation**

All the experiments were performed at the Unilever Food & Health Research Institute, Vlaardingen, Netherlands with a pilot plant scale homogenizer. Emulsions were prepared using a two-step process. First a coarse pre-emulsion was prepared by mixing the chemical ingredients in a stirred tank device (Silverson L4RT). For most of the experiments, the mixing speed and time used were 5000 rpm and 3 minutes, respectively (Table 4.1). For testing the effect of the premix on homogenized drop size distributions, two other speeds (5000 and 7500 rpm) and three other mixing times (1,3 and 5 minutes) were used. About 2 liters of premix was prepared, of which approximately 100 ml were sampled for measuring the premix drop size distribution (see below). The premix was then processed in a two-stage, high-pressure homogenizer (APV Gaulin, Niro Soavi). For all the reported experiments, only a single stage was used and the pressure was fixed at 650 bars. Multiple passes were performed by reprocessing the emulsion obtained from the previous homogenizer pass. All the passes had about the same processing time and the time between passes was limited to less than a minute. Three passes were performed for most of the experiments, and after each pass about 100 ml of the emulsion was sampled for drop size distribution measurement. A set of experiments was also performed at zero pressure applied on the homogenizer.

Emulsion compositions for the different cases studied are listed in Tables (4.2-4.4). For most of the emulsions tested, identical premixes were prepared at the base composition, mixer speed and stirring time (Table 4.1). To vary the oil concentration, premixes at 5wt% oil were diluted and additional surfactant was added to reach the desired composition as listed in Table 4.2. The premixes were then homogenized at 650 bar for 3 passes, and the drop size distribution was measured after each pass. To increase the surfactant concentra-

tion, additional surfactant was added to the premix to reach the desired concentration while the reduced concentration case of 0.05wt% surfactant was prepared separately (Table 4.3). For the third set of tests, the oil and surfactant concentrations were varied such that the ratio of oil to surfactant was kept constant at 5 (Table 4.4). The effect of the premix was investigated using the base case formulation and changing the mixing properties. Six different premixes were prepared by varying the mixing speed (5000 and 7500 rpm) and stirring times (1,3, and 5 minutes) were used. All these premixes were homogenized at 650 bar for 3 passes.

### **4.1.3 Emulsion Characterization**

Drop size distributions were measured using a Malvern Mastersizer 2000 particle size analyzer. Oil-water interfacial tensions were measured by drop shape analysis using Tracker, automatic drop tensiometer (IT Concept, Teclis) at 25°C. Optical microscopy was performed on some of the premix and homogenized samples using a Zeiss Axioplan-2 microscope. Sample densities were measured using Bio-Rad 36XMX densitometer and viscosities were measured using a TA Ar-2000 stress controlled rheometer (Texas Instruments).

## **4.2 Theory**

### **4.2.1 Population Balance Equation Model**

We assumed that the high pressure homogenizer was a pure breakage process and utilized the population balance equation (PBE) model developed in our previous work [81] to predict evolution of the drop size distribution. The assumption of negligible coalescence is reasonable when the dispersed phase volume fraction is small and excess surfactant is present, conditions which generally held for the experiments performed. Experiments for which this assumption may have been violated were also performed to identify possible areas of improvement for the model.

Under the breakage only assumption, the PBE for a batch system was written as [16, 18, 19],

$$\frac{\partial n(v, t)}{\partial t} = -g(v)n(v, t) + \int_v^\infty \beta(v, v')\nu(v')g(v')n(v', t)dv' \quad (4.1)$$

where:  $n(v, t)dv$  is the number of drops with volume in the range  $[v, v + dv]$  per unit volume of the dispersion;  $g(v)$  is the breakage rate representing the fraction of drops of volume  $v$  breaking per unit time;  $\nu(v)$  is the number of daughter drops formed by breakage of a mother drop of volume  $v$ ; and  $\beta(v, v')$  is the daughter drop distribution function representing the probability of forming a daughter drop of size  $v$  from breakage of a mother drop of size  $v'$ . As in our previous work [81], we modeled the high-pressure homogenizer as a well-mixed batch system in which the initial drop volume distribution was the measured distribution of the premix and each pass corresponded to one dimensionless time unit. Since the particle size analyzer provided measurements of the volume percent distribution  $n_p(v, t)$ , we reformulated the PBE model in terms of volume percent distribution as follows,

$$\frac{\partial n_p(v, t)}{\partial t} = -g(v)n_p(v, t) + v \int_0^\infty \frac{g(v')\nu(v')\beta(v, v')n_p(v', t)}{v'}dv' \quad (4.2)$$

The PBE model (4.2) required specification of three functions: the breakage rate  $g(v)$ , the daughter drop distribution  $\beta(v, v')$  and the number of daughter drops formed  $\nu(v)$ . Following our previous work [81], the breakage rate was assumed to be determined by turbulent breakage of drops by both inertial and viscous forces. The first breakage function  $g_1(v)$  was a modified version of two previously proposed functions [18, 19], which were derived assuming that breakage results from drop collision with turbulent eddies, extended to high-pressure homogenizers,

$$g_1(v) = K_1 v^{-1/3} P^{1/2} \rho_d^{-1/2} \exp \left[ -\frac{K_2 \sigma (1 + \phi)^2}{v^{1/3} P} \right] \quad (4.3)$$

where  $K_1$  and  $K_2$  are adjustable constants. The second breakage rate function  $g_2(v)$  was derived under the assumption that drop breakage results from turbulent shear [81],

$$g_2(v) = K_3 \left( \frac{2}{\pi} \right)^{1/2} \left( \frac{P^{3/4}}{\eta_d^{1/2} \rho_d^{1/4} v^{1/6}} \right) \exp \left( \frac{-2K_4 \sigma^2 \lambda}{\eta_c P^{3/2} \rho_d^{-1/2} v^{1/3}} \right) \quad (4.4)$$

where  $K_3$  and  $K_4$  are adjustable constants. The total breakage rate was assumed to be the sum of the two individual rates,

$$g(v) = g_1(v) + g_2(v) \quad (4.5)$$

One objective of this study was to determine if the dependence of the breakage rate function  $g(v)$  on emulsion parameters ( $\phi$ ,  $\sigma$ ,  $\rho_d$ ,  $\eta_d$ ) and the homogenization pressure ( $P$ ) was sufficient to allow prediction of chemical and process variations on the drop size distribution. Our experiments revealed that substantial drop breakage occurred even with no applied pressure on the homogenizer. Since  $g_1(v)$  and  $g_2(v)$  are pressure dependent functions that account for turbulent drop breakage, we derived (see Appendix C) a new breakage function that described drop breakage due to laminar shear applicable under low homogenization pressures,

$$g_3(v) = K_5 \left( \frac{2}{\pi} \right)^{1/2} Q \exp \left[ - \left( K_6 \frac{2Ca_c \sigma \pi^{1/3}}{\eta_c Q (6v)^{1/3}} \right)^2 \right] \quad (4.6)$$

For consistency with our previous work, we first considered binary breakage ( $\nu(v)=2$ ) and used the truncated normal distribution as the daughter drop distribution function ( $\beta(v, v')$ ) such that breakage had the highest probability of forming two equally sized daughter drops [63, 92, 101],

$$\beta(v, v') = \frac{2.4}{v'} \exp \left[ -4.5 \frac{(2v - v')^2}{(v')^2} \right] \quad (4.7)$$

Motivated by laminar flow experiments showing multiple daughter drops can be formed from a single mother drop [82, 105, 126] as well as other emulsion modeling studies [7, 49,

109, 115], we also considered the possibility of multiple daughter drop formation. For this purpose, we used the power law product form of the generalized Hill-Ng distribution [24, 40, 125],

$$\beta(v, v') = \frac{p}{\mathbf{B}(q, r)} \left(\frac{v}{v'}\right)^{q-1} \left(1 - \frac{v}{v'}\right)^{r-1}, \quad r = q(p-1) \quad (4.8)$$

This equation represents the generalized beta distribution function where  $p \geq 2$  is the number of daughter drops formed,  $q > 0$  determines the shape of the distribution and  $\mathbf{B}(q, r)$  is the beta function. To utilize equation 4.8, the parameter  $p$  must be specified *a priori*. When  $q = 1$ , equation 4.8 reduces to the uniform distribution for  $p$  daughter drops,

$$\beta(v, v') = p(p-1) \left(1 - \frac{v}{v'}\right)^{p-2} \quad (4.9)$$

The effect of the two parameters of the distribution function on the drop size distribution predictions is discussed in detail in the results section

The PBE model was solved numerically by spatially discretizing the integro-differential equation (4.2) with a fixed pivot method [52] with 100 node points over the volume domain of interest. The resulting system of 100 nonlinear ordinary differential equations describing the time evolution of the volume percent distribution at each node point was solved using the Matlab integration code `ode45`. The measured distribution of the coarse premix was used as the initial condition  $n_p(v, 0)$ , and the distribution after the  $i^{th}$  homogenizer pass was  $n_p(v, i)$ .

#### 4.2.2 Parameter Estimation

The constants  $K_1-K_4$  in the turbulent breakage rate functions (equations 4.3 and 4.4) were treated as adjustable parameters to be estimated from homogenization experiments. Available experimental data for parameter estimation included emulsion ingredient properties ( $\phi, \sigma, \rho_d, \eta_d, \eta_c$ ) that are measured *a priori* and drop size distributions for the premix  $n_p(v, 0)$  and the processed emulsion obtained after the  $i^{th}$  homogenizer pass  $n_p(v, i)$ .

The PBE model (equation 4.2) was spatially discretized by finite differences with 100 node points. The resulting set of nonlinear ordinary differential equations was reduced to a large system of nonlinear algebraic equations suitable for incorporation into nonlinear optimization codes through temporal discretization with orthogonal collocation on finite elements. For this purpose, we used Radau collocation where each pass corresponded to 2 finite element and 2 internal collocation points were employed within each finite element. We determined that these numbers of node points, finite elements and collocation provided an acceptable compromise between solution accuracy and computational efficiency. The parameter estimation problem was posed as a constrained minimization problem with the following objective function and equality constraints corresponding to the discretized model equations and continuity conditions across the finite elements,

$$\Psi = \sum_{i=1}^N \sum_{j=1}^n \frac{[\hat{n}_p(v_j, i) - n_p(v_j, i)]^2}{[n_p(v_j, i)]^2} \quad (4.10)$$

where  $n_p(v_j, i)$  is the measured drop size distribution corresponding to drop volume  $v_j$  and the  $i^{th}$  homogenizer pass,  $\hat{n}_p(v_j, i)$  is corresponding predicted value from the PBE model,  $n$  is the total number of node points, and  $N$  is the number of passes. The optimization problem was formulated in AMPL [29] and solved using the nonlinear solver CONOPT.

### Extent of Recoalescence

Recoalescence is an important phenomenon that can occur if there is insufficient surfactant to stabilize drops resulting from breakage [28]. The ratio of the adsorption to collision time scales [117] shown below can be used as a qualitative measure of the extent of recoalescence,

$$\frac{\tau_{ads}}{\tau_{coll}} = \frac{6\pi\Gamma\phi}{dC_s} \quad (4.11)$$

where  $\Gamma$  is the surface load and  $C_s$  is the surfactant concentration. Recoalescence was assumed to be negligible when  $\tau_{ads}/\tau_{coll} \ll 1$ , which is favored under conditions of low

oil concentration and high surfactant concentration. The surface load  $\Gamma$  was calculated by balancing the amount of added surfactant and the surfactant adsorbed at the interface. Other parameters in equation 4.11 were calculated from the emulsion composition and the Sauter mean diameter  $d_{32}$  as described elsewhere [117].

## 4.3 Results and Discussion

### 4.3.1 Reproducibility of Measured Drop Volume Distributions

To test the reproducibility of measured drop volume distributions, we performed 5 homogenization experiments at the base case conditions (Table 4.1). The data set for each experiment included the measured drop volume distributions of the premix and the processed emulsions obtained after the first, second and third homogenization passes. The mean and the standard deviation of the measured distributions in each bin were calculated individually for each pass from the 5 data sets (Figure 4.1a). The maximum standard deviation for any bin was 0.41, 0.53 and 0.58 for passes 1, 2, and 3, respectively, indicating that the experimental procedure and the distribution measurements were very reproducible. The measured distributions were used to calculate the mean and standard deviation of Sauter mean diameters ( $d_{32}$ ) for the premix and each pass (4.1b). In addition to exhibiting good reproducibility, the  $d_{32}$  values show that most size reduction occurred during the first pass and very little breakage was observed during the third pass.

### 4.3.2 Base Case Parameter Estimation

Using measured drop size distributions obtained for the base case homogenization conditions (Table 4.1), we attempted to estimate the breakage rate parameters  $K_1$ - $K_4$  (equations 4.3 and 4.4) with the measured distribution for the premix used as the initial condition in the PBE model (equation 4.2). First we performed parameter estimation assuming binary breakage and using the truncated normal distribution function (equation 4.7) to model the daughter drop distribution. While accurate model predictions were obtained when the distri-

bution data was fit for individual passes (Figures 4.2(a), 4.2(b) and 4.2(d)), poor predictions were generated when all the distribution data were fit simultaneously (Figures 4.2(c) and 4.2(d)). Both the individual pass distributions and the Sauter mean diameters were poorly predicted in the latter case due to underprediction of breakage during the first two passes and overprediction during the third pass.

Next we performed parameter estimation assuming multiple daughter drop formation using the uniform version of the generalized power law product function (equation 4.9) to model the daughter drop distribution. The number of daughter drops formed from a single drop was assumed to be  $p=20$ . The effect of the two adjustable parameters  $q$  and  $p$  on predicted drop size distributions are examined in detail below. In addition to accurately fitting individual pass data (Figures 4.3(a) and 4.3(b)), the multiple drop breakage model was able to yield substantially improved predictions when all the distribution data were fit simultaneously (Figures 4.3(c) and 4.3(d)) compared to the binary breakage model (Figures 4.2(c) and 4.2(d)). The objective function value, which is the error measure we have used, obtained with multiple breakage ( $\Psi=0.35$ ) was much smaller than the value obtained with binary breakage ( $\Psi=1.25$ ). Based on these results, we concluded that multiple drop formation was a likely breakage outcome as observed experimentally [82, 105, 126] and did not consider binary breakage further.

We varied the adjustable parameters  $q$  and  $p$  in the generalized Hill-Ng distribution (equation 4.8) in an effort to identify suitable values without resorting to mixed-integer nonlinear optimization. The  $q$  value was found to have a minimal effect on the objective function (Figure 4.4(b)), while increasing  $p$  values were shown to monotonically decrease the objective function (Figure 4.4(a)). Based on these results, we chose  $q=1$  corresponding to the simplest case of a uniform daughter drop distribution. Because the objective function was shown to asymptote at large  $p$  values and experimental studies [82, 105, 126] suggest that drop breakage into a very large number of daughter drops is unlikely, we used  $p=20$  for all future simulations.

### 4.3.3 Model Extensibility to New Emulsification Conditions

Because the third homogenizer pass produced the final emulsion product, we focused our subsequent analysis on prediction of the drop size distribution and Sauter mean diameter for the third pass only. The PBE model with multiple drop breakage ( $p=20$ ,  $q=1$ ) was used to generate estimates of the breakage rate parameters  $K_1$ – $K_4$  using the measured initial and third pass drop size distributions obtained for the base case conditions (Table 4.1). The constants were fixed at these optimal values and the PBE model was used to generate predictions for different oil concentrations, surfactant concentrations and premix distributions by changing the associated model variables as explained below for each case.

#### Oil concentration

To vary the oil concentration, premixes at 5wt% oil were diluted as necessary and additional surfactant was added to reach the desired compositions listed in Table 4.2. The premixes were then homogenized at 650 bar for 3 passes, and the drop size distribution was measured after each pass. Increasing oil concentrations shifted the drop size distribution (Figure 4.5(a)) and the Sauter mean diameter  $d_{32}$  (Figure 4.5(c)) towards larger drop diameters. The drop size distributions obtained at 0.5wt% and 1wt% oil were similar, while much larger differences were observed at higher oil concentrations. Simulated variations in the oil concentration were implemented by changing the dispersed volume fraction  $\phi$  in the breakage rate function (equation 4.3). Although the model also predicted a shift of the drop size distribution (Figure 4.5(b)) and Sauter mean diameter  $d_{32}$  (Figure 4.5(c)) towards larger drops with increasing oil concentrations, the model generated much smaller changes than observed experimentally. We believe that this difference was partially attributable to surfactant limitations present at higher oil concentrations, as the model did not account for coalescence due to partial drop coverage by available surfactant. Because the multiple drop breakage model produced marginally improved predictions as compared to the binary

breakage model for this parameter (Figure 4.5(d)) and the parameters discussed below, the binary breakage model is not discussed further in this chapter.

### **Surfactant concentration**

The impact of varying the surfactant concentration was investigated indirectly by varying the interfacial tension in the PBE model. The interfacial tension at the oil-water interface decreases as the concentration of surfactant in the system increases, which facilitates droplet disruption. The interfacial tension for a given surfactant concentration was measured using drop tensiometer. To vary the surfactant concentration, additional surfactant was added to the premix at 5wt% oil to reach the desired concentration while the smallest concentration of 0.05wt% surfactant was prepared separately (Table 4.3). Increasing surfactant concentrations shifted the drop size distribution (Figure 4.6(a)) and Sauter mean diameter (Figure 4.6(c)) towards smaller drop diameters and produced a noticeable sharpening of the drop size distribution. Simulated variations in the oil concentration were implemented by changing the interfacial tension  $\sigma$  in both breakage rate functions (equations 4.3 and 4.4). The model produced qualitatively correct predictions, as increasing surfactant concentrations shifted the drop size distribution (Figure 4.6(b)) and Sauter mean diameter (Figure 4.6(c)) towards smaller drop diameters. Although the model failed to capture the distribution sharpening behavior observed experimentally, the effects of variable surfactant concentration were predicted more accurately than those of variable oil concentrations. We believe that this difference was attributable to limited drop recoalescence occurring at high surfactant concentrations.

### **Constant oil to surfactant ratio**

The oil and surfactant concentrations were varied to maintain a constant oil to surfactant ratio of 5 (Table 4.4). While the drop size distributions showed less variability than when the oil and surfactant concentrations were varied individually, higher oil concentrations shifted the drop size distribution (Figure 4.7(a)) and Sauter mean diameter (Figure

4.7(c)) towards smaller drop diameters. Simulated variations in the oil and surfactant concentration were implemented by changing the dispersed volume fraction  $\phi$  and the interfacial tension  $\sigma$ , respectively, in both breakage rate functions (equations 4.3 and 4.4). The model produced qualitatively similar results, with the dominant effect of increasing surfactant concentrations shifting the drop size distribution (Figure 4.7(b)) and Sauter mean diameter (Figure 4.7(c)) towards smaller drop diameters. However, the model produced broader distributions and failed to capture the distribution sharpening behavior observed experimentally.

The previous results were generated using the breakage rate constants estimated for the base case conditions. We assembled a data set for variable oil to surfactant ratios and re-estimated the breakage parameters from this data to determine if improved drop size distribution predictions could be obtained. Results for 4 of the 6 ratios used show that re-estimation produced improved predictions compared to predictions obtained with the base case parameters (Figure 4.8). However, model predictions continued to deviate from experimental data at the higher oil to surfactant ratios. We hypothesize that this behavior might be partially attributable to reduced drop recoalescence occurring at high surfactant concentrations.

### **Recoalescence**

We calculated the ratio of the adsorption to collision time scales  $\tau_{ads}/\tau_{coll}$  (equation 4.11) for the various experiments performed to obtain a qualitative measure of the extent of recoalescence. The  $\tau_{ads}/\tau_{coll}$  ratio increased as the oil concentration increased (Figure 4.9(a)) or the surfactant concentration decreased (Figure 4.9(b)), producing conditions that favored recoalescence. The ratio was never sufficiently small ( $\tau_{ads}/\tau_{coll} \ll 1$ ) in these experiments to rule out the possibility of recoalescence and a corresponding shift of the size distribution towards larger drops. This analysis provides a possible explanation for the inability of the model fit at the base case conditions to predict drop size distributions at

other oil and surfactant concentrations. Homogenization at the base case conditions likely involved significant recoalescence while the model used in this study only accounted for drop breakage. As a result, parameter estimation produced a model in which the effects of drop breakage and recoalescence were lumped into the breakage functions and the model was not capable of producing accurate distribution predictions at other conditions for which the balance of drop breakage and recoalescence differed from the base case conditions (Figures 4.5 and 4.6). By contrast the  $\tau_{ads}/\tau_{coll}$  ratio remained approximately constant when the oil to surfactant ratio was held constant (Figure 4.9(c)), conditions under which the model produced more accurate drop size distribution predictions (Figure 4.7) than when the ratio was varied. Parameter re-estimation tests (Figure 4.8) also suggested the presence of drop recoalescence at large oil to surfactant ratios, as re-estimation only produced significantly improved predictions when the oil to surfactant ratio was relatively small. When  $\tau_{ads}/\tau_{coll}$  was plotted as a function of the oil to surfactant ratio for all the experiments performed, a monotonically increasing curve was produced (Figure 4.9(d)). This result suggested that the oil to surfactant ratio determined the size distribution by balancing the extent of surfactant adsorption at the drop interface and the frequency of drop collisions.

### **Premix drop size distribution**

Six premixes prepared by varying the mixing speed and mixing time of the stirred tank device produced a range of drop size distributions (Figure 4.10(a)). However the third pass homogenized samples obtained from these premixes were characterized by nearly identical size distributions (Figure 4.10(b)), suggesting that drop breakage was dominated by surfactant or energy limitations of the homogenizer rather than by the initial distribution. The model was able to capture this behavior very faithfully, predicting nearly identical third pass size distributions for all six premixes (Figure 4.10(c)). A plot of Sauter mean diameters for all six premixes showed that experimental third pass values were largely independent of the premix despite large difference in premix mean diameters (Figure 4.10(d)). A similar re-

sult was obtained for simulated first pass size distributions, suggesting that nearly constant size distributions were obtained after a single homogenization pass. The model with binary breakage did not produce good agreement with the experimental data as very different third pass distributions were predicted for the six premixes (not shown).

### **Zero applied pressure**

To investigate the role of homogenizer geometry on drop breakage, we performed experiments in which the premix prepared at the base case conditions was passed through the homogenizer without applying any external pressure on the homogenizing valve. Even under these laminar flow conditions, a significant amount of breakage was observed during the first pass (Figure 4.11(a)) and additional breakage occurred during the third pass (Figure 4.11(b)). We developed a pressure independent breakage rate function  $g_3$  (equation 4.6) applicable to laminar flow conditions to account for these observations. When the adjustable constants  $K_5$  and  $K_6$  were estimated from the individual pass distributions, the predicted distributions were quite accurate (Figures 4.11(a) and 4.11(b)). However, the predictions were degraded significantly when measured distributions for all three passes were used simultaneously for parameter estimation (Figure 4.11(c)). In this case, the fitted breakage function (Figure 4.11(d)) was not able to accurately predict over the wide range of drop sizes encountered. Additional studies are necessary to assess the usefulness of the proposed function.

## **4.4 Conclusions**

We developed a population balance equation (PBE) model that described the breakage of oil-in-water emulsion drops into a prespecified number of daughter drops according to a uniform distribution. Following our previous work, two distinct rate functions for drop breakage due to turbulent eddies and turbulent shear were used to reproduce the bimodal nature of measured drop size distributions from a pilot-scale high-pressure homogenizer.

Nonlinear optimization was used to find optimal values of four adjustable parameters in the breakage rate functions that minimized the least-squares difference between measured and predicted drop size distributions. If the number of daughter drops produced was chosen to be sufficiently large, the PBE model with multiple drop breakage produced more accurate predictions of measured size distributions than an analogous model based on the usual assumption of binary drop breakage. Using optimal parameter values for the base case conditions, the multiple breakage PBE model was shown to produce qualitatively correct predictions for different emulsion conditions obtained by varying the oil concentration, surfactant concentration, oil to surfactant ratio and emulsion premix distribution. More accurate predictions were obtained when the oil to surfactant ratio was relatively small, as unmodeled effects of drop recoalescence were minimized. An analysis of surfactant adsorption and drop collision time scales indicated that the oil to surfactant ratio strongly affected the obtained drop sizes and that recoalescence was not clearly negligible under any of the conditions studied in this chapter. The model was able to reproduce the experimental observation that homogenized drop size distributions were largely independent of the premix drop distribution. Experiments revealed that substantial breakage of the premix occurred during the first homogenization pass even under zero applied pressure operation. We proposed a new pressure independent breakage rate function and showed that the PBE model based on this function was able to partially reproduce experimentally observed behavior.

**Table 4.1.** Base case emulsion formulation and homogenization values

Sunflower Oil	5 wt %
Pluronic F-68 Surfactant	0.1 wt%
Interfacial tension ( $\sigma$ )	18.68 mN/m
Continuous phase viscosity ( $\eta_c$ )	1 cP
Premix speed and time	5000 rpm, 3 minutes
Homogenizer pressure ( $P$ )	650 bar

**Table 4.2.** Variable oil concentrations

Oil concentration (wt%)	Surfactant concentration (wt%)
0.5	0.1 wt%
1	0.1 wt%
2	0.1 wt%
5	0.1 wt%

**Table 4.3.** Variable surfactant concentrations

Oil concentration (wt%)	Surfactant concentration (wt%)
5	0.05 wt%
5	0.1 wt%
5	0.2 wt%
5	0.3 wt%
5	0.5 wt%
5	1.0 wt%

**Table 4.4.** Concentrations used to maintain constant oil to surfactant ratio

Oil concentration (wt%)	Surfactant concentration (wt%)
0.5	0.1 wt%
1	0.2 wt%
2	0.4 wt%
5	1.0 wt%

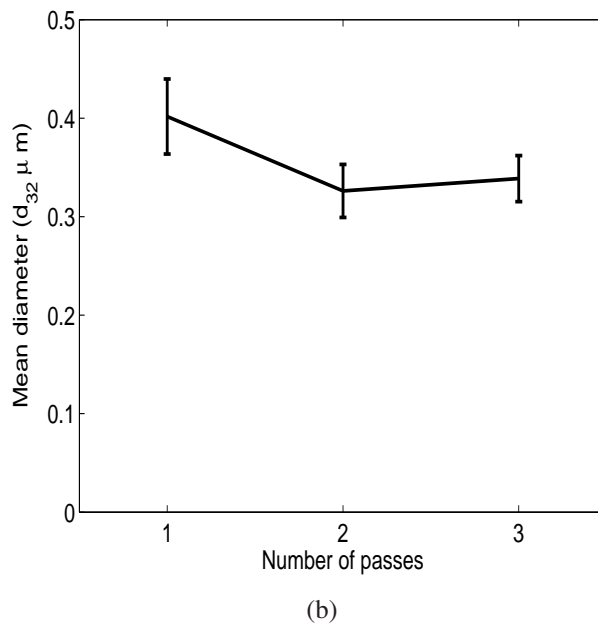
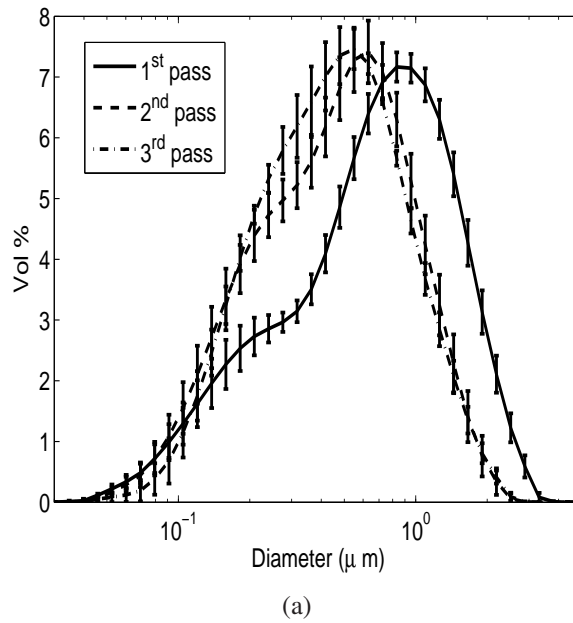


**Figure 4.1.** Experimental variability calculated from 5 repeats of the base case emulsification procedure. (a) Average drop size distributions and standard deviations for the first three homogenization passes. (b) Average Sauter mean diameters  $d_{32}$  and standard deviations for the premix and the first three homogenization passes.

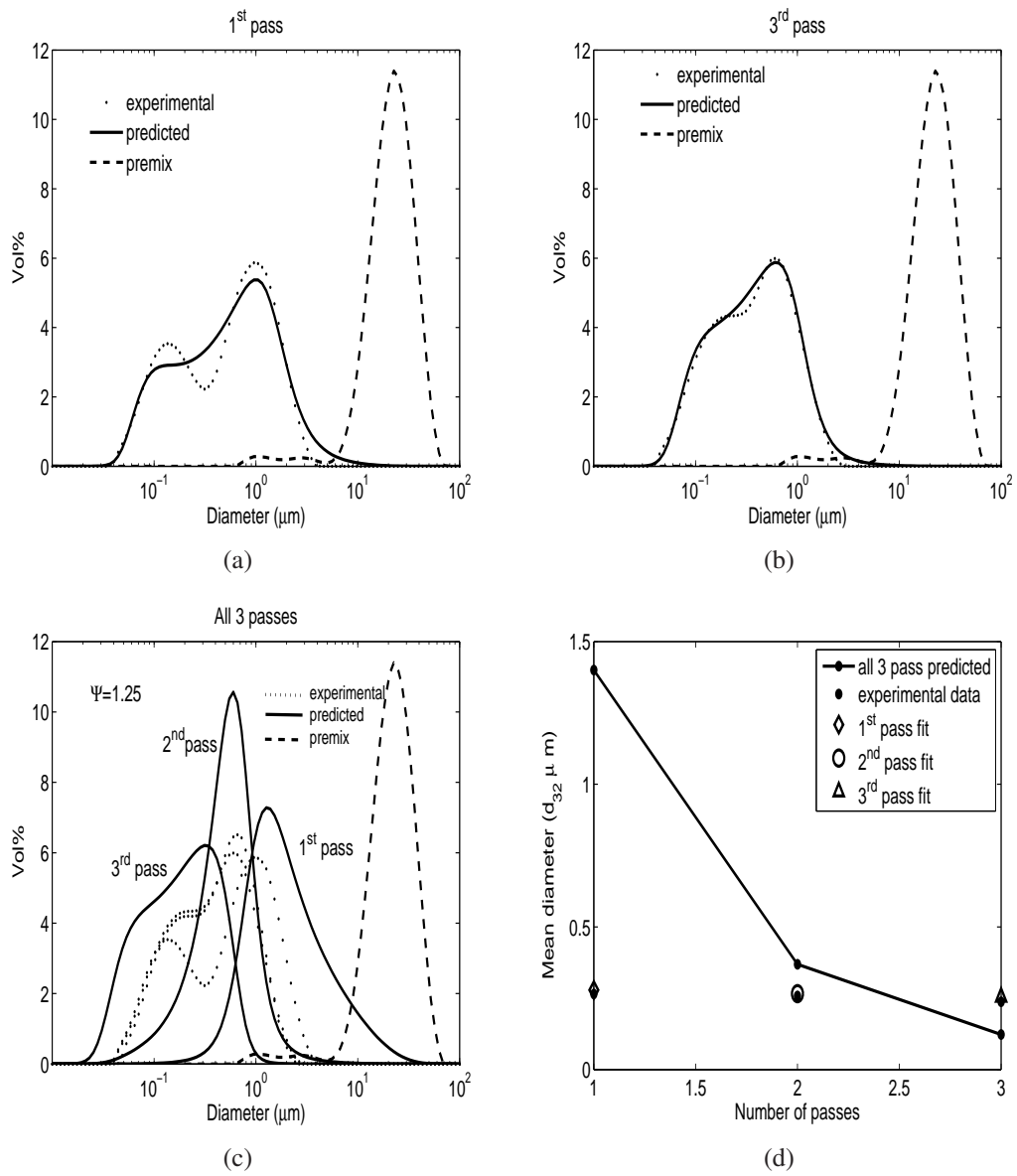


**Figure 4.2.** Drop size distribution predictions assuming binary breakage (equation (4.7)). (a) Predicted first pass drop size distribution. (b) Predicted third pass drop size distributions (c) Prediction drop size distributions for all 3 passes. (d) Experimental and predicted Sauter mean diameters  $d_{32}$  for all three passes.

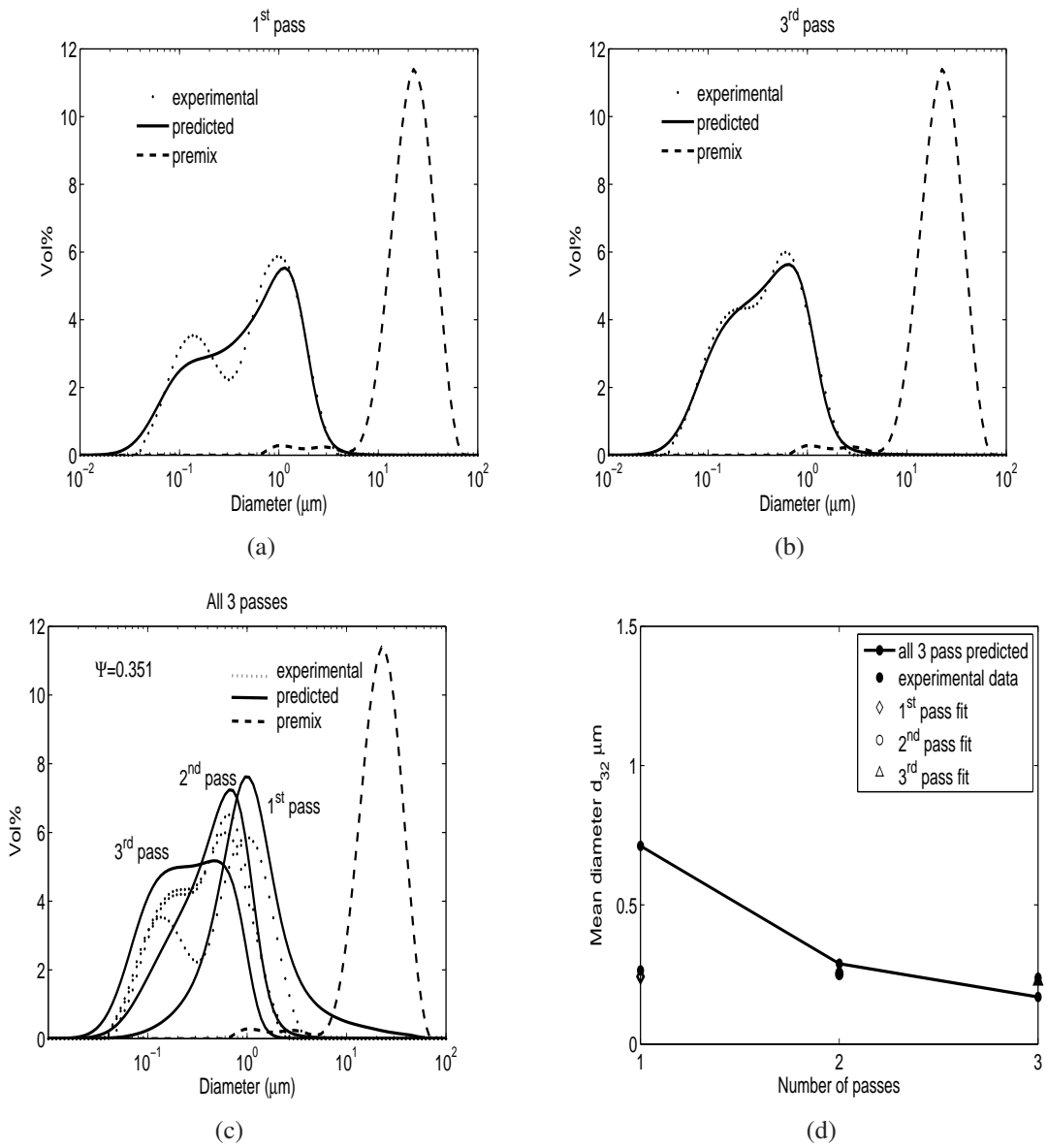
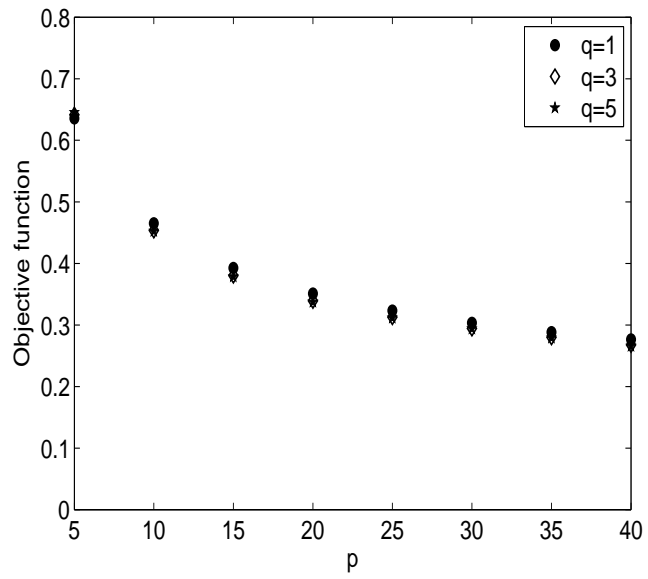
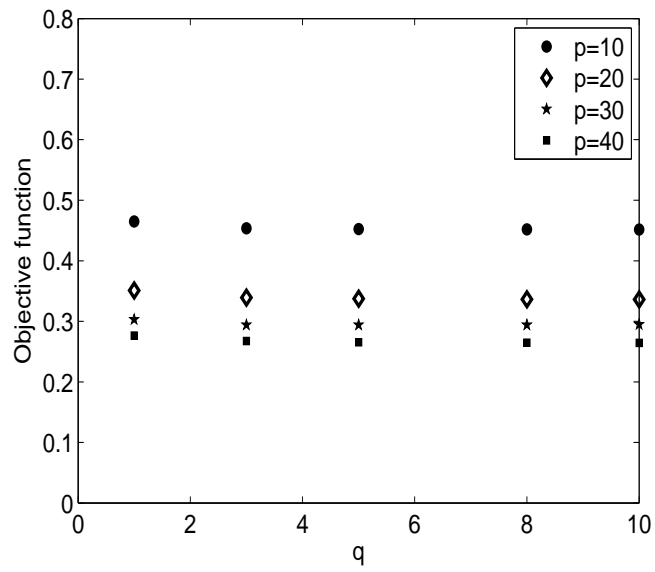


**Figure 4.3.** Drop size distribution predictions assuming multiple breakage (equation (4.9)) with  $q=1$  and  $p=20$ . (a) Predicted first pass drop size distribution. (b) Predicted third pass drop size distributions (c) Prediction drop size distributions for all 3 passes. (d) Experimental and predicted Sauter mean diameters  $d_{32}$  for all three passes.



(a)



(b)

**Figure 4.4.** Effect of the multiple drop breakage parameters  $p$  and  $q$  on objective function values. (a)Effect of  $p$ . (b) Effect of  $q$

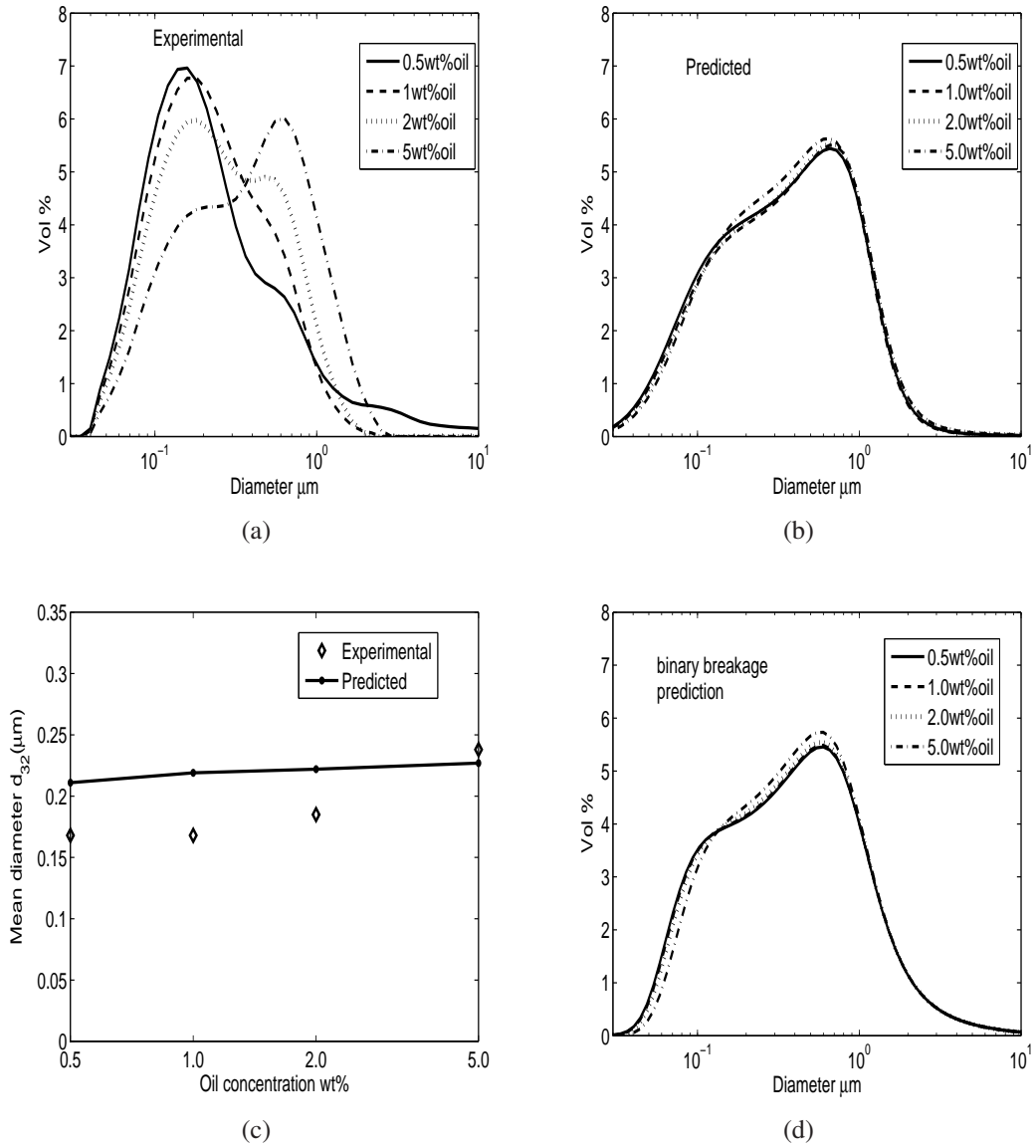


**Figure 4.5.** Effect of variable oil concentrations. (a) Experimental drop size distributions for the third pass. (b) Predicted drop size distributions for the third pass. (c) Experimental and predicted Sauter mean diameter  $d_{32}$  for all three passes. (d) Predicted drop size distributions for the third pass assuming binary drop breakage.

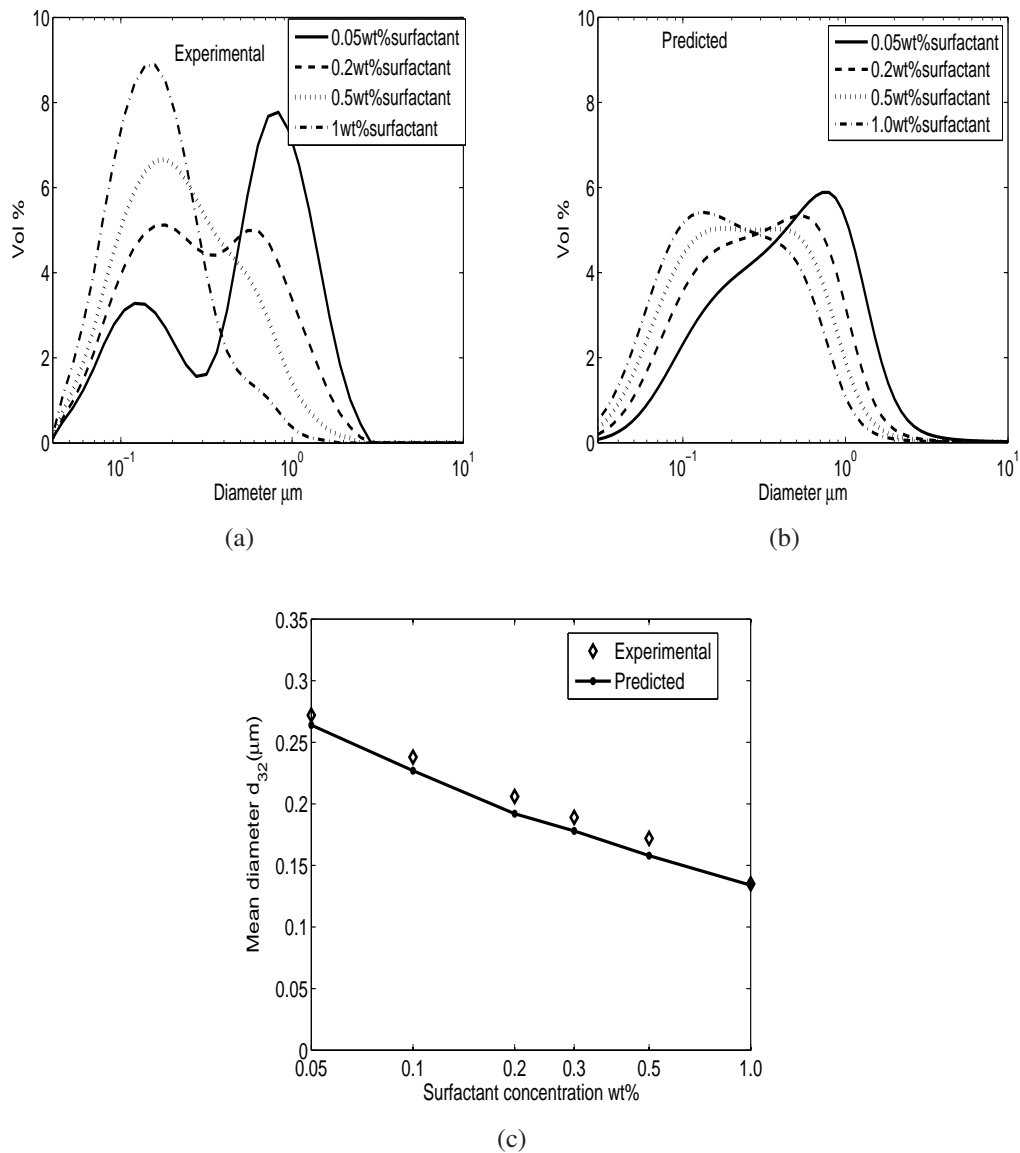


**Figure 4.6.** Effect of variable surfactant concentrations. (a) Experimental drop size distributions for the third pass. (b) Predicted drop size distributions for the third pass. (c) Experimental and predicted Sauter mean diameter  $d_{32}$  for all three passes.

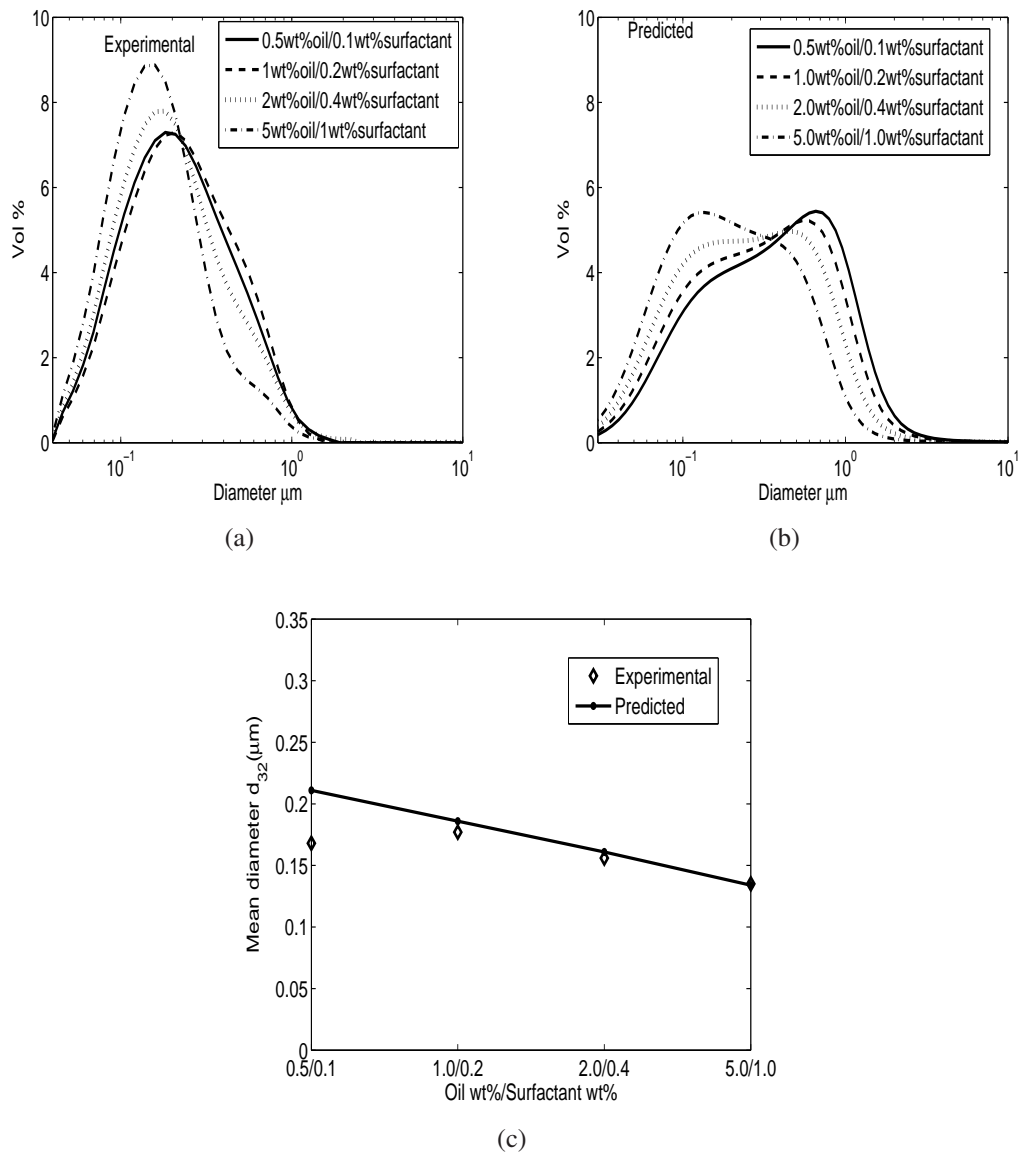


**Figure 4.7.** Effect of constant oil to surfactant ratio. (a) Experimental drop size distributions for the third pass. (b) Predicted drop size distributions for the third pass. (c) Experimental and predicted Sauter mean diameter  $d_{32}$  for all three passes.

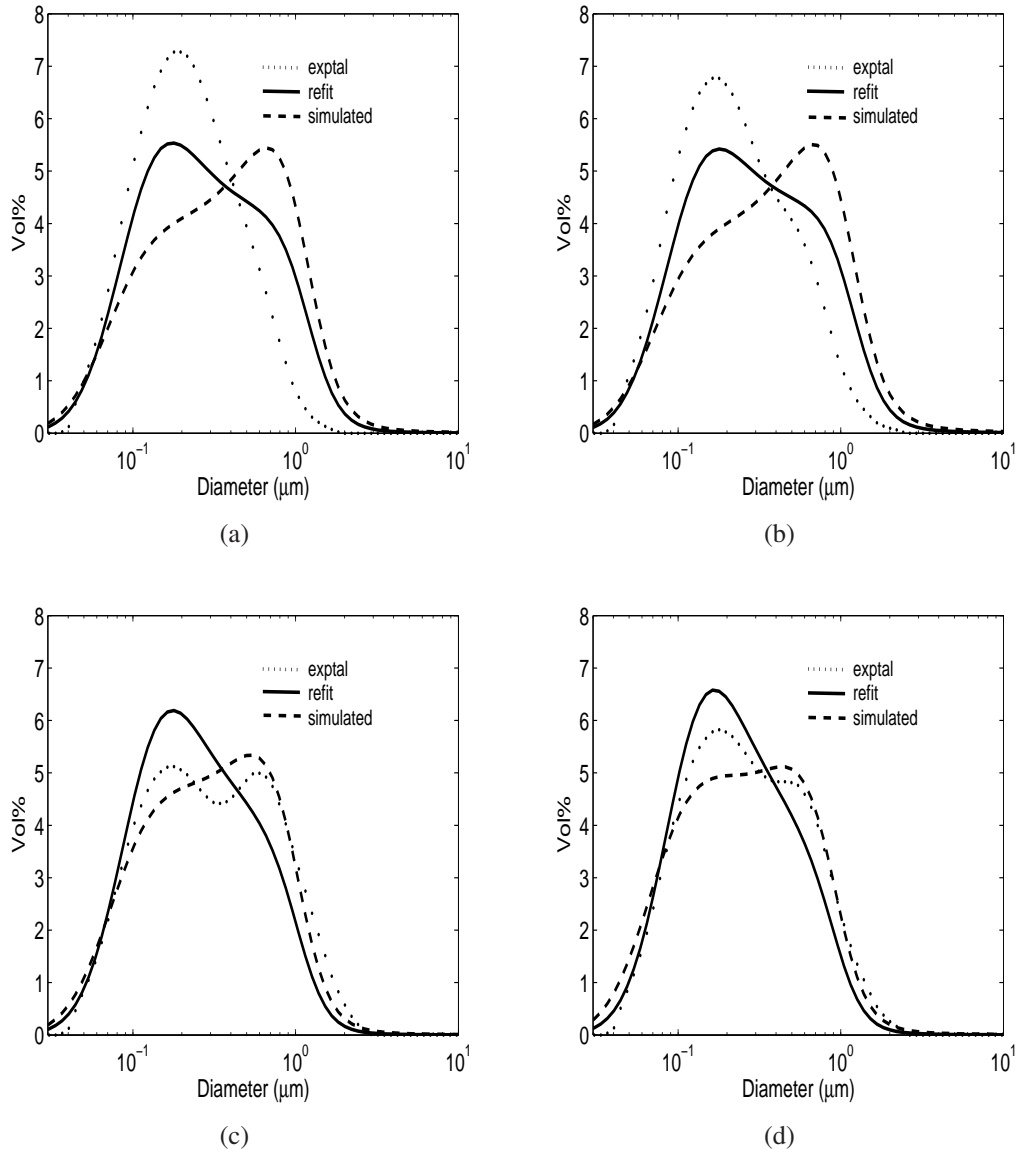


**Figure 4.8.** Re-estimation of the breakage rate parameters from a data set containing variable oil to surfactant ratios. Experimental and predicted drop size distributions for: a) 0.5wt% oil and 0.1wt% surfactant; b) 1.0wt% oil and 0.1wt% surfactant; c) 5.0wt% oil and 0.2wt% surfactant; and d) 5.0wt% oil and 0.3wt% surfactant.

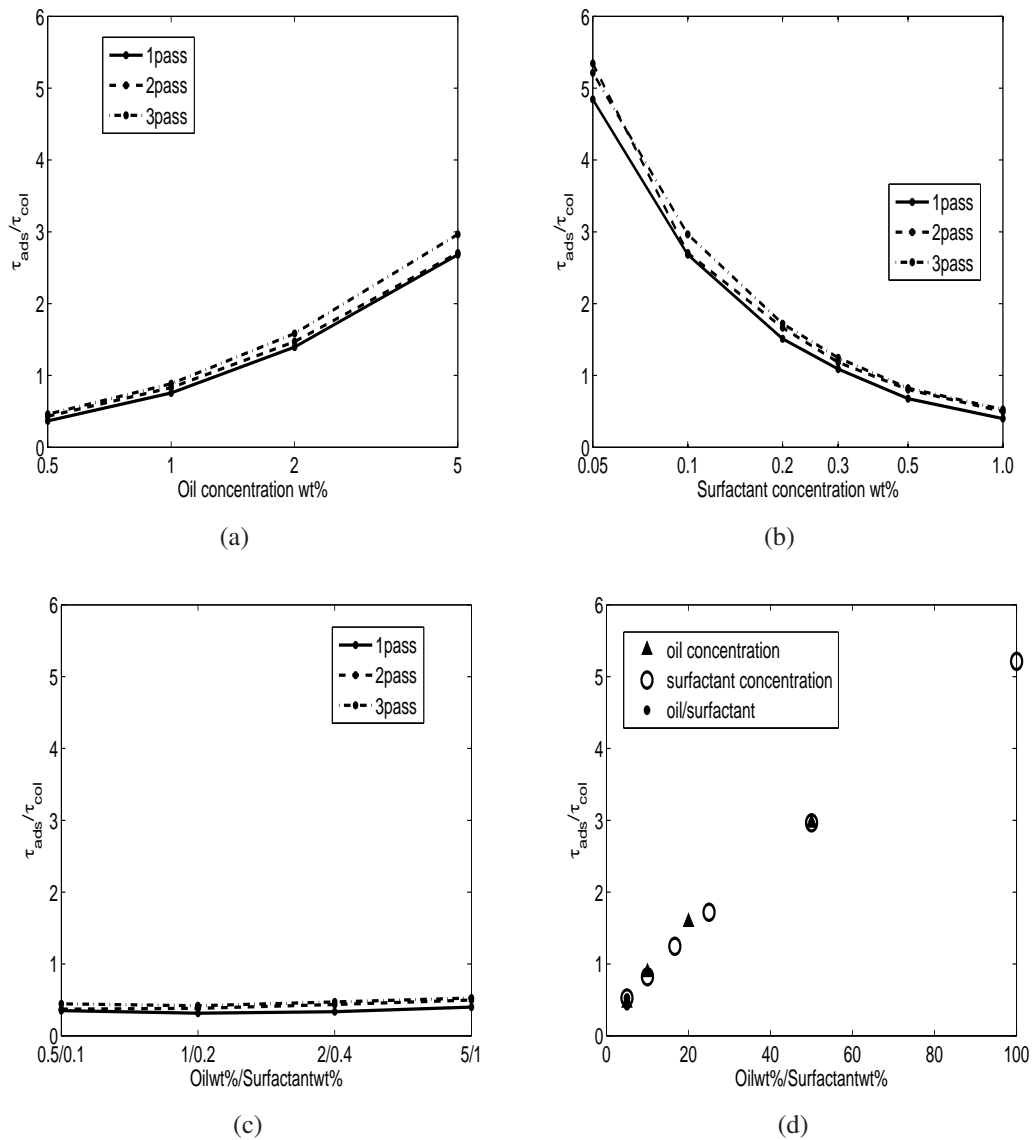


**Figure 4.9.** Ratio of adsorption to collision timescales. (a) Effect of oil concentration. (b) Effect of surfactant concentration. (c) Constant oil to surfactant ratio. (d) Effect of oil to surfactant ratio.

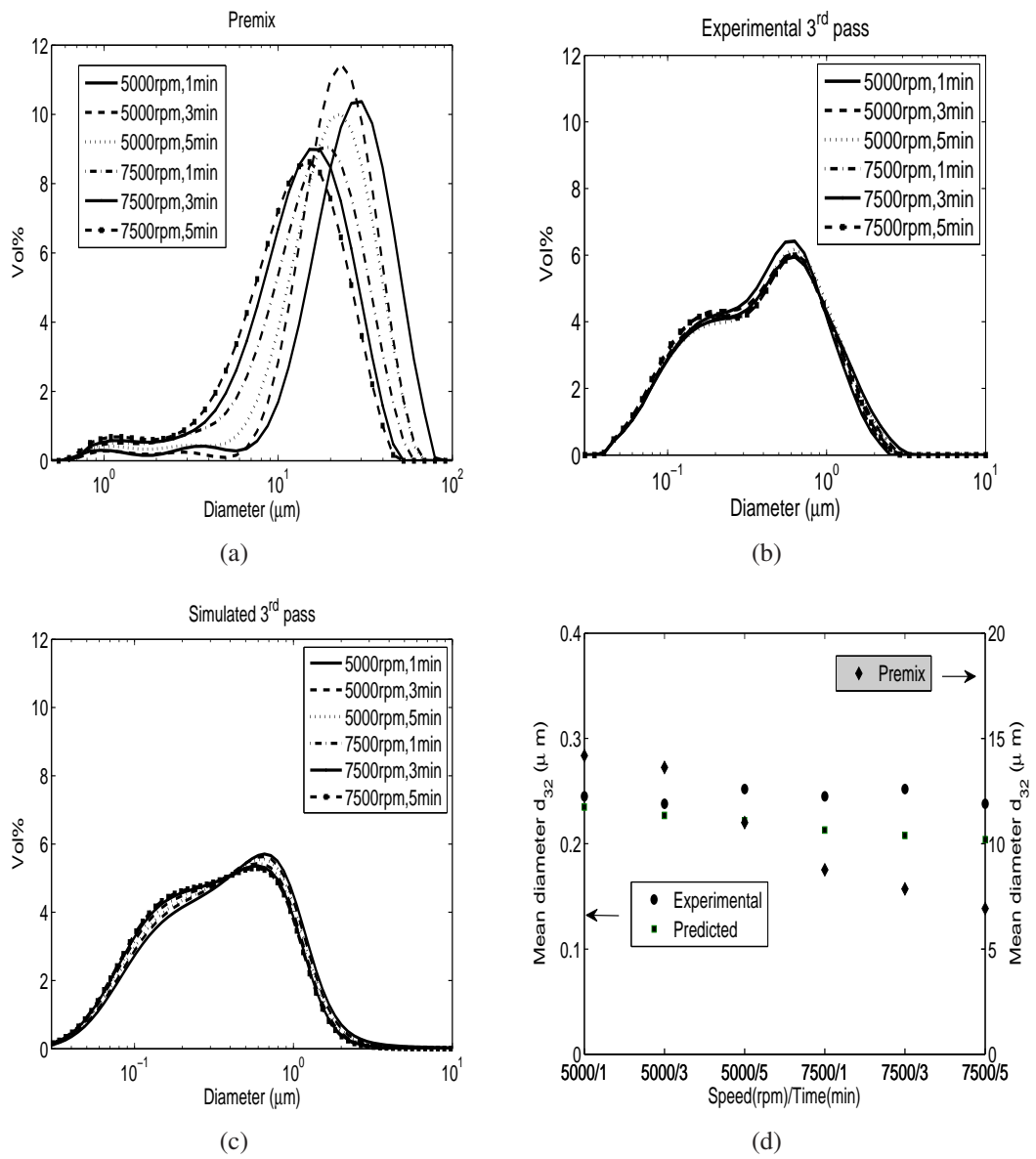


**Figure 4.10.** Effect of premix preparation. (a) Drop size distributions for the premixes. (b) Experimental drop size distributions for the third pass. (c) Predicted drop size distributions for the third pass. (d) Experimental Sauter mean diameters for the premixes and the third pass and predicted Sauter mean diameters for first pass.

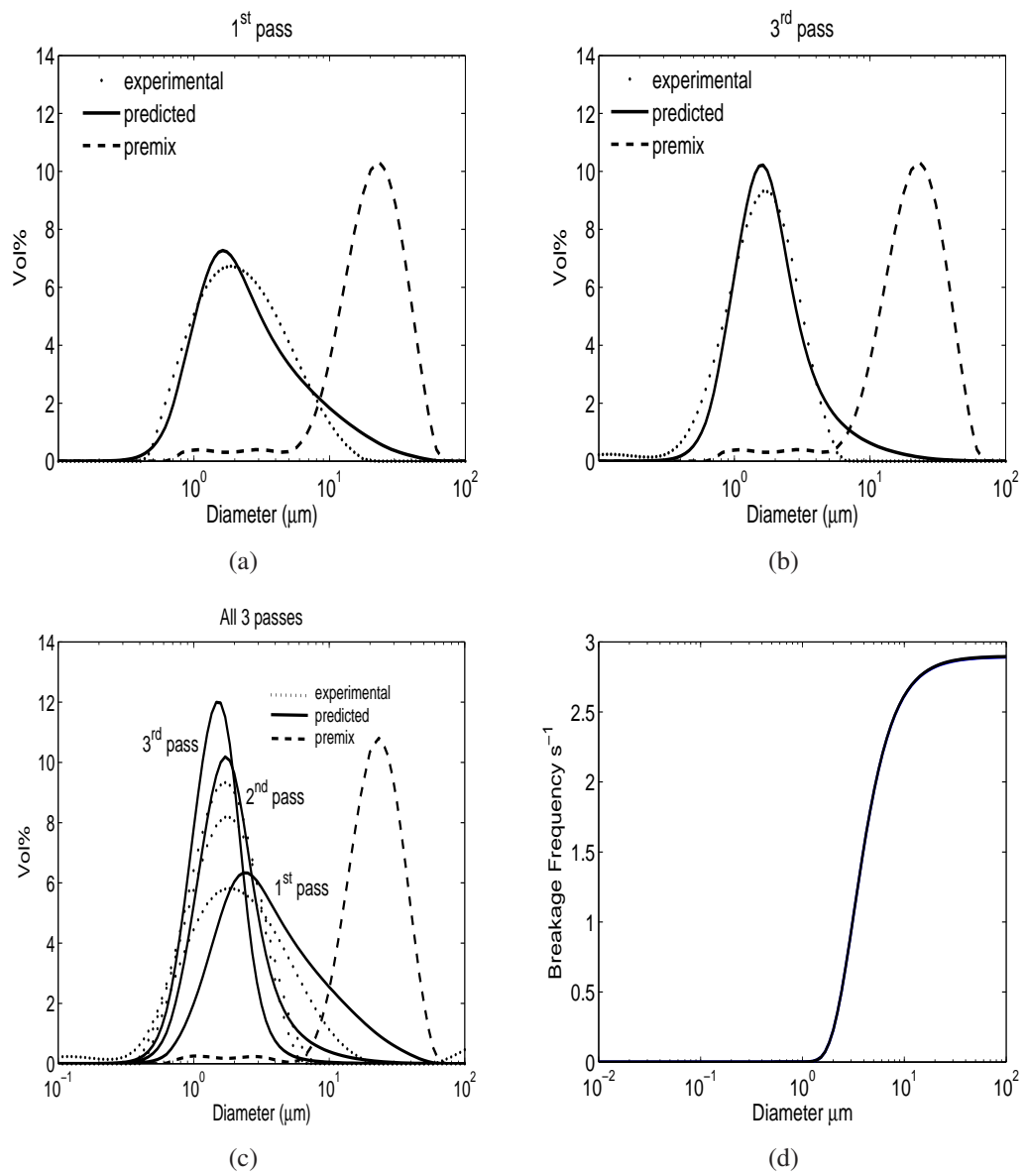


**Figure 4.11.** Effect of homogenization at no applied pressure. (a) Experimental and predicted first pass drop size distributions. (b) Experimental and predicted third pass drop size distributions, (c) Experimental and predicted drop size distributions for all three passes. (d) Breakage rate function  $g_3(v)$  estimated for all three passes.

## **CHAPTER 5**

### **PREDICTING THE EFFECT OF HOMOGENIZATION PRESSURE ON THE DROP SIZE DISTRIBUTIONS OF EMULSIONS IN A HIGH PRESSURE HOMOGENIZER**

In this chapter, we attempt to improve upon the previously encountered deficiencies in the model in terms of pressure predictions. We identified some effects which could be incorporated to have more realistic predictions. These were added sequentially to the model and their contribution to model improvement was evaluated. The effects considered include sample heating, interfacial tension increase with passes, maximum stable diameter, surfactant depletion and number of daughter drops. The critical effects were found to be maximum stable diameter and the number of daughter droplets. The improved model extensibility was also successfully tested for a range of formulation but at constant ratio of oil to surfactant with the aim of keeping coalescence to the minimum. We also made a preliminary attempt at using the model for designing of experiments for target formulation. The concept of attainable region was used and the model design predictions were also tested experimentally.

#### **5.1 Materials and Methods**

##### **5.1.1 Experimental Methods**

###### **Materials**

We used soybean oil (Spectrum Organic) as the dispersed phase, nanopure water as the continuous phase, and the non-ionic surfactant Pluronic F-68 (Sigma Aldrich) as the emulsifier. The base case emulsion consisted of 5wt% oil and 1wt% surfactant with the

remainder water. High surfactant concentrations were used to minimize the possibility of coalescence. Emulsions were also prepared at concentrations different than the base case but keeping the ratio of oil to surfactant constant at the base case value of 5. The different dispersed phase and surfactant concentrations are listed in Table 5.1

### **Emulsion Preparation**

Emulsions were prepared using a two-step process. First a coarse premix was prepared by mixing the different ingredients in a stator-rotor device (Ultra-Turrax Model T25, Rose Scientific Ltd.) at 16000 rpm for 15 minutes. A standard premix was made at 40 wt% oil and 8 wt% surfactant and then diluted to concentrations in table 5.1 to ensure similar initial drop size distribution for all the experiments. The premix was then processed in a high-pressure homogenizer (Emulsiflex C-3, Avestin Inc.) where it was homogenized to a fine emulsion at the studied pressures to generate the first pass. The first pass was then reprocessed to generate subsequent passes. 5 passes were collected in total and along with premix analyzed for the drop size distribution. 5 homogenization pressures were used ranging from 250 bar to 1250 bar in steps of 250 bar.

### **Emulsion Characterization**

Drop size distributions were measured using a static light scattering device (Malvern Mastersizer S). Oil-water interfacial tensions were measured by drop shape analysis (KRUSS Instruments Model DSA-10 Tensiometer, KRUSS) at 25°C. Densities of the emulsion samples was measured using a Densitometer. Viscosities of the constituent phases were measured using a TA-Ar stress controlled rheometer (Texas Instruments).

#### **5.1.2 Theory**

##### **Population Balance Equation Model**

We used the population balance equation (PBE) model similar to our previous work for a pure breakage process of emulsification through a high pressure homogenizer [81]. We

assumed coalescence to be negligible which is reasonable when the amount of surfactant is high enough. Considering the limiting case of breakage, the population balance equation can be written as [16, 18, 19]

$$\frac{\partial n(v, t)}{\partial t} = -g(v)n(v, t) + \int_0^\infty \beta(v, v')g(v')n(v', t)dv' \quad (5.1)$$

here:  $n(v, t)dv$  is the number of drops in the volume range  $[v, v + dv]$  per unit volume of the dispersion;  $g(v)$  is the breakage rate i.e. the fraction of drops of volume  $v$  breaking per unit time; and  $\beta(v, v')$  is the daughter drop distribution function representing the probability of forming a daughter drop of size  $v$  from breakage of a mother drops of size  $v'$ . The high-pressure homogenizer was modeled as a well-mixed batch system with each pass corresponds to one dimensionless time unit. The initial condition is the measured drop volume distribution of the premix.

We use the reformulated version of the PBE model in terms of volume percent distribution as in equation 5.2 since the particle size analyzer provides measurements of the volume percent distribution  $n_p(v, t)$ ,

$$\frac{\partial n_p(v, t)}{\partial t} = -g(v)n_p(v, t) + v \int_0^\infty \frac{g(v')\beta(v, v')n_p(v', t)}{v'} dv' \quad (5.2)$$

We need to specify the breakage rate  $g(v)$  and the daughter drop distribution function  $\beta(v, v')$  which includes the number of daughter drops formed on breakage. Consistent with our prior work, we have considered breakage of drops by both inertial ( $g_1(v)$ ) and viscous forces  $g_2(v)$  under turbulent conditions [81]. The turbulent inertial breakage rate  $g_1(v)$  is modified version of previously proposed function [19] and then extended to high-pressure homogenizer using equation (5.6) for energy dissipation rate.

$$g_1(v) = K_1 v^{-2/9} \epsilon^{1/3} \exp \left[ -\frac{K_2 \sigma (1 + \phi)^2}{\rho_d v^{5/9} \epsilon^{2/3}} \right] \quad (5.3)$$

The second breakage rate  $g_2(v)$  was derived considering breakage of drops due to turbulent viscous forces [81].

$$g_2(v) = K_3 \left( \frac{2}{\pi} \right)^{1/2} \left( \frac{\epsilon \rho_d}{\eta_d} \right)^{1/2} \exp \left( \frac{-K_4 \sigma^2 \lambda}{\eta_c v^{2/3} \epsilon \rho_d} \right) \quad (5.4)$$

The resultant breakage rate is the sum of the two individual breakage rates representing the two mechanisms. In these two equations,  $K_1 - K_4$  are adjustable constants to be calculated from parameter estimation.

$$g(v) = g_1(v) + g_2(v) \quad (5.5)$$

We have used the following description for the energy dissipation rate  $\epsilon$  term (equation 5.6) [113, 114]

$$\epsilon = \frac{\Delta P Q}{V_{diss}} \quad (5.6)$$

where,  $\Delta P$  is the applied pressure,  $Q$  is the flowrate and  $V_{diss}$  is valve gap volume which is given by equation (5.7). The valve gap  $h_{gap}$  was calculated by rearranging the following expression (equation 5.8) of Phipps [77] retaining only the last term.

$$V_{diss} = \frac{\pi}{4} (D_o^2 - D_i^2) h_{gap} \quad (5.7)$$

$$\Delta P = \frac{\rho_c}{4} \left( \frac{Q}{\pi D_i h_{gap}} \right)^2 - \frac{\rho_c}{2} \left( \frac{Q}{\pi D_o h_{gap}} \right)^2 - \left( \frac{5\rho_c}{h_{gap}^3} \right) \left( \frac{\eta_c}{\rho_c} \right)^{3/5} \left( \frac{Q}{2\pi} \right)^{7/5} \left[ \left( \frac{D_i}{2} \right)^{-2/5} - \left( \frac{D_e}{2} \right)^{-2/5} \right] \quad (5.8)$$

$$h_{gap} = \left( \frac{5\rho_c}{\Delta P} \right)^{1/3} \left( \frac{\eta_c}{\rho_c} \right)^{1/5} \left( \frac{Q}{2\pi} \right)^{7/15} \left[ \left( \frac{D_i}{2} \right)^{-2/5} - \left( \frac{D_e}{2} \right)^{-2/5} \right]^{1/3} \quad (5.9)$$

For the daughter drops formation from mother drop we considered multiple drop generation. The daughter drop distribution function was considered to be the power law product form of the generalized Hill-Ng distribution [24, 40, 125].

$$\beta(v, v') = \frac{p}{\mathbf{B}(q, r)} \left(\frac{v}{v'}\right)^{q-1} \left(1 - \frac{v}{v'}\right)^{r-1}, \quad r = q(p-1) \quad (5.10)$$

In this the number of daughter drops is included in the daughter drop distribution function itself through the parameter  $p$ . This is a generalized beta daughter distribution function for  $p$  daughter drops such that  $p \geq 2$  and  $q > 0$ .  $\mathbf{B}(q, r)$  is a beta function and  $q$  decides the shape of the distribution function. For  $q = 1$ , we get the following simplified equation 5.11 which is uniform distribution for  $p$  daughter drops.  $p$  needs to be specified *a priori* and its effect on the predictions is discussed in detail later.

$$\beta(v, v') = p(p-1) \left(1 - \frac{v}{v'}\right)^{p-2} \quad (5.11)$$

We also used the full version of the PBE model as listed in equation (5.12) for testing the significance of coalescence in our experimental system

$$\begin{aligned} \frac{dn(v, t)}{dt} = & -g(v)n(v, t) - \int_0^\infty \beta(v, v')g(v')n(v', t)dv' \\ & -n(v, t) \int_0^\infty C(v, v')n(v', t)dv' + \frac{1}{2} \int_0^\infty C(v-v', v')n(v', t)n(v-v', t)dv' \end{aligned} \quad (5.12)$$

where:  $C(v, v')$  is the coalescence frequency and is the product of collision frequency  $h(v, v')$  and coalescence efficiency  $\lambda(v, v')$ . The following functions were used for collision frequency and coalescence efficiency [19]

$$h(v, v') = K_5 \frac{\epsilon^{1/3}}{1 + \phi} (v^{2/3} + v'^{2/3})(v^{2/9} + v'^{2/9})^{1/2} \quad (5.13)$$

$$\lambda(v, v') = \exp \left[ -K_6 \frac{C\mu_c \rho_c \epsilon}{\sigma^2} \left( \frac{v^{1/3}v'^{1/3}}{v^{1/3} + v'^{1/3}} \right)^4 \right] \quad (5.14)$$

The PBE model (5.2) was solved numerically by discretizing the integro-differential equation with 100 node points. The resulting system of 100 nonlinear ordinary differential equations describing the time evolution of the volume percent distribution at each node point was solved using the Matlab integration code `ode45`. The measured distribution of the coarse emulsion i.e. the premix was used as the initial condition  $n_p(v, 0)$ .

### Parameter Estimation

The PBE model has terms which depend on the constituent ingredient properties and some adjustable constants. Formulation properties i.e. density, viscosity, interfacial tension can be measured experimentally and can be used as inputs to the model. However, the model constants  $K_1 - K_4$  need to be estimated and is done using a systematic nonlinear optimization approach instead of trial-and-error approach. The PBE model was spatially discretized using 100 node points and temporally discretized using orthogonal collocation on finite elements. 5 finite elements with 2 internal collocation points were used such that each pass was at the end of a finite element. We observed that addition of points and/or finite elements did not change the parameter estimates but increased the computational effort and on the other hand decreasing the number of points produces substandard solution. We pooled in all the pressure sets and a combined set of parameters  $K_1 - K_4$  which are the decision variables and were estimated for the entire range of pressure. The problem is then posed as a constrained minimization problem with the following objective function (equation 5.15) and equality constraints corresponding to the discretized model equations and continuity conditions across the finite elements.

$$\Psi_T = \sum_{p=1}^{N_p} \sum_{i=1}^N \sum_{j=1}^n \frac{[\hat{n}_p(p, v_j, i) - n_p(p, v_j, i)]^2}{[n_p(p, v_j, i)]^2} \quad (5.15)$$

where  $n_p(v_j, i)$  is the measured drop size distribution corresponding to drop volume  $v_j$  and  $i^{th}$  homogenizer pass,  $\hat{n}_p(v_j, i)$  is corresponding predicted value from the PBE model (5.2),  $n$  is the total number of node points,  $N$  is the number of passes, and  $N_p$  is the

number of pressure sets. From the results point of view we also estimated the pass by pass objective function  $\Psi_j$  as well the objective function for each pressure set  $\Psi_i$ . The optimization problem was formulated in AMPL [29] and solved using the nonlinear solver CONOPT.

### **Surfactant concentration and interfacial tension [68]**

The role of surfactant is to adsorb at the oil-water interface and thereby reduce the interfacial tension facilitating breakup. In addition to this it also stabilizes the newly formed emulsion droplets. The reduction in the interfacial tension in the presence of a surfactant is referred to as surface pressure  $\Pi$  (equation 5.16) and is proportional to the surfactant concentration.

$$\Pi = \sigma_{o/w} - \sigma \quad (5.16)$$

Here,  $\sigma_{o/w}$  is the interfacial tension in the absence of surfactant i.e. pure oil-water, and  $\sigma$  is the interfacial tension corresponding to the amount of surfactant present in solution. The Gibb's adsorption isotherm (equation 5.17) can be used to relate the surface load ( $\Gamma$ ) which is the amount of surfactant present at the interface to the interfacial tension and the surfactant concentration in the bulk solution. These can be obtained experimentally from measurements of oil-water interfacial tension for various amounts of surfactant.

$$\Gamma = -\frac{1}{aRT} \frac{d\sigma}{d\ln(c)} \quad (5.17)$$

where,  $a$  is the parameter which depends on the solute and is 1 for non-ionic and 2 for ionic surfactants.  $c$  is the aqueous phase surfactant concentration,  $R$  is the gas constant and  $T$  is the absolute temperature. Thus  $\Gamma$  can be estimated from the first order derivative of  $\sigma$  versus  $\ln(c)$  plot as given in equation 5.17. The Gibbs adsorption isotherm also allows expression of the surface pressure  $\Pi$  in terms of the surface load  $\Gamma$ .

$$\Pi = \sigma_{o/w} - \sigma = aRT \int_0^c \Gamma(c) d\ln c \quad (5.18)$$

The Langmuir adsorption isotherm (equation 5.19) relates the amount of surfactant at the interface to its concentration  $c$  and surface activity  $1/c_{1/2}$

$$\frac{\Gamma}{\Gamma_{\infty}} = \frac{c/c_{1/2}}{1 + c/c_{1/2}} \quad (5.19)$$

$\Gamma_{\infty}$  is the surface load when all the interface is completely covered with surfactant, and  $c_{1/2}$  is the surfactant concentration when  $\Gamma = 1/2\Gamma_{\infty}$ . Substituting equation 5.19 in the equation 5.18 for surface pressure, we can get the interfacial tension as a function of bulk concentration as follows

$$\sigma = \sigma_{o/w} - aRT\Gamma_{\infty} \ln \left( 1 + \frac{c}{c_{1/2}} \right) \quad (5.20)$$

The surfactant concentration  $c$  in solution can be calculated by subtracting the amount of surfactant adsorbed at the interface from the initial amount added. The amount of surfactant adsorbed can be calculated from equation 5.21.

$$c_{ads} = \frac{6\Gamma\phi}{d_{32}} \quad (5.21)$$

### Heating effect and Critical diameter

Significant amount of sample heating occurs in a high pressure homogenizer and the temperature rise increases with increase in pressure applied. Part of the energy applied is thus lost to the sample and also to the instrument. Knowing the specific heats of the constituents  $C_{p_{oil}}$  &  $C_{p_{water}}$  and the temperature rise of the sample  $\Delta T$  and the instrument  $\Delta T_{ins}$ , the thermal losses can be estimated by equation 5.22

$$E_H = \rho_s(\phi C_{p_{oil}} + (1 - \phi)C_{p_{water}})\Delta T + \rho_c C_{p_{water}}\Delta T_{ins} \quad (5.22)$$

where,  $E_H$  is the thermal loss and  $\rho_s$  is the sample density.

The maximum stable diameter for the turbulent inertial breakup is given by equation 5.23. This is the critical diameter below which drops cannot be broken down but can only be formed from breakup of bigger drops. The term on the right hand side of equation 5.23 except the proportionality is labeled as  $d_{ti}$  and listed in equation 5.24.

$$d_{max} = c_1 \frac{\sigma^{3/5}}{\epsilon^{2/5} \rho_c^{1/5}} \quad (5.23)$$

$$d_{ti} = \frac{\sigma^{3/5}}{\epsilon^{2/5} \rho_c^{1/5}} \quad (5.24)$$

## 5.2 Results and Discussion

### 5.2.1 Base case model

The base case model is the version of the model with minimal features added and is the reference point for all future comparisons. For the base case, we used 5 wt% oil and 1 wt% surfactant and prepared emulsions at 5 different pressures (250 bar - 1250 bar) and 5 passes were collected for each pressure. We used the breakage rate to be sum of turbulent inertial and viscous breakage (equation 5.3 & 5.4) with the energy dissipation rate given by equation 5.6. Consistent with our previous work [80], we used multiple drop breakage with 20 drops. Nonlinear optimization involving minimization of the total objective function to estimate the decision variables  $K_1 - K_4$  was performed. The pass by pass objective function  $\Psi_j$ , objective function for a particular pressure  $\Psi$  and total objective function  $\Psi_T$  (equation 5.15) were used as the error measures to analyze the deviations of the predicted distribution from the experimental data. For the base case, the value of the total objective function  $\Psi_T$  was observed to be 4.46. The model results for the base case is shown in figure (5.1(a))-(5.1(c)) for three of the five pressures studied. Each pressure set shows the experimental data and the model prediction for 1<sup>st</sup>, 3<sup>rd</sup> and 5<sup>th</sup> pass and also reports the objective function for that pressure. The lower and higher pressures have higher objective

function values compared to the 750 bar indicating underprediction at lower pressures and overprediction at higher pressures. Figure (5.1(d)) shows the trends in the pass by pass objective function with respect to the number of passes. It is seen from figure (5.1(d)) that for 250 bar the deviation is higher at initial passes and decreases towards higher passes. This is consistent with the underprediction observed for this pressure. For higher pressures, the deviation is more at initial and final passes and minimum in the middle.

We also tested the full version of the PBE model including coalescence and tried to estimate all 6 constants, i.e. 4 for breakage and 2 for coalescence. For coalescence, we could estimate with only one pressure set at a time because of the limitations in problem size that AMPL can handle. For the base case formulation at all pressures, the optimizer set  $K_6$  equal to zero implying the zero coalescence frequency. This occurred over a wide range of initial guesses implying that breakage was dominant over coalescence. In our previous work [81], we did an explicit test for coalescence for 0.5 wt% oil and 0.1 wt% surfactant and found it to be negligible under these conditions. Although, we have used a higher oil concentration in this work, we expect coalescence to be minimal here as well since the ratio of oil to surfactant is same as used in the test. This being the case, we used the breakage only model for all the future tests and did not pursue coalescence any further.

### **5.2.2 Heating effects**

Substantial rise in temperature of the emulsion was observed at the exit of the homogenizer which increases as the pressure was increased. This temperature rise at the end of each pass was measured and the emulsion was cooled back down to starting temperature before generating the next pass. The temperature rise was averaged over all the 5 passes for each pressure and is reported in figure (5.2(a)) with the error bars representing the standard deviation. This rise in temperature was used to calculate the loss in energy due to thermal effects i.e. heating of the sample. Some of energy is also lost to heating of the homogenizer which was measured by passing water and measuring the rise in temperature. Since part of

the available energy is lost to heating the sample, not all of it available for drop disruption. The available mechanical energy can be calculated by subtracting the thermal contribution  $E_H$  calculated using equation 5.22 from the applied pressure.

The resultant effective pressure is also represented in figure (5.2(a)). The model now with the effective pressure was re-optimized for the constants  $K_1 - K_4$ . The model predictions after including the heating effects is shown in figure (5.2). The objective function decreases from 4.46 to 3.89 which is a 13 % improvement over the base case. Bigger improvement is obtained for 250 bar and 1250 bar whereas the predictions at 750 bar continue to be reasonably good as before as seen in figures 5.2(b)-5.2(c).

### 5.2.3 Interfacial tension effect

The oil-water interfacial tension in the presence of surfactant is related to the surfactant concentration as explained in section 5.1.2. The interfacial tension was measured as a function of concentration using drop shape analysis tensiometer and the data is shown in figure (5.3(a)). The interfacial tension data was fit to a quadratic equation and the first order derivative was used to calculate the surface load as a function of concentration using the equation (5.17). The normalized value of surface load ( $\Gamma/\Gamma_\infty$ ) is shown in figure (5.3(b)) and was used to estimate  $c_{1/2}$ . These values can be used to correlate the interfacial tension to the amount of surfactant remaining in solution using equation (5.20) described in section 5.1.2.

To include the effect of interfacial tension in our model, we start with the interfacial tension value corresponding to the amount of surfactant added. Then as the drops get smaller and smaller more and more surfactant is adsorbed at the interface and so the amount of free surfactant decreases. Since the amount of surfactant in solution decreases with successive passes, the resultant interfacial tension increases and therefore the breakup rate goes down. With this feature included in the model, re-optimization was performed to get the best values of the parameters  $K_1 - K_6$ . Incorporating the increase in interfacial tension

with subsequent passes in our model, the predictions were improved and hence the objective function decreased by 17% over the base case (figure(5.4)), the new value of objective function being 3.68. The increase in interfacial tension with the number of passes is shown in figure (5.4(a)). It is seen from this figure that the increase is not substantial at lower pressures but significant at higher pressures. The model predictions with the experimental data is shown in figures (5.4(b)-5.4(d)). Including this effect shows maximum benefit at 1250 bar and although the overall improvement is not huge, it does need to be incorporated to have the correct physics included in the model

#### 5.2.4 Critical diameter limit

To get an estimate of the maximum stable diameter from experimental data we observed the drop distributions for all the sets. The drop distribution was seen to stabilize around the fourth and fifth pass and hence the Sauter mean diameter  $d_{32}$  for the fifth pass was considered to be the steady state diameter possible. The proportionality constant  $c_1$  in equation 5.23 was estimated by fitting the fifth pass  $d_{32}$  to the critical diameter  $d_{ti}$  from equation 5.24. Figures (5.5(a))-(5.5(c)) show the fitting relations for two formulations namely 5wt% oil with 1wt% surfactant and 10wt% oil with 2wt% surfactant. The slopes in case of both formulations are similar indicating that any one of the formulation set is sufficient to estimate the proportionality constant. Since the maximum stable is the limiting diameter below which drops cannot break further, this concept was included in our PBE model such that when the ratio of mean diameter  $d_{32}$  to  $d_{max}$  falls below unity, the breakage rate is set to zero.

We have shown the effect of including this limit in our model in figures (5.6(a))-(5.6(c)). From figure (5.6(d)), we see that the ratio of  $d_{32}/d_{max}$  starts to fall below 1 at about 750 bar and does so till 1250 bar. Since the limit is not active for 250 and 500 bar pressure, this case was not shown in figure 5.6(d). The critical diameter limit becomes active between the 3<sup>rd</sup> pass and 4<sup>th</sup> pass for 750 bar and between the 2<sup>nd</sup> pass and 3<sup>rd</sup> pass for 1250

bar set. Including this effect helps to correct the model overprediction observed at higher pressures seen by the reduction in objective function for 1250 bar (figure 5.6(c)). The overall objective function on inclusion of this effect decreased to 2.85 which was a 36% improvement over the base case.

### **5.2.5 Surfactant limit**

We also included the effect of surfactant concentration in addition to the interfacial tension. If there is insufficient amount of surfactant in the system, there might not be enough breakage. Hence, if the ratio of added surfactant to adsorbed surfactant drops below 1, we imposed that the breakage rate goes to zero. The amount of surfactant adsorbed is calculated from equation 5.21. We tried to include this effect alongwith all the above discussed effects. However, in all the cases discussed above we had sufficient amount of surfactant and this effect does not occur independent of the critical diameter effect. So, we tried it on another independent test case with 5 wt% oil and 0.1 wt % surfactant for 250 bar pressure. Only at lower pressure, we observed that the surfactant limit goes below unity without the critical diameter limit doing the same. From figure (5.7(b)), we see that the surfactant limit becomes active after the 3<sup>rd</sup> pass even though the diameter ratio is always above 1. The model predictions with this limit included is shown in figure (5.7(a)). Although not important in our case, this test proves that the effect maybe dominant under certain conditions especially when coalescence is also present.

### **5.2.6 Effect of number of daughter drops**

In all the cases considered above we assumed the number of daughter drops to be 20 similar to our previous work. However, we thought it would be worthwhile to check the effect of number of daughter droplets which was hence varied from 10 to 500 and the model was reoptimized to get new objective function values. In figure (5.8(a)), is plotted the objective function versus the number of daughter drops formed on breakage. The objective function decreases on increasing the number of daughter drops till about 150 drops and then

it increases with increasing the number of drops further. Since a minimum was observed at 150 drops, all the above effects were added to the base case model but with 150 drops instead of 20. From figures (5.8(b)-5.8(d)), we see a large improvement in the objective function in all the cases. The total objective function reduced significantly to 1.69 which in total is 62 % improvement.

### **5.2.7 Overall trends in the objective function**

The contribution of all the different effects discussed above towards the objective function is shown in figure (5.9). We also simulated other oil and surfactant concentrations listed in table 5.1 using the constants optimized for the base case formulation. The heating effect affects positively for 5 wt % oil, negatively for 10 wt% oil and no effect for 20 wt% oil. All the other effects considered improve the total objective function uniformly over all the formulations tested. The objective function values and the percentage improvement is tabulated in table 5.2 for the base case formulation. Significant reduction in objective function was observed on including the critical diameter effect since it helps to avoid the overprediction of the distributions observed at higher pressures. Increasing the number of daughter drops from 20 to 150 also shows a substantial decrease in objective function over all the pressures and formulations considered. This test enabled us to weigh the contributions of the different effects towards reducing the objective function. We think that the most important effects to include would be the critical diameter and daughter drop distribution function.

### **5.2.8 Design**

The PBE model was improved over the basic version by adding features which resulted in a final reduction of about 62% in the objective function value and the constants evaluated were applicable over a wide range of operating pressure. The next step once we had a decent model was to use it for experimental design. For this, the model predicted mean diameters  $d_{32}$  and  $d_{43}$  for 5 wt% oil and 1 wt% surfactant were used to construct the

attainable region of drop sizes for the high pressure homogenizers. At a given pressure, the successive passes can be considered to be homogenizers in series. The starting point is the initial condition and the  $d_{43}$  versus  $1/d_{32}$  is plotted for different passes at a given pressure (figure 5.10(b)) which is analogous to residence time for reactor networks [23,31]. For an emulsion breakup process, the  $d_{43}$  decreases with increasing homogenizers in series equivalent of number of passes whereas the  $1/d_{32}$  increases. This allows construction of a convex attainable region with easy visualization of the average properties. Although only two mean properties are not enough to characterize the whole distribution, this method allows us to generate possible alternatives for target emulsions with desired properties. The whole PBE model can then be used to evaluate the entire distribution and compare with the target.

In figure (5.10(c)), we plot  $d_{43}$  versus  $1/d_{32}$  for all passes and pressures. The vertical lines are lines of constant  $d_{32}$  and the dashed lines correspond to different values of polydispersity defined in equation (5.25). The premix is omitted in this figure to expand the scale.

$$p.d. = \frac{d_{43}}{d_{32}} \quad (5.25)$$

From the figure (5.10(c)), we see that it is not possible to get a monodispersed ( $p.d.=1$ ) emulsion with any configuration since it is outside the attainable region. Possible values of polydispersity are 2 or higher.

As examples, we have considered 2 targets, Target I: mean diameter  $d_{32}$  of 500 nm or 0.5  $\mu\text{m}$  and a polydispersity of 2,  $p.d. = 2$ , and Target II: mean diameter  $d_{32}$  of 250 nm or 0.25  $\mu\text{m}$  and a polydispersity of 2,  $p.d. = 2$ . To identify possible combination we need to see which pressure lines lie at the intersection of  $p.d. = 2$  and the vertical line for corresponding  $d_{32}$ . From the plot, we see that there are 2 possible options for reaching either of the two targets: 3.5 passes at 500 bar and 2.25 passes (slightly above 2 passes) at 750 bar for Target I and 2.75 passes at 1000 bar and 2.33 for 1250 bar. These options are listed in table 5.3 and the best choice in either case would be the one with the

minimum energy requirement. However, since it not possible to generate fractional passes, we generate a whole pass at a lower pressure which has the same energy requirement as the fractional pass. The energy dissipation rate versus pressure curve in figure 5.10(a) can be used as a guide to choose an intermediate pressure which has same  $\epsilon$  as the fractional pass.

To implement the options in table 5.3, the experimental strategy in table 5.4 based on matched energy dissipation rate was used. The experimentally obtained  $d_{32}$  and polydispersities are listed in the same table. The model predictions using the following strategy is also listed. The model predicts that the conditions listed yield the right  $d_{32}$  and  $p.d.$  as expected. However, for the first case the experimental  $d_{32}$  were lower than the target value but the polydispersities were correct. Although the experimental  $d_{32}$  for first target were lower, they maybe acceptable since the target size has been crossed. For the second case, both the schemes yield the desired  $d_{32}$  and polydispersity  $p.d.$ . From energy requirement standpoint, the best choice in both cases would be to operate more passes at lower pressure.

### 5.3 Conclusion

The previous version of the PBE model was improved upon to get better agreements with experimental data over a wide range of operating pressure as well as formulations by adding various features to the model. Substantial heating of the emulsion at the exit of the homogenizer suggested loss in mechanical energy available for drop disruption. Incorporating thermal losses improved model predictions to some extent. Adding the change in interfacial tension with successive passes and the effect of critical diameter further helped in proposed aim of improving predictions. Considerable improvements could be obtained on increasing the number of daughter droplets on top of the above effects and a final 62 % total reduction in the objective function value was obtained. Based on all the results, the most promising features to be included in the model were the maximum stable diameter and the number of daughter drops. To use all the features discussed, in addition to experimental drop size distribution data and physical properties of the constituent ingredients, we

need the temperature rise, the interfacial tension as a function of the concentration as well as the final pass  $d_{32}$ . However, this data once collected for one of the formulation holds true for other cases in the range considered. We also used our model to guide the design of some target emulsions. The design approach alongwith our model was found to be quite successful in being able to guide manufacturing of emulsions with target properties.

**Table 5.1.** Oil and surfactant concentrations

Oil concentration (wt%)	Surfactant concentration (wt%)
5	1
10	2
20	4

**Table 5.2.** Objective function values for 5 wt% oil and 1 wt% surfactant

Effect	Objective function $\Psi_T$	% improvement
Base case	4.46	-
Heating	3.89	13
Interfacial tension	3.68	17
Critical diameter	2.85	36
Daughter drops	1.69	62

**Table 5.3.** Design options

Pressure (bar)	#passes	$\epsilon$ (W/m <sup>3</sup> )
$d_{32}=0.5 \mu\text{m}$ , p.d.=2		
500	3.5	5.6e11
750	2.25	6.2e11
$d_{32}=0.25 \mu\text{m}$ , p.d.=2		
1000	2.75	1.1e12
1250	2.33	1.26e12

**Table 5.4.** Design strategy with experimental and model results

	Pressure (bar)	#passes	$d_{32}$ (expt)	p.d. (expt)	$d_{32}$ (model)	p.d. (model)
Target I: $d_{32}=0.5 \mu\text{m}$ , $p=2$						
Set I	500	3	0.29	2.0	0.47	2.0
	300	1				
Set II	750	2	0.3	2.1	0.45	2.24
	300	1				
Target II: $d_{32}=0.25 \mu\text{m}$ , $p=2$						
Set III	1000	2	0.23	1.91	0.25	1.86
	800	1				
Set IV	1250	2	0.25	2.12	0.27	2.27
	550	1				

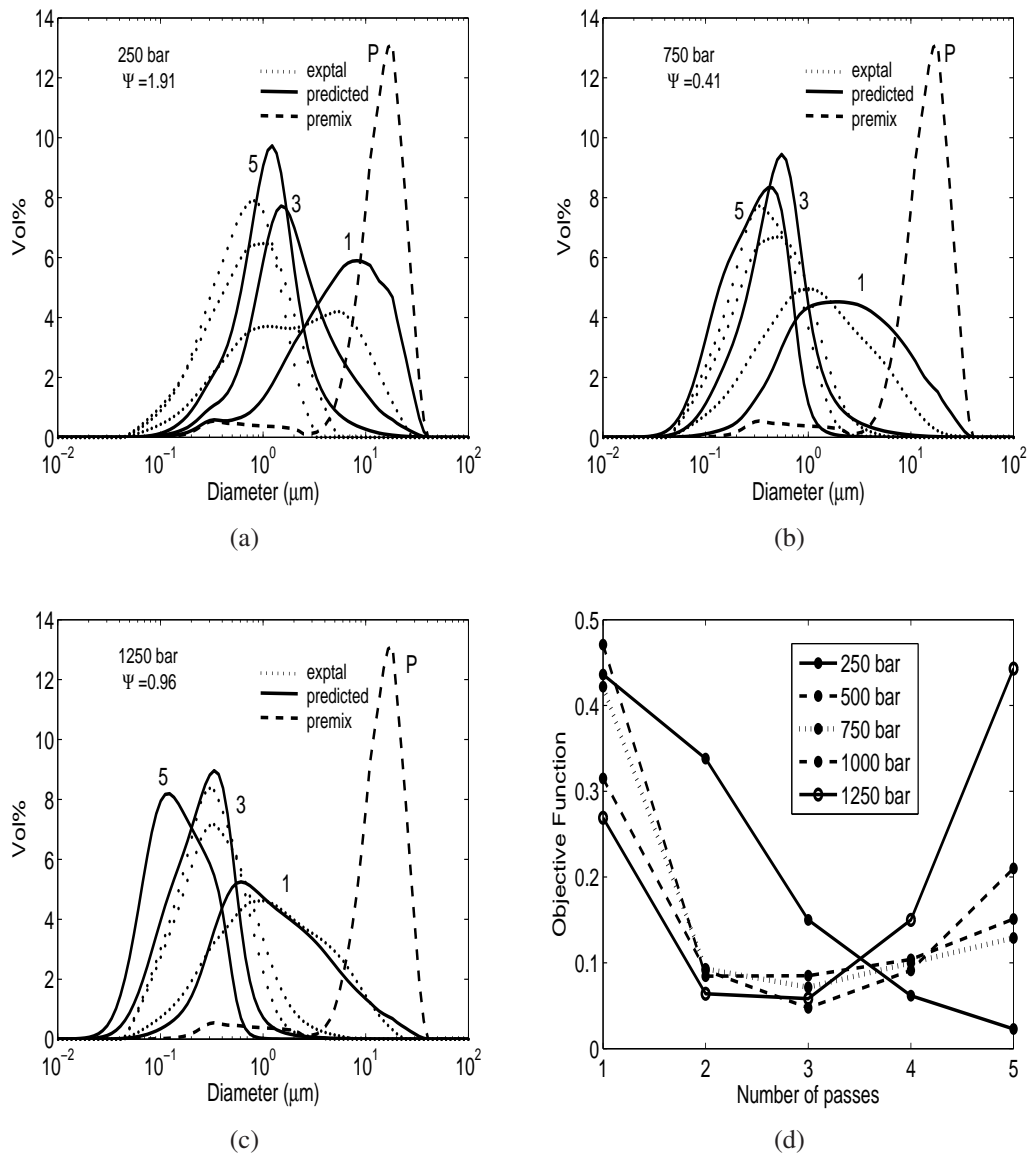


**Figure 5.1.** Base case parameter estimation for different pressures with experimental and predicted drop volume distributions for the (P) pre-mix, (1) the first pass, (3) the third pass, and (5) the fifth pass.  $\Psi$  is the objective function value for a particular pressure set. (a) 250 bar pressure set. (b) 750 bar pressure set. (c) 1250 bar pressure set. (d) Pass by pass objective function as a function of the number of passes for the different pressures.

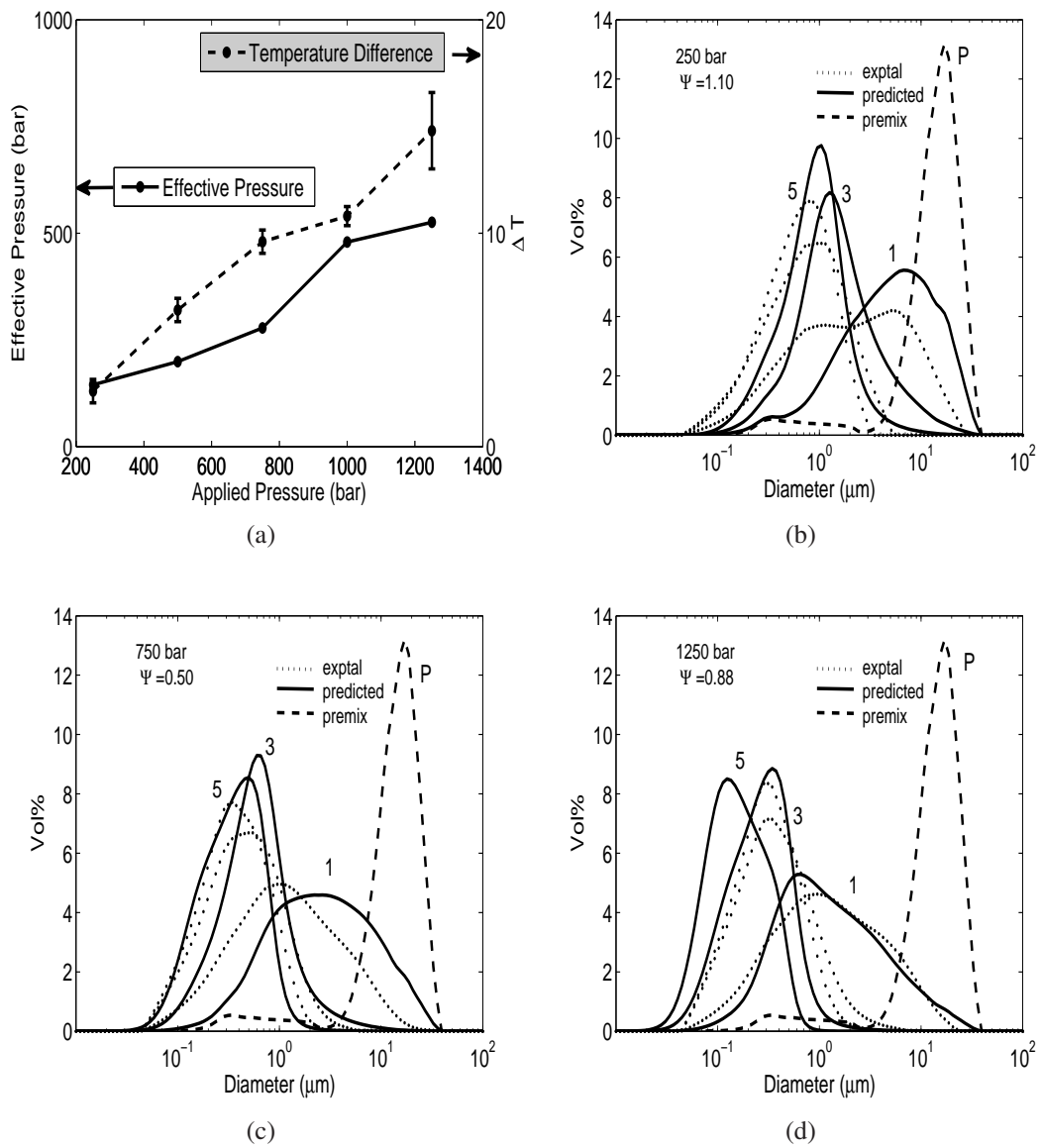
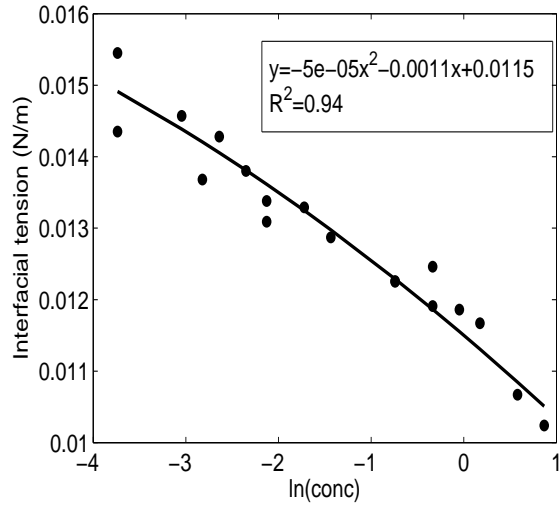
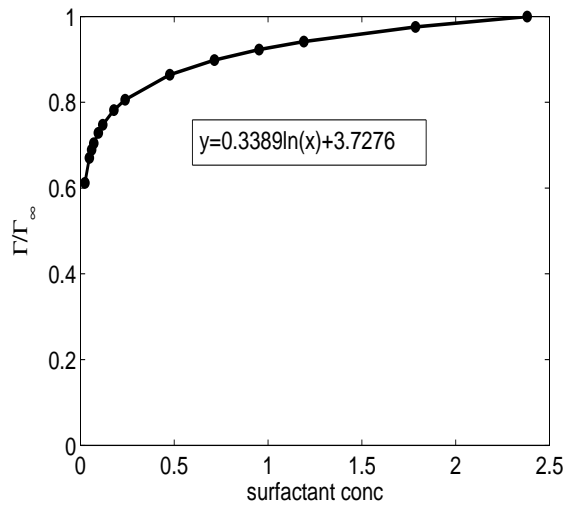


**Figure 5.2.** Effect of the inclusion of heating effects on parameter estimation for different pressures with experimental and predicted drop volume distributions. (a) Average temperature difference and the effective pressure as a function of the applied pressure with error bar representing the standard deviation. (b) 250 bar pressure set. (c) 750 bar pressure set. (d) 1250 bar pressure set.



(a)



(b)

**Figure 5.3.** Experimental data and model fits for interfacial tension. (a) Interfacial tension as a function of surfactant concentration with a fit to quadratic equation. (b)  $\Gamma/\Gamma_\infty$  as a function of concentration.

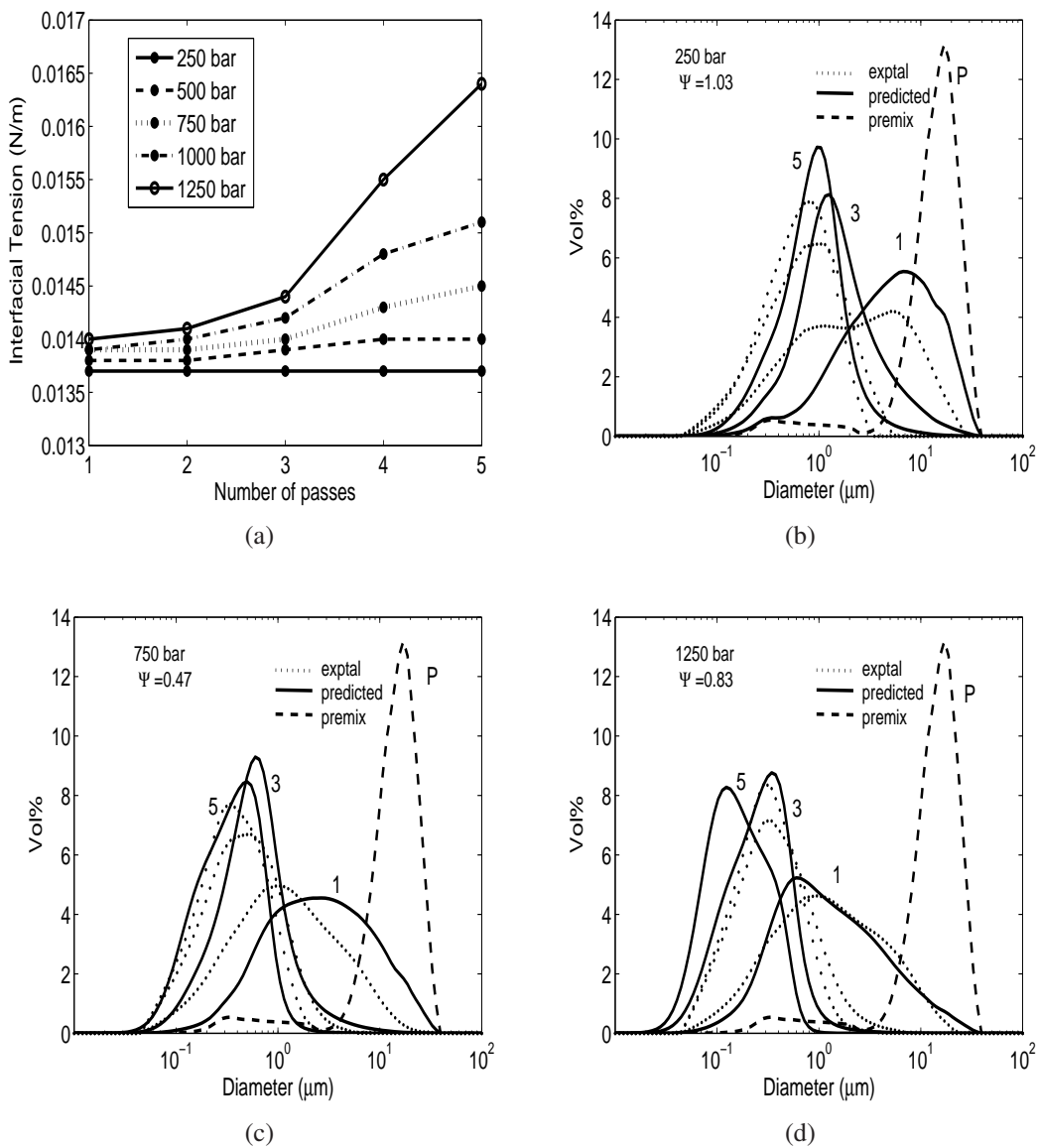


**Figure 5.4.** Effect of the inclusion of change in interfacial tension with passes on parameter estimation for different pressures with experimental and predicted drop volume distributions. (a) Interfacial tension as a function of the number of passes for different pressures. (b) 250 bar pressure set. (c) 750 bar pressure set. (d) 1250 bar pressure set.

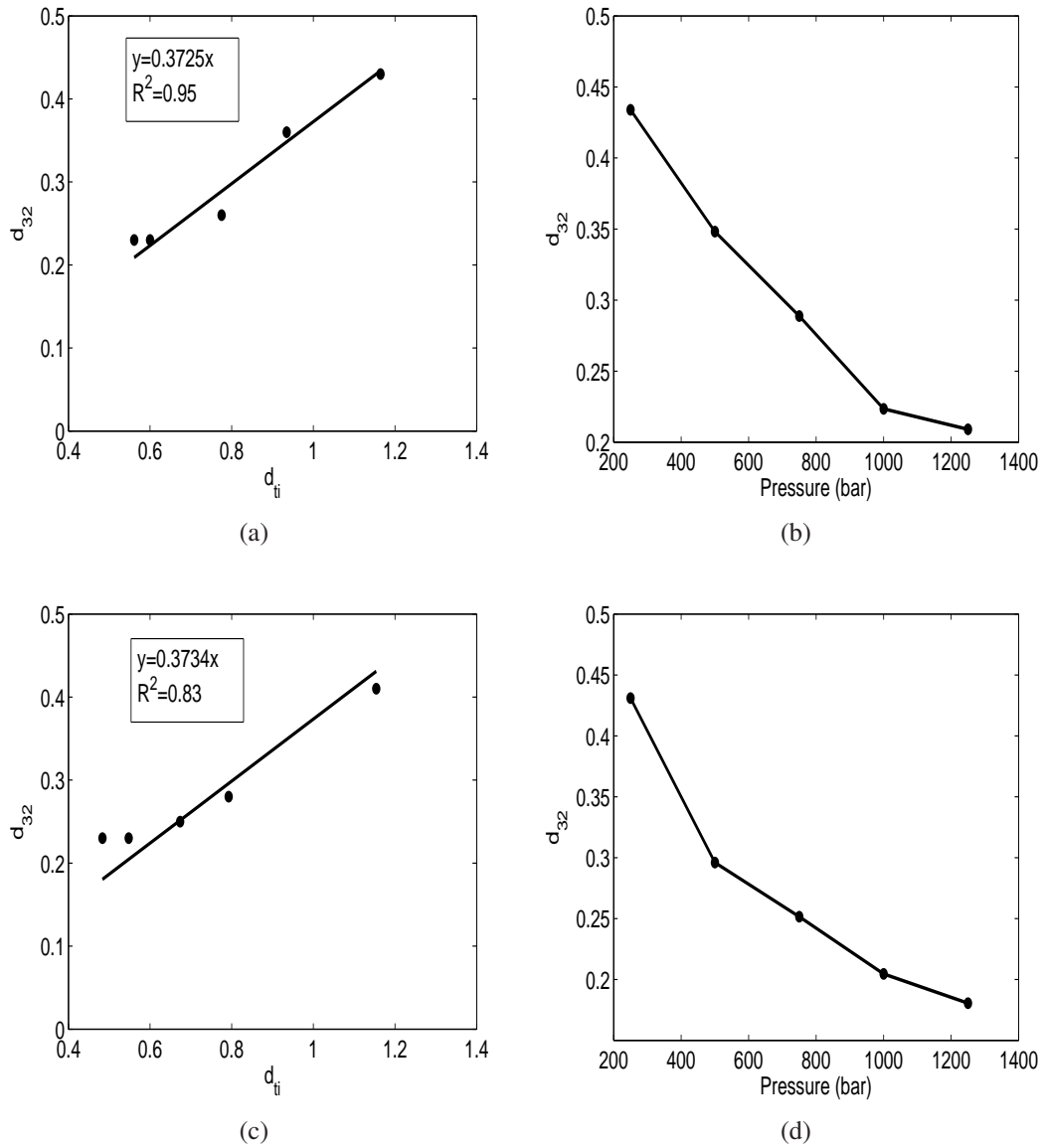


**Figure 5.5.** Critical diameter fits to experimental 5<sup>th</sup> pass  $d_{32}$ . (a) Mean diameter  $d_{32}$  with  $d_{ti}$  for 5wt% oil and 1wt% surfactant. (b) Mean diameter  $d_{32}$  with pressure for 5wt% oil and 1wt% surfactant. (c) Mean diameter  $d_{32}$  with  $d_{ti}$  for 10wt% oil and 2wt% surfactant. (d) Mean diameter  $d_{32}$  with pressure for 10wt% oil and 2wt% surfactant

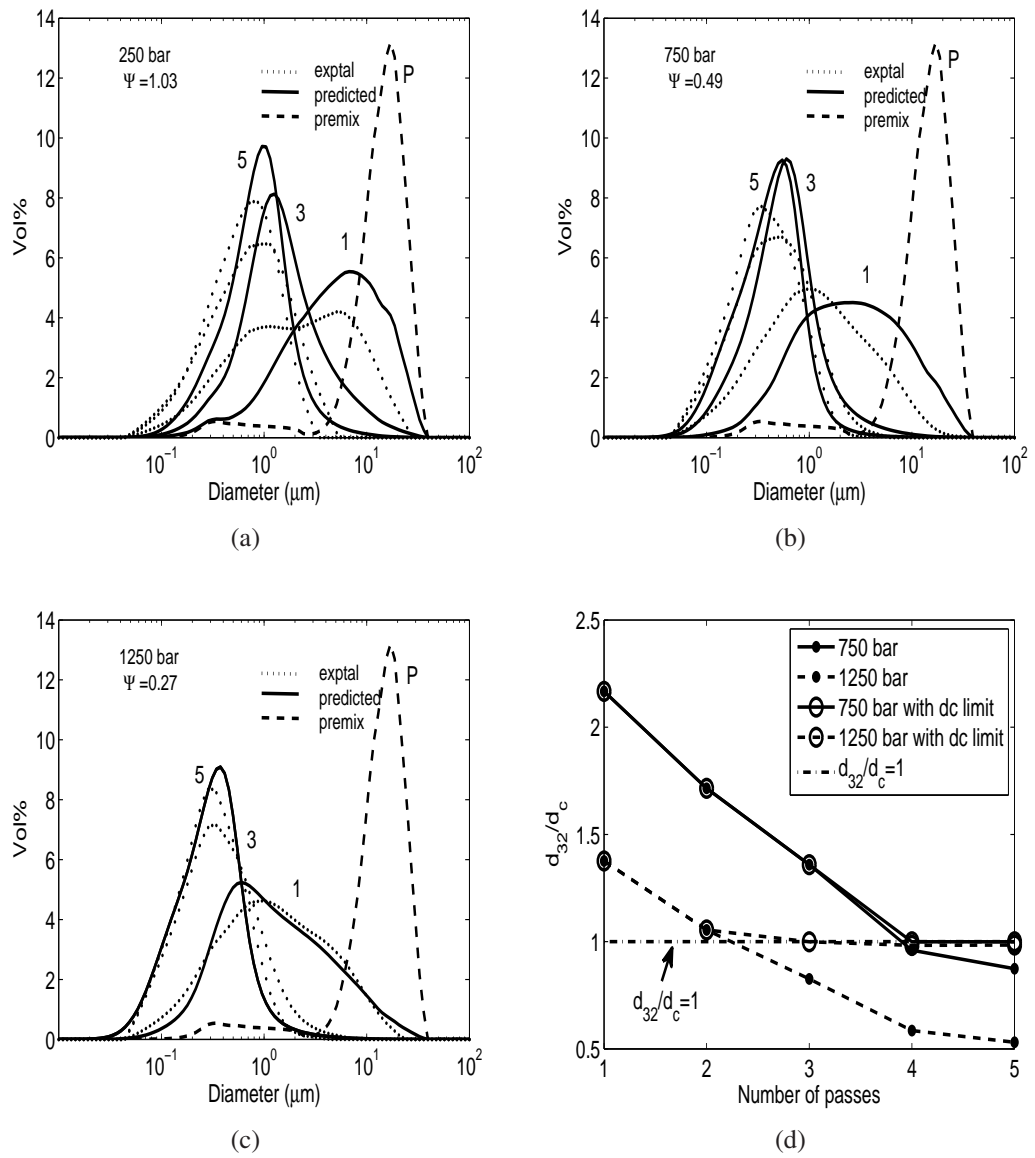


**Figure 5.6.** Effect of critical diameter limit on parameter estimation for different pressures with experimental and predicted drop volume distributions. (a) 250 bar pressure set. (b) 750 bar pressure set. (c) 1250 bar pressure set. (d) Diameter ratio versus number of passes for different pressures before and after inclusion of the critical diameter limit.

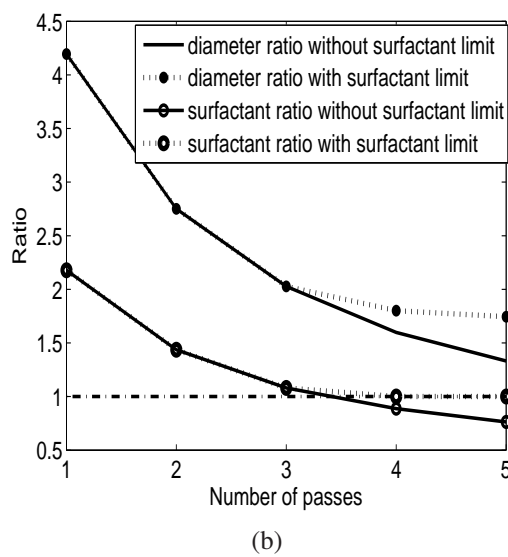
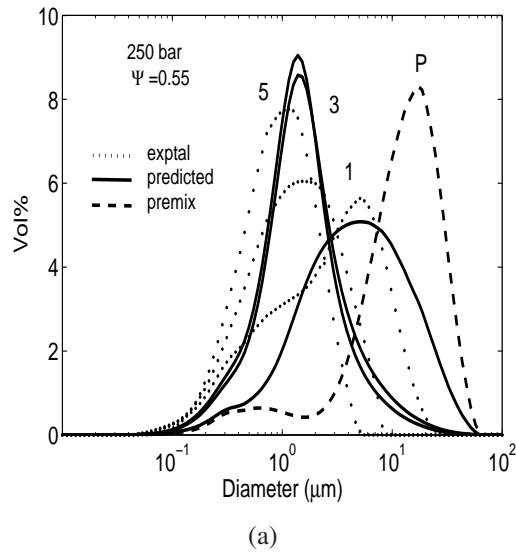


**Figure 5.7.** Effect of inclusion of the surfactant depletion limit. (a) 5 wt % oil and 1 wt % surfactant at 250 bar case with experimental data and model predictions. (b) Surfactant ratio and diameter ratio versus number of passes before and after inclusion of the surfactant limit.

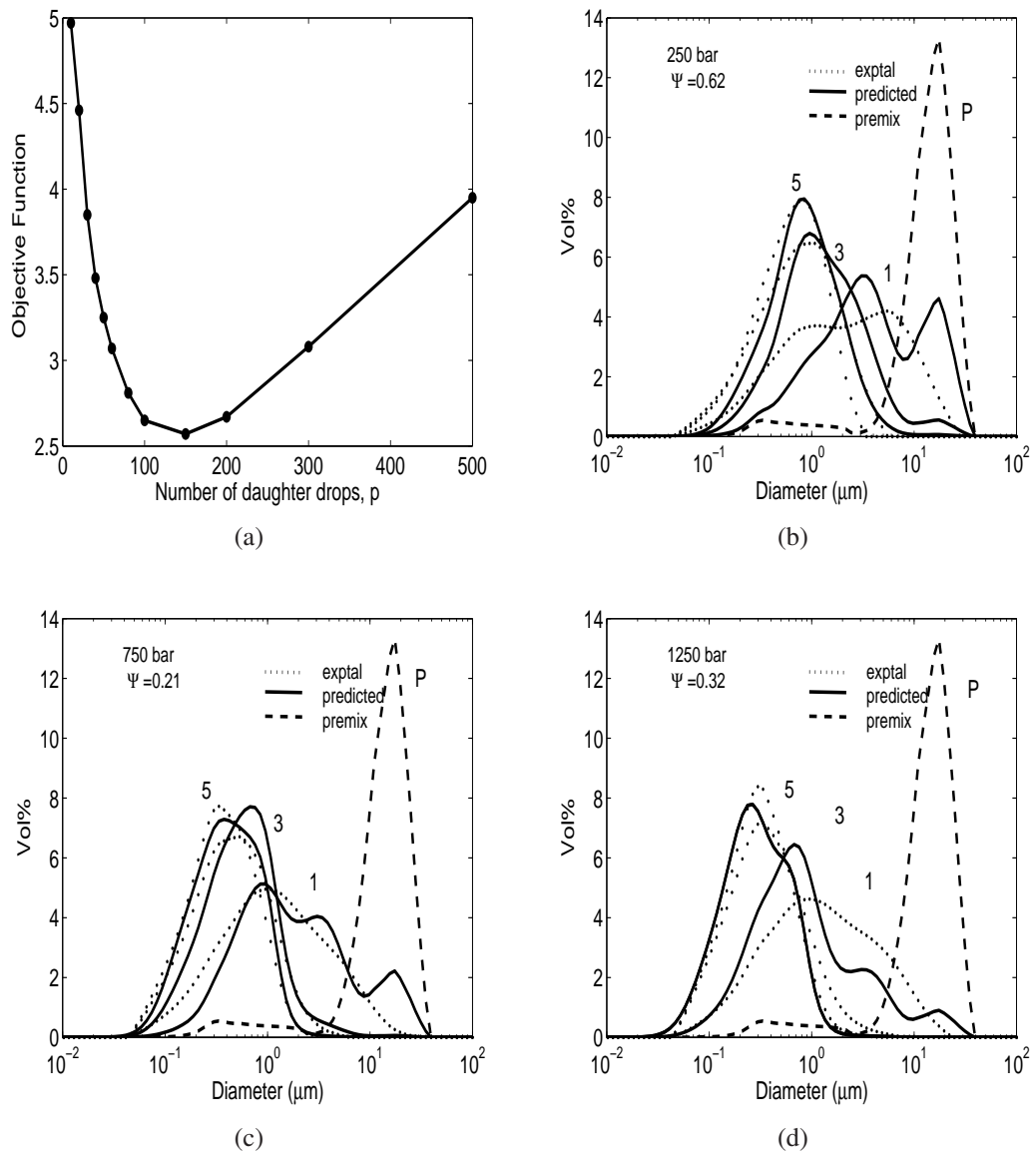
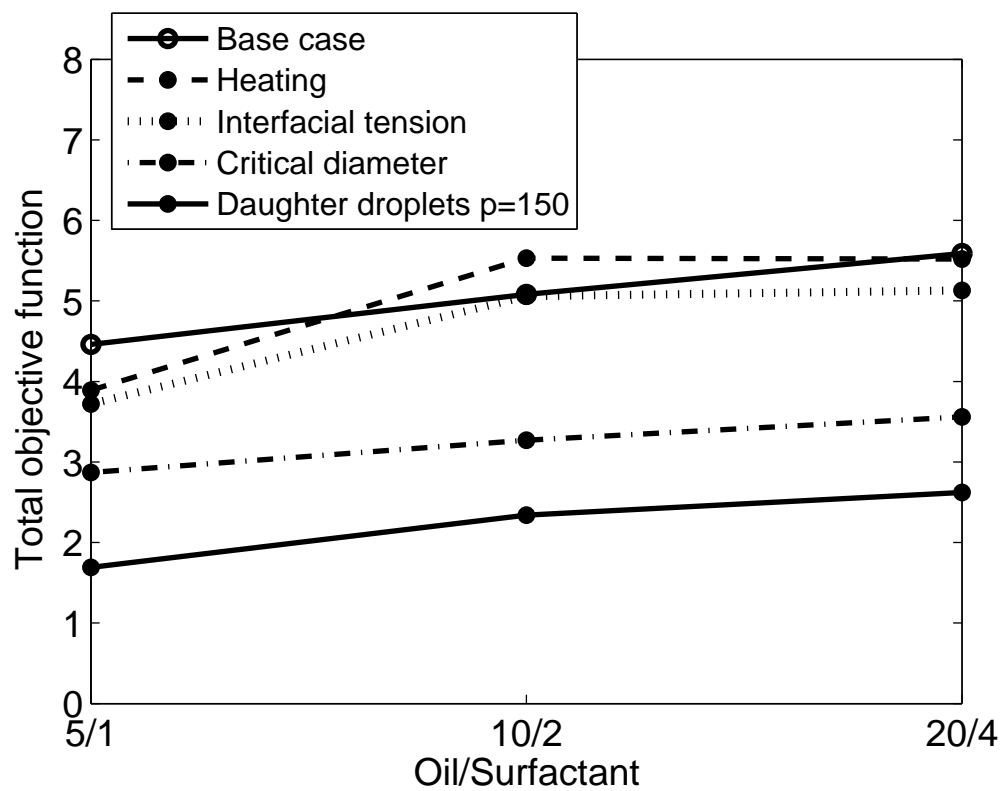


**Figure 5.8.** Effect of the number of daughter drops on parameter estimation for different pressures with experimental and predicted drop volume distributions. (a) Objective function value for different number of daughter drops. (b) 250 bar pressure set for  $p = 150$  and all the previously mentioned effects. (c) 750 bar pressure set for  $p = 150$  and all the previously mentioned effects. (d) 1250 bar pressure set for  $p = 150$  and all the previously mentioned effects.



(a)

**Figure 5.9.** Trends in Objective function for different formulations and the effect of different cases discussed. 3 different formulations as listed in table 5.1 were simulated using constants optimized for 5 wt% oil and 1 wt% surfactant.

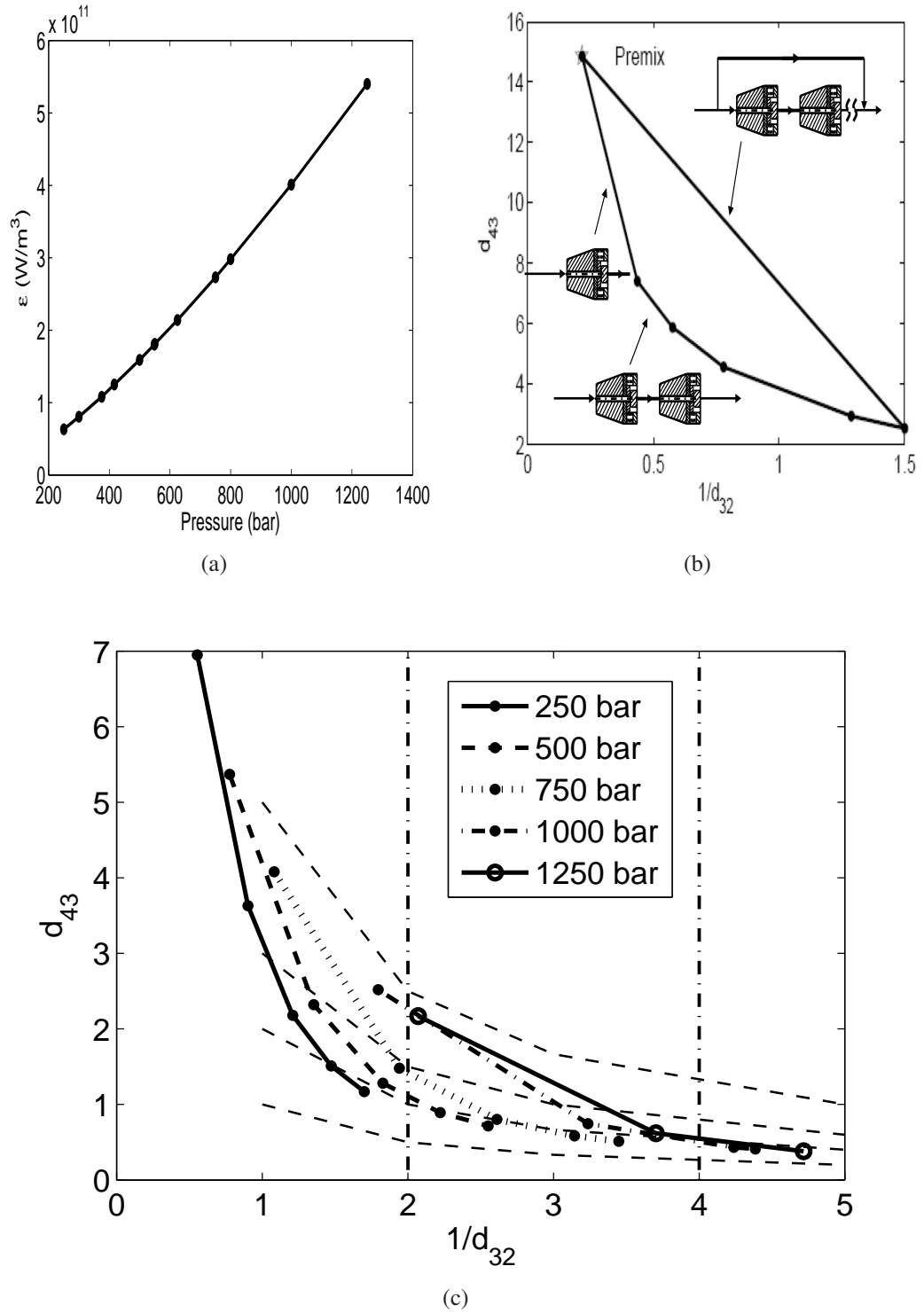


**Figure 5.10.** Design of target emulsions. (a) Energy dissipation rate as a function of pressure. (b) Attainable region of drops sizes at 250 bar pressure. (c) Attainable region of drops sizes for all pressures with lines of constant polydispersity and constant  $d_{32}$  as guides.

## **CHAPTER 6**

### **CONCLUSIONS AND FUTURE WORK**

#### **6.1 Summary**

We have developed a population balance equation based model for predicting the drop size distributions of emulsions resulting from a high pressure homogenization process. This work involved using appropriate mechanistic functions for the physical processes occurring in the homogenizer namely, breakage. Our focus was primarily on breakage and care was taken to keep coalescence to the minimum. We identified that two functions corresponding two breakage mechanisms under turbulent conditions were necessary for successful reproduction of the key features of the experimental drop size distribution. Starting with the assumption of binary breakup of drops, we improved the model by using multiple drop breakage which is a more common occurrence according to some experimental studies. Extensibility tests with the model were successful for changes in the formulation variables but were unsuccessful for changes in operating variable which is the pressure applied. The pressure predictions were improved upon by adding more features to the model like heating losses, changes in interfacial tension, critical diameter effect and number of daughter drops. Of these, the key features to be included were found to be the maximum stable diameter and number of daughter drops. The use of mechanistic functions allowed us to apply the model as a predictive tool under conditions not explored experimentally. An attempt was also made to validate the capability of the model as a design tool. Using the attainable region approach for design, we were able to successfully develop experimental plans for some example target emulsions.

## 6.2 Future Work

Our primary focus in this dissertation was developing a PBE model for emulsion breakage and identifying appropriate candidate functions for the same. Although coalescence was added to the model, it was not extensively explored. Moreover, we tried to maintain conditions where coalescence would not be significant, like using low dispersed phase volume fractions and plenty of surfactant which was verified by independent coalescence experiments. However for most practical applications, for instance mayonnaise, it is necessary to have a high dispersed phase fraction. It is therefore necessary to explore these high concentration systems using the PBE model. For this case, including coalescence is crucial since it is most likely to occur when the dispersed phase concentration is high. Surfactant effects are also significant under this scenario since in industrial situations material cost is a limiting factor and hence we cannot overload the system with surfactant to avoid coalescence.

We have probed changes in formulation variables to some extent but never changed the constituent ingredients. It is also important to explore different types of surfactant and dispersed phases. Depending on the choice of formulation ingredients, the physical properties will be different and will directly impact the breakage and coalescence processes in the homogenizer, ultimately affecting the final product. Emulsion systems in itself are worth exploring in detail and in addition the applicability of emulsions for delivery of active components should also be studied. Use of emulsions as delivery systems adds further complexity since their interactions with the formulation ingredients needs to be considered.

We also have not explored the effect of the homogenizing geometry in detail. A simplistic description introduced through the energy dissipation rate  $\epsilon$  was used. This in itself is not enough if we are interested in comparing different equipments or scaling them up. A detailed study is necessary and computational fluid dynamics can be probably used as a guide.

Many times from an application point of view, the final emulsion properties are more important and need to be modeled. For example, emulsion rheology is affected by the viscosity of the continuous phase, dispersed phase volume fraction, temperature, drop size distribution, and drop shape factor. Using physical property models, more tangible final properties like rheology, stability, and release rate of active ingredients can be predicted which however needs detailed study. Another applicability of the PBE model is for designing experiments to make emulsions with pre-specified properties. We did a preliminary investigation of the design methodology using the attainable region approach with reasonable success. We used mean properties of the distribution i.e. the  $d_{43}$  and  $d_{32}$  for this purpose and in Section 1.2 we have discussed what properties of emulsions are important. However, depending on the application it may be necessary to identify what key properties of these emulsions should be modeled and used for design. The design approach allows us to identify what combinations of process and formulation would give the target properties.

## APPENDIX A

### DERIVATION OF THE TURBULENT VISCOUS BREAKAGE RATE FUNCTION

The breakage rate is considered to be exponentially distributed as described by [119],

$$g(d) = \left(\frac{2}{\pi}\right)^{1/2} \frac{\Delta u}{d_i} \exp\left(\frac{-\Delta u_b^2}{\Delta u^2}\right) \quad (\text{A.1})$$

where  $\Delta u$  is the rms velocity difference across distance  $d_i$ , and  $\Delta u_b$  is the critical velocity difference at which drop breakage occurs. The local shear rate is approximated as:

$$G = \frac{\Delta u}{d_i} \quad (\text{A.2})$$

Substituting for  $\Delta u$  and  $\Delta u_b$  yields,

$$g(d) = \left(\frac{2}{\pi}\right)^{1/2} G \exp\left(\frac{-G_b^2}{G^2}\right) \quad (\text{A.3})$$

where  $G_b$  is the critical shear rate that causes drop breakup. The Capillary number ( $Ca$ ) for a drop of diameter  $d$  is given as,

$$Ca_d = \frac{\eta_c G d}{2\sigma} \quad (\text{A.4})$$

where  $\eta_c$  is the continuous phase viscosity, and  $\sigma$  is the interfacial tension. If  $Ca_d > Ca_c$  (the critical capillary number), the drop is unstable and will eventually break. The critical shear rate can be written in terms of the critical capillary number  $Ca_c$  as [23]:

$$G_b = \frac{2Ca_c\sigma}{\eta_c d} \quad (\text{A.5})$$

Therefore, the breakage rate can be written as:

$$g(d) = \left(\frac{2}{\pi}\right)^{1/2} G \exp\left(\frac{-(2Ca_c\sigma)^2}{(\eta_c G d)^2}\right) \quad (\text{A.6})$$

For turbulent flow,  $G$  can be related to energy dissipation rate  $\epsilon$  and the kinematic viscosity  $\nu$  [66, 119]. The resulting expression based on dispersed phase properties is:

$$G = \sqrt{\frac{\epsilon}{\nu}} = \sqrt{\frac{\epsilon\rho_d}{\eta_d}} \quad (\text{A.7})$$

Substituting for  $G$  in the breakage rate yields,

$$g(d) = \left(\frac{2}{\pi}\right)^{1/2} \left(\frac{\epsilon\rho_d}{\eta_d}\right)^{1/2} \exp\left(\frac{-(2Ca_c\sigma)^2\lambda}{(\eta_c d^2 \epsilon\rho_d)}\right) \quad (\text{A.8})$$

where  $\lambda = \eta_d/\eta_c$  is viscosity ratio. Expressing  $\epsilon$  in terms of pressure yields the final result:

$$\epsilon = \frac{c_1}{d} \left(\frac{P}{\rho_d}\right)^{3/2} \quad (\text{A.9})$$

$$g(v) = g_2(v) = K_3 \left(\frac{2}{\pi}\right)^{1/2} \left(\frac{P^{3/4}}{\eta_d^{1/2} \rho_d^{1/4} v^{1/6}}\right) \exp\left(\frac{-c_2(2Ca_c\sigma)^2\lambda}{\eta_c P^{3/2} \rho_d^{-1/2} v^{1/3}}\right) \quad (\text{A.10})$$

This function depends on the pressure  $P$ , interfacial tension  $\sigma$ , dispersed phase density  $\rho_d$ , continuous phase viscosity  $\eta_c$ , dispersed phase viscosity  $\eta_d$ , and the critical capillary number  $Ca_c$ . The critical capillary number is expected to depend on the viscosity ratio and the type of flow ([35, 48]). However, for turbulent viscous flows the dependence on the viscosity ratio is not strong. Therefore, we invoke the assumption that  $Ca_c$  is constant and incorporate  $Ca_c$  into the adjustable constant  $K_4$ .

$$g(v) = g_2(v) = K_3 \left(\frac{2}{\pi}\right)^{1/2} \left(\frac{P^{3/4}}{\eta_d^{1/2} \rho_d^{1/4} v^{1/6}}\right) \exp\left(\frac{-2K_4\sigma^2\lambda}{\eta_c P^{3/2} \rho_d^{-1/2} v^{1/3}}\right) \quad (\text{A.11})$$

## APPENDIX B

### MAXIMUM STABLE DROP SIZES

From turbulence theory, drops can break by collisions with turbulent eddies (function  $g_1$ ) or due to viscous stress (function  $g_2$ ). The size of the smallest eddy is given by [?, 68, 113, 116, 118]

$$\lambda_0 \approx \epsilon^{-1/4} \eta_c^{3/4} \rho_c^{-1/2} \quad (\text{B.1})$$

where  $\epsilon$  is the energy dissipation rate per unit volume of fluid. The maximum stable drop size in the inertial turbulent regime is given by

$$d_i \approx \sigma^{3/5} \epsilon^{-2/5} \rho_c^{-1/5} \quad (\text{B.2})$$

For the case of shear or viscous turbulent flow, the maximum stable drop diameter is

$$d_v \approx \sigma \epsilon^{-1/2} \eta_c^{-1/2} \quad (\text{B.3})$$

For our base case conditions  $d_v \approx \lambda_0 \approx d_i$ , which implies that both inertial and viscous forces are important [113].

The deformation time scale is given by [116, 118]

$$t_{def} \approx \frac{\eta_d}{C \rho_c^{1/3} \epsilon^{2/3} d^{2/3} - 4\sigma/d} \quad (\text{B.4})$$

The lifetime of the eddy is

$$t_{eddy} \approx \frac{\rho_c^{1/3} d^{2/3}}{\epsilon^{1/3}} \quad (\text{B.5})$$

Because the deformation time is smaller than eddy lifetime for most of the size range considered, drops can be broken by inertial forces and viscous forces. Therefore, either function could be used to describe breakage at small drop sizes. Because  $d_v$  was larger than  $d_i$ , we used the turbulent eddy function ( $g_1$ ) to describe breakup of small drops and turbulent shear function ( $g_2$ ) to describe breakup of large drops.

## APPENDIX C

### DERIVATION OF THE NO APPLIED PRESSURE BREAKAGE RATE FUNCTION

If the breakage rate is considered to be exponentially distributed [119],

$$g(d) = \left(\frac{2}{\pi}\right)^{1/2} \frac{\Delta u}{d_i} \exp\left(-\frac{\Delta u_b^2}{\Delta u^2}\right) \quad (\text{C.1})$$

$$G = \frac{\Delta u}{d_i} = \frac{u}{L} \quad (\text{C.2})$$

where  $u$  is the velocity in the homogenizer and  $L$  is the length over which the velocity changes. Rewriting this equation in terms of flowrate  $Q$ ,

$$G = \frac{Q}{AL} = \frac{Q}{V_d} \quad (\text{C.3})$$

where  $V_d$  is the dispersion volume or the effective volume over which the change occurs.

The breakage rate becomes,

$$g(d) = \left(\frac{2}{\pi}\right)^{1/2} G \exp\left(-\frac{G_b^2}{G^2}\right) \quad (\text{C.4})$$

where  $G_b$  is the critical shear rate. Expressing  $G_b$  in terms of the critical Capillary number  $Ca_c$ ,

$$G_b = \frac{2Ca_c\sigma}{\eta_c d} \quad (\text{C.5})$$

$$g(d) = \left(\frac{2}{\pi}\right)^{1/2} G \exp\left(-\left(\frac{2Ca_c\sigma}{\eta_c Gd}\right)^2\right) \quad (\text{C.6})$$

If  $G$  is expressed is rewritten using equation (C.3),

$$g(d) = \left(\frac{2}{\pi}\right)^{1/2} \frac{Q}{V_d} \exp\left(-\frac{(2Ca_c\sigma V_d)^2}{(\eta_c Q d)^2}\right) \quad (\text{C.7})$$

Converting the breakage rate to drop volume assuming spherical drops, the following equation is obtained,

$$g(v) = \left(\frac{2}{\pi}\right)^{1/2} \frac{Q}{V_d} \exp\left[-\left(\frac{2Ca_c\sigma V_d\pi^{1/3}}{\eta_c Q(6v)^{1/3}}\right)^2\right] \quad (\text{C.8})$$

The final equation is obtained by expressing unmeasurable quantities in terms of the adjustable parameters  $K_5$  and  $K_6$ ,

$$g(v) = K_5 \left(\frac{2}{\pi}\right)^{1/2} Q \exp\left[-\left(K_6 \frac{2Ca_c\sigma\pi^{1/3}}{\eta_c Q(6v)^{1/3}}\right)^2\right] \quad (\text{C.9})$$

## BIBLIOGRAPHY

- [1] Abramowitz, M, and Stegun, A. *Handbook of Mathematical Functions with Formulas, Graphs, and Mathematical Tables*. National Bureau of Standards. Applied Mathematics Series, 55, Washington D.C., 1964.
- [2] Alanazi, F., Fu, Z. F., and Lu, D. R. Effective transfection of rabies DNA vaccine in cell culture using an artificial lipoprotein carrier system. *Pharmaceutical Research* 21 (2004), 675–682.
- [3] Alopaeus, V., Koskinen, J., and Keskinen, K.I. Simulation of the population balances for liquid-liquid systems in a nonideal stirred tank. Part 1 Description and qualitative validation of the model. *Chemical Engineering Science* 54, 24 (1999), 5887–5899.
- [4] Alopaeus, V., Koskinen, J., and Keskinen, K.I. Utilization of population balances in simulation of liquid-liquid systems in mixed tanks. *Chemical Engineering Communications* 190, 11 (2003), 1468–1484.
- [5] Alopaeus, V., Koskinen, J., Keskinen, K.I., and Majander, J. Simulation of the population balances for liquid-liquid systems in a nonideal stirred tank. Part 2 - Parameter fitting and the use of the multiblock model for dense dispersions. *Chemical Engineering Science* 57, 10 (2002), 1815–1825.
- [6] Attama, A. A., Nzekwe, I. T., Nnamani, P. O., Adikwu, M. U., and Onugu, C. O. The use of solid self-emulsifying systems in the delivery of diclofenac. *Int. J. Pharmaceutics* 262 (2003), 23–28.
- [7] Austin, L., Shoji, K., Bhatia, V., Jindal, V., Savage, K., and Klimpel, R. Some results on description of size-reduction as a rate process in various mills. *Industrial & Engineering Chemistry Process Design And Development* 15, 1 (1976), 187 – 196.
- [8] Barut, K. D., Ari, F. F. C., and Oner, F. Development and characterization of a cationic emulsion formulation as a potential pDNA carrier system. *Turkish J. Chem.* 29 (2005), 27–40.
- [9] Becher, P. *Encyclopedia of Emulsion Technology, Vol I*. Marcel Dekker, New York, NY, 1983.
- [10] Becher, P. *Encyclopedia of Emulsion Technology, Vol II*. Marcel Dekker, New York, NY, 1983.
- [11] Becher, P. *Encyclopedia of Emulsion Technology, Vol III*. Marcel Dekker, New York, NY, 1983.

- [12] Becher, P. *Emulsions: Theory and Practice*. Oxford University Press, New York, NY, 2001.
- [13] Bivas-Benita, M., Oudshoorn, M., Romeijn, S., van Meijgaarden, K., Koerten, H., van der Meulen, H., Lambert, G., Ottenhoff, T., Benita, S., Junginger, H., and Borchard, G. Cationic submicron emulsions for pulmonary DNA immunization. *J. Controlled Release* 100 (2004), 145–155.
- [14] Bozkir, A., and Hayta, G. Preparation and evaluation of multiple emulsions water-in-oil-in-water (w/o/w) as delivery system for influenza virus antigens. *J. Drug Targeting* 12 (2004), 157–164.
- [15] Butz, N., Porte, C., Courrier, H., Krafft, M. P., and Vandamme, T. F. Reverse water-in-fluorocarbon emulsions for use in pressurized metered-dose inhalers containing hydrofluoroalkane propellants. *Int. J. Pharmaceutics* 238 (2002), 257–269.
- [16] Canu, P. Prediction of multimodal distributions in breakage processes. *Industrial & Engineering Chemistry Research* 44, 8 (2005), 2649 – 2658.
- [17] Cevc, G. Lipid vesicles and other colloids as drug carriers on the skin. *Adv. Drug Delivery Rev.* 56 (2004), 675–711.
- [18] Chen, Z., Pruss, J., and Warnecke, H.J. A population balance model for disperse systems: Drop size distribution in emulsion. *Chemical Engineering Science* 53, 5 (1998), 1059–1066.
- [19] Coualoglou, C.A., and Tavlarides, L.L. Description of interaction processes in agitated liquid-liquid dispersions. *Chemical Engineering Science* 32, 11 (1977), 1289–1297.
- [20] Courrier, H. M., Pons, F., Lessinger, J. M., Frossard, N., Krafft, M. P., and Vandamme, T. F. In vivo evaluation of a reverse water-in-fluorocarbon emulsion stabilized with a semifluorinated amphiphile as a drug delivery system through the pulmonary route. *Int. J. Pharmaceutics* 282 (2004), 131–140.
- [21] Cristini, V., Blawdziewicz, J., Loewenberg, M., and Collins, L. R. Breakup in stochastic Stokes flows: sub-Kolmogorov drops in isotropic turbulence. *J. Fluid Mechanics* 492 (2003), 231–250.
- [22] Cuellar, I., Bullon, J., Forgarini, A. M., Cardenas, A., and Briceno, M. I. More efficient preparation of parenteral emulsions or how to improve a pharmaceutical recipe by formulation engineering. *Chem. Engineering Science* 60 (2005), 2127–2134.
- [23] Dhingra, D. Feasible drop sizes in laminar emulsification systems. Master's thesis, University of Massachusetts Amherst, 2001.

- [24] Diemer, R.B., and Olson, J.H. A moment methodology for coagulation and breakage problems: Part 3 - generalized daughter distribution functions. *Chemical Engineering Science* 57, 19 (2002), 4187 – 4198.
- [25] Dorao, C.A., and Jakobsen, H.A. Numerical calculation of the moments of the population balance equation. *Journal Of Computational And Applied Mathematics* 196, 2 (2006), 619 – 633.
- [26] Fang, J. Y., Leu, Y. L., Chang, C. C., Lin, C. H., and Tsai, Y. H. Lipid nano/submicron emulsions as vehicles for topical flurbiprofen delivery. *Drug Delivery* 11 (2004), 97–105.
- [27] Flourey, J., Bellettre, J., Legrand, J., and Desrumaux, A. Analysis of a new type of high pressure homogeniser: A study of the flow pattern. *Chemical Engineering Science* 59, 4 (2004), 843–853.
- [28] Flourey, J., Legrand, J., and Desrumaux, A. Analysis of a new type of high pressure homogeniser: Part B: Study of droplet break-up and re-coalescence phenomena. *Chemical Engineering Science* 59, 6 (2004), 1285–1294.
- [29] Fourer, R., Gay, D. M., and Kernighan, B. W. *AMPL: A Modeling Language for Mathematical Programming*. Brooks/Cole Publishing Company, Pacific Grove, CA, 2003.
- [30] Friedman D.I., Schwarz J.S., and M., Weisspapir. Submicron emulsion vehicle for enhanced transdermal delivery of steroidal and nonsteroidal antiinflammatory drugs. *J. Pharmaceutical Sciences* 84 (1995), 324–329.
- [31] Garcia, J. A. Robust design for structured products. Master's thesis, University of Massachusetts Amherst, 2004.
- [32] Gavi, E., Marchisio, D.L., and Barresi, A.A. On the importance of mixing for the production of nanoparticles. *Journal Of Dispersion Science And Technology* 29, 4 (2008), 548 – 554.
- [33] Gershanik, T., and Benita, S. Self-dispersing lipid formulations for improving oral absorption of lipophilic drugs. *European J. Pharmaceutics Biopharmaceutics* 50 (2000), 179–188.
- [34] Guide, Fluent Users. , *Version 6.2*. Fluent Inc, Lebanon, NH, 2005.
- [35] Gupta, S. Structured liquid products: Emulsification process design for viscoelastic liquids. Master's thesis, University of Massachusetts Amherst, 2004.
- [36] Gursoy, R. N., and Benita, S. Self-emulsifying drug delivery systems (SEDDS) for improved oral delivery of lipophilic drugs. *Biomedicine & Pharmacotherapy* 58 (2004), 173–182.

- [37] Hakansson, A., Tragardh, C., and Bergenstahl, B. Dynamic simulation of emulsion formation in a high pressure homogenizer. *Chemical Engineering Science* 64, 12 (2009), 2915 – 2925.
- [38] Hakansson, A., Tragardh, C., and Bergenstahl, B. Studying the effects of adsorption, recoalescence and fragmentation in a high pressure homogenizer using a dynamic simulation model. *Food Hydrocolloids* 23, 4 (2009), 1177–1183.
- [39] He, L., Wang, G. L., and Zhang, Q. An alternative paclitaxel microemulsion formulation: hypersensitivity evaluation and pharmacokinetic profile. *Int. J. Pharmaceutics* 250 (2004), 45–50.
- [40] Hill, P.J., and Ng, K.M. Statistics of multiple particle breakage. *AIChE Journal* 42, 6 (1996), 1600 – 1611.
- [41] Hinze, J. O. Fundamentals of the hydrodynamic mechanism of splitting in dispersion processes. *Aiche Journal* 1 (1955), 289–295.
- [42] Hung, C. F., Hwang, T. L., Chang, C. C., and Fang, J. Y. Physicochemical characterization and gene transfection efficiency of lipid emulsions with various co-emulsifiers. *Int. J. Pharmaceutics* 289 (2005), 197–208.
- [43] Jaworski, Z., Pianko-Oprych, P., Marchisio, D.L., and Nienow, A.W. CFD modelling of turbulent drop breakage in a kenics static mixer and comparison with experimental data. *Chemical Engineering Research & Design* 85 (2007), 753 – 759.
- [44] Kang, B. K., Chon, S. K., Kim, S. H., Jeong, S. Y., Kim, M. S., Cho, S. H., Lee, H. B., and Khang, G. Controlled release of paclitaxel from microemulsion containing PLGA and evaluation of anti-tumor activity in vitro and in vivo. *Int. J. Pharmaceutics* 286 (2004), 147–156.
- [45] Kelly, W.J., and Muske, K.R. Optimal operation of high-pressure homogenization for intracellular product recovery. *Bioprocess And Biosystems Engineering* 27, 1 (2004), 25–37.
- [46] Kim, J., and Kramer, T.A. Improved orthokinetic coagulation model for fractal colloids: Aggregation and breakup. *Chemical Engineering Science* 61, 1 (2006), 45 – 53.
- [47] Kim, T. W., Chung, H. S., Kwon, I. C., Sung, H. C., Shin, B. C., and Jeong, S. Y. Airway gene transfer using cationic emulsion as a mucosal gene carrier. *J. Gene Medicine* 7 (2005), 749–758.
- [48] Koper, G. J. M. *An introduction to Interfacial Engineering*. VSSD, Leeghwaterstraat, Delft, Netherlands, 2007.
- [49] Kostoglou, M., Dovas, S., and Karabelas, A.J. On steady - state size distribution of dispersions in breakage process. *Chemical Engineering Science* 52, 8 (1997), 1285–1299.

- [50] Kostoglou, M., and Karabelas, A.J. Toward a unified framework for the derivation of breakage functions based on the statistical theory of turbulence. *Chemical Engineering Science* 60, 23 (2005), 6584 – 6595.
- [51] Krafft, M. P., Chittofrati, A., and Riess, J. G. Emulsions and microemulsions with a fluorocarbon phase. *Current Opinion In Colloid & Interface Science* 8 (2003), 251–258.
- [52] Kumar, S., and Ramkrishna, D. On the solution of population balance equations by discretization 1. A fixed pivot technique. *Chemical Engineering Science* 51, 8 (1996), 1311–1332.
- [53] Kumar, S., and Ramkrishna, D. On the solution of population balance equations by discretization 2. A moving pivot technique. *Chemical Engineering Science* 51, 8 (1996), 1333–1342.
- [54] Lallemand, F., Felt-Baeyens, O., Besseghir, K., Behar-Cohen, F., and Gurny, R. Cyclosporine A delivery to the eye: A pharmaceutical challenge. *European J. Pharmaceutics Biopharmaceutics* 56 (2003), 307–318.
- [55] Lallemand, F., Furrer, P., Felt-Baeyens, O., Gex-Fabry, M., Dumont, J. M., Besseghir, K., and Gurny, R. A novel water-soluble cyclosporine A prodrug: Ocular tolerance and in vivo kinetics. *Int. J. Pharmaceutics* 295 (2005), 7–14.
- [56] Lallemand, F., Perottet, P., Felt-Baeyens, O., Kloeti, W., Philippoz, F., Marfurt, J., Besseghir, K., and Gurny, R. A water-soluble prodrug of cyclosporine A for ocular application: A stability study. *European J. Pharmaceutical Sciences* 26 (2005), 124–129.
- [57] Lander, R, Manger, W, Scouloudis, M, Ku, A, Davis, C, and Lee, A. Gaulin homogenization: A mechanistic study. *Biotechnology Progress* 16, 1 (2000), 80 – 85.
- [58] Lanza, G. M., and Wickline, S. A. Targeted ultrasonic contrast agents for molecular imaging and therapy. *Current Problems In Cardiology* 28 (2003), 625–653.
- [59] Lee, J., Lee, Y., Kim, J., Yoon, M., and Choi, Y. W. Formulation of microemulsion systems for transdermal delivery of aceclofenac. *Archives Pharmacal Research* 28 (2005), 1097–1102.
- [60] Lowe, K. C. Perfluorinated blood substitutes and artificial oxygen carriers. *Blood Rev.* 13 (1999), 171–184.
- [61] Lowe, K. C. Engineering blood: Synthetic substitutes from fluorinated compounds. *Tissue Engineering* 9 (2003), 389–399.
- [62] Lowe, K. C., and Ferguson, E. Benefit and risk perceptions in transfusion medicine: blood and blood substitutes. *J. Internal Medicine* 253 (2003), 498–507.

- [63] Maguire, L.A., Zhang, H., and Shamlou, P.A. Preparation of small unilamellar vesicles (SUV) and biophysical characterization of their complexes with poly-L-lysine-condensed plasmid DNA. *Biotechnology And Applied Biochemistry* 37 (2003), 73–81.
- [64] Mahoney, A.W., Doyle, F.J., and Ramkrishna, D. Inverse problems in population balances: Growth and nucleation from dynamic data. *AIChE Journal* 48, 5 (2002), 981–990.
- [65] Malmsten, M. *Surfactants and Polymers in Drug Delivery*. Marcel Dekker, Inc., New York, 2002.
- [66] Marchisio, D.L., Soos, M., Sefcik, J., and Morbidelli, M. Role of turbulent shear rate distribution in aggregation and breakage processes. *AIChE Journal* 52, 1 (2006), 158–173.
- [67] Marti-Mestres, G., and Nielloud, F. Emulsions in health care applications - An overview. *J. Dispersion Science Technology* 23 (2002), 419–439.
- [68] McClements, D. J. *Food Emulsions : Principles, Practice, and Techniques*. CRC Press, Boca Raton, FL, 2005.
- [69] Miller, J., Rogowski, M., and Kelly, W. Using a CFD model to understand the fluid dynamics promoting e-coli breakage in a high-pressure homogenizer. *Biotechnology Progress* 18, 5 (2002), 1060 – 1067.
- [70] Muller-Goymann, C. C. Physicochemical characterization of colloidal drug delivery systems such as reverse micelles, vesicles, liquid crystals and nanoparticles for topical administration. *European J. Pharmaceutics Biopharmaceutics* 58 (2004), 343–356.
- [71] Narsimhan, G., Nejfelt, G., and Ramkrishna, D. Breakage functions for droplets in agitated liquid-liquid dispersions. *AIChE Journal* 30, 3 (1984), 457–467.
- [72] Narsimhan, G., Ramkrishna, D., and Gupta, J.P. Analysis of drop size distributions in lean liquid-liquid dispersions. *AIChE Journal* 26, 6 (1980), 991–1000.
- [73] Nasr-El-Din, H. A. *Fluid Dynamics in Oil-Water-Sand Systems in Emulsions: Fundamentals and Applications in the Petroleum Industry*. American Chemical Society, Washington, DC, 1992.
- [74] Nicolaos, G., Crauste-Manciet, S., Farinotti, R., and Brossard, D. Improvement of cefpodoxime proxetil oral absorption in rats by an oil-in-water submicron emulsion. *Int. J. Pharmaceutics* 263 (2003), 165–171.
- [75] Nielloud, Françoise, and Marti-Mestres, Gilberte. *Pharmaceutical Emulsions and Suspensions*. Marcel Dekker, Inc., New York, NY, 2000.

- [76] Pan, G. L., Shower, M., Oie, S., and Lu, D. R. In vitro gene transfection in human glioma cells using a novel and less cytotoxic artificial lipoprotein delivery system. *Pharmaceutical Research* 20 (2003), 738–744.
- [77] Phipps, L.W. Fragmentation of oil drops in emulsions by a high-pressure homogenizer. *Journal Of Physics D-Applied Physics* 8, 4 (1975), 448 – 462.
- [78] Piemi, M. P. Y., Korner, D., Benita, S., and Marty, J. P. Positively and negatively charged submicron emulsions for enhanced topical delivery of antifungal drugs. *J. Controlled Release* 58 (1999), 177–187.
- [79] Rabinovich-Guilatt, L., Couvreur, P., Lambert, G., and Dubernet, C. Cationic vectors in ocular drug delivery. *J. Drug Targeting* 12 (2004), 623–633.
- [80] Raikar, N.B., Bhatia, S.R., Malone, M.F., Almeida-Rivera, C., Bongers, P., McClements, D.J., and Henson, M.A. Prediction of emulsion drop size distributions with population balance equation models of multiple drop breakage. *Accepted in Colloids and Surfaces A: Physicochemical and Engineering Aspects* (2010).
- [81] Raikar, N.B., Bhatia, S.R., Malone, M.F., and Henson, M.A. Experimental studies and population balance equation models for breakage prediction of emulsion drop size distributions. *Chemical Engineering Science* 64, 10 (2009), 2433–2447.
- [82] Rallison, J.M. The deformation of small viscous drops and bubbles in shear flows. *Annual Review Of Fluid Mechanics* 16 (1984), 45 – 66.
- [83] Ramkrishna, D. Drop-breakage in agitated liquid-liquid dispersions. *Chemical Engineering Science* 29, 4 (1974), 987–992.
- [84] Ramkrishna, D. *Population Balances: Theory and Applications to Particulate Processes in Engineering*. Academic Press, New York, NY, 2000.
- [85] Ramkrishna, D., and Mahoney, A.W. Population balance modeling: Promise for the future. *Chemical Engineering Science* 57, 4 (2002), 595–606.
- [86] Ramkrishna, D., Sathyagal, A., and Narsimhan, G. Analysis of dispersed-phase systems - fresh perspective. *AIChE Journal* 41, 1 (1995), 35–44.
- [87] Riess, J. G. Blood substitutes and other potential biomedical applications of fluorinated colloids. *J. Fluorine Chem.* 114 (2002), 119–126.
- [88] Riess, J. G. Understanding the fundamentals of perfluorocarbons and perfluorocarbon emulsions relevant to in vivo oxygen delivery. *Artificial Cells Blood Substitutes Biotechnology* 33 (2005), 47–63.
- [89] Riess, J. G., and Krafft, M. P. Fluorinated materials for in vivo oxygen transport (blood substitutes), diagnosis and drug delivery. *Biomaterials* 19 (1998), 1529–1539.

- [90] Rimmer, D. P., Gregoli, A. A., Hamshar, J. A., and Yildirim, E. *Pipeline Emulsion Transportation for Heavy Oils, in Emulsions: Fundamentals and Applications in the Petroleum Industry*. American Chemical Society, Washington, DC, 1992.
- [91] Ruiz, M.C., Lermenda, P., and Padilla, R. Drop size distribution in a batch mixer under breakage conditions. *Hydrometallurgy* 63, 1 (2002), 65–74.
- [92] Ruiz, M.C., and Padilla, R. Analysis of breakage functions for liquid-liquid dispersions. *Hydrometallurgy* 72, 3-4 (2004), 245 – 258.
- [93] Saettone, M. F., Giannaccini, B., and Monti, D. Ophthalmic emulsions and suspensions (Reprinted from *Pharmaceutical Emulsions and Suspensions*, pg 303-322, 2000). *J. Toxicology-cutaneous Ocular Toxicology* 20 (2001), 183–201.
- [94] Saniere, A., Henaut, I., and Argillier, J.F. Pipeline transportation of heavy oils, a strategic, economic and technological challenge. *Oil And Gas Science And Technology-Revue De L Institut Francais Du Petrole* 59, 5 (2004), 455 – 466.
- [95] Sathyagal, A.N., and Ramkrishna, D. Droplet breakage in stirred dispersions: Breakage functions from experimental drop-size distributions. *Chemical Engineering Science* 51, 9 (1996), 1377–1391.
- [96] Sathyagal, A.N., Ramkrishna, D., and Narsimhan, G. Solution of inverse problems in population balances 2: Particle break-up. *Computers and Chemical Engineering* 19, 4 (1995), 437–451.
- [97] Schmitz, K. S. *Dynamic Light Scattering by Macromolecules*. Academic Press, Inc., San Diego, 1990.
- [98] Schramm, L. L. *Petroleum Emulsions: Basic Principles in Emulsions: Fundamentals and Applications in the Petroleum Industry*. American Chemical Society, Washington, DC, 1992.
- [99] Simon, M., Schmidt, S.A., and Bart, H.J. The droplet population balance model - Estimation of breakage and coalescence. *Chemical Engineering & Technology* 26, 7 (2003), 745–750.
- [100] Solans, C., Izquierdo, P., Nolla, J., Azemar, N., and Garcia-Celma, M. J. Nanoemulsions. *Current Opinion In Colloid & Interface Science* 10 (2005), 102–110.
- [101] Soon, S.Y., Harbidge, J., Titchener-Hooker, N.J., and Shamlou, P.A. Prediction of drop breakage in an ultra high velocity jet homogenizer. *Journal of Chemical Engineering of Japan* 34, 5 (2001), 640–646.
- [102] Sovova, H. Breakage and coalescence of drops in a batch stirred vessel .2. Comparison of model and experiments. *Chemical Engineering Science* 36, 9 (1981), 1567–1573.

- [103] Sovova, H, and Prochazka, J. Breakage and coalescence of drops in a batch stirred vessel .1. Comparison of continuous and discrete models. *Chemical Engineering Science* 36, 1 (1981), 163–171.
- [104] Spahn, D. R. Current status of artificial oxygen carriers. *Adv. Drug Delivery Rev.* 40 (2000), 143–151.
- [105] Stone, H.A. Dynamics of drop deformation and breakup in viscous fluids. *Annual Review Of Fluid Mechanics* 26 (1994), 65 – 102.
- [106] Tamilvanan, S. Oil-in-water lipid emulsions: implications for parenteral and ocular delivering systems. *Progress In Lipid Research* 43 (2004), 489–533.
- [107] Tamilvanan, S., and Benita, S. The potential of lipid emulsion for ocular delivery of lipophilic drugs. *European J. Pharmaceutics Biopharmaceutics* 58 (2004), 357–368.
- [108] Taylor, G. I. The formation of emulsions in definable fields of flow. *Proc. Royal Soc. London Series A-mathematical Phys. Sciences* 146 (1934), 0501–0523.
- [109] Tcholakova, S., Vankova, N., Denkov, N.D., and Danner, T. Emulsification in turbulent flow: 3. Daughter drop-size distribution. *Journal of Colloid and Interface Science* 310, 2 (2007), 570 – 589.
- [110] Valentas, K. J., and Amundson, N. R. Breakage and coalescence in dispersed phase systems. *Industrial & Engineering Chem. Fundamentals* 5 (1966), 533–&.
- [111] Valentas, K. J., and Amundson, N. R. Influence of droplet size-age distribution on rate processes in dispersed-phase systems. *Industrial & Engineering Chem. Fundamentals* 7 (1968), 66–&.
- [112] Valentas, K. J., Bilous, O., and Amundson, N. R. Analysis of breakage in dispersed phase systems. *Industrial & Engineering Chem. Fundamentals* 5 (1966), 271–&.
- [113] Vankova, N., Tcholakova, S., Denkov, N.D., Ivanov, I.B., Vulchev, V.D., and Danner, T. Emulsification in turbulent flow - 1. Mean and maximum drop diameters in inertial and viscous regimes. *Journal of Colloid and Interface Science* 312, 2 (2007), 363 – 380.
- [114] Vankova, N., Tcholakova, S., Denkov, N.D., Vulchev, V.D., and Danner, T. Emulsification in turbulent flow 2. Breakage rate constants. *Journal of Colloid and Interface Science* 313, 2 (2007), 612 – 629.
- [115] Vigil, R.D., and Ziff, R.M. On the stability of coagulation fragmentation population balances. *Journal Of Colloid And Interface Science* 133, 1 (1989), 257 – 264.
- [116] Walstra, P. Principles of emulsion formation. *Chemical Engineering Science* 48, 2 (1993), 333–349.
- [117] Walstra, P. *Physical Chemistry of Foods*. Marcel Dekker, New York, NY, 2003.

- [118] Walstra, P. *Emulsions*. In: J. Lyklema (Ed.), *Fundamentals of interface and colloid science: Soft colloids*. Elsevier, Academic Press, London, 2005.
- [119] Wang, L., Marchisio, D.L., Vigil, R.D., and Fox, R.O. CFD simulation of aggregation and breakage processes in laminar Taylor-Couette flow. *Journal of Colloid and Interface Science* 282, 2 (2005), 380 – 396.
- [120] Wei, L. L., Sun, P. N., Nie, S. F., and Pan, W. S. Preparation and evaluation of SEDDS and SMEDDS containing carvedilol. *Drug Development Industrial Pharmacy* 31 (2005), 785–794.
- [121] Woo, X.Y., Tan, R.B.H., Chow, P.S., and Braatz, R.D. Simulation of mixing effects in antisolvent crystallization using a coupled CFD-PDF-PBE approach. *Crystal Growth & Design* 6, 6 (2006), 1291 – 1303.
- [122] Wright, H., and Ramkrishna, D. Solutions of inverse problems in population balances 1: Aggregation kinetics. *Computers & Chemical Engineering* 16, 12 (1992), 1019–1038.
- [123] Yaghi, B.M., and Al-Bemani, A. Heavy crude oil viscosity reduction for pipeline transportation. *Energy Sources* 24, 2 (2002), 93 – 102.
- [124] Yamaguchi, M., Yasueda, S., Isowaki, A., Yamamoto, M., Kimura, M., Inada, K., and Ohtori, A. Formulation of an ophthalmic lipid emulsion containing an anti-inflammatory steroidal drug, difluprednate. *Int. J. Pharmaceutics* 301 (2005), 121–128.
- [125] Zaccone, A., Gabler, A., Maass, S., Marchisio, D., and Kraume, M. Drop breakage in liquid-liquid stirred dispersions: Modelling of single drop breakage. *Chemical Engineering Science* 62, 22 (2007), 6297 – 6307.
- [126] Zhao, X., and Goveas, J.L. Size selection in viscoelastic emulsions under shear. 3788 – 3791.